# Bismuth Oxybromide-Based Photocatalysts for Solar Energy Utilisation and Environmental Remediation

Liang Kong

St Hilda's College, University of Oxford


A thesis submitted to the Department of Chemistry of the University of Oxford

for the degree of Doctor of Philosophy in Inorganic Chemistry.

Trinity Term 2013

The work described in my thesis was performed in Inorganic Chemistry Laboratory, University of Oxford from October 2009 to April 2013, under the supervision of Prof. Peter P. Edwards. All the work is my own and unless otherwise stated, and has not been submitted previously for any degree in this University or elsewhere.

Liang Kong, April 2013

# Acknowledgments

It would not have been possible to write this doctoral thesis without the guidance and help of the kind people around me who in one way or another contributed their valuable assistance in the preparation and completion of this study, for which I am extremely grateful.

This thesis would not have been possible without the help, support and patience of my supervisor, Prof. Peter P. Edwards, and for giving me the chance to work in such interesting field, and also thank you to Linda Webb for all the last-minute emails that I have been bothering you. I would like to express my deepest gratitude to my second supervisor, Dr. Zheng Jiang, for guiding my research for the past several years, not to mention his advice and knowledge. I have learnt so much from you, the sincerity and encouragement I will never forget.

I am most grateful to Dr. Kate Ryan and Dr. Liam France for helping me with proof reading. Dr. Martin Owen-Jones, Dr. Tiancun Xiao and Dr Vladimir L. Kuznetsov are thanked for their part in my doctorate.

I would also like to thank my colleagues and friends for being awesome and wonderful all the time: special thanks to Dr. Andrew Seel, who as a good friend, was always willing to help and give his best suggestions. Many thanks to Philippe, Josh, Henry, Katie and Nazanin, it would have been a lonely and boring lab without you guys (or Katie's brownie cakes which are amazing); thank you Yue Li and Xiangxue Kong for being such loyal and true friends to rely on. Finally, I would like to thank my parents for giving me their unequivocal support and great patience throughout, as always, for which my mere expression of thanks likewise does not suffice.

I gratefully acknowledge China Oxford Scholarship Fund for funding.

# Bismuth Oxybromide-Based Photocatalysts for Solar Energy Utilisation and Environmental Remediation

Liang Kong

Submitted for the degree of Doctor of Philosophy in Trinity 2013.

St Hilda's College, Oxford.

**Abstract**

This thesis reports the investigation of Bismuth oxybromide (BiOBr) semiconductor material as an efficient photocatalyst for the sunlight harvesting as well as environmental cleanup. I have utilised different synthetic methodologies to obtain BiOBr and its derivatives, such as co-precipitation, ultrasonification, and photo-deposition; and have studied their structural and optical properties by X-ray diffraction and surface analysis techniques. I report the synthesis and characterisation of two new p-n heterojunction systems, AgBr-BiOBr and BiOBr-$ZnFe_2O_4$, and have performed initial studies on photocatalytic reaction and their catalytic decomposition mechanisms. I have also reported the surface modification method including the deposition of noble metal on BiOBr to investigate the role played by the noble metal and the interactions between semiconductor and metal using various characterisation measurements. Furthermore, a continuous series of BiOBr-BiOI solid solutions were synthesised, characterised and the photocatalytic degradation was performed on the as-obtained semiconductors, to study the band structure properties of the solid solutions.

# Publications

1. Does Noble Metal Modification Improve the Photocatalytic Activity of BiOCl? L. Kong, Z. Jiang, H. Lai, T. Xiao, P. P. Edwards, *Progress in Natural Science*: *Materials International* (In press)

2. Unusual Reactivity of Visible-Light-Responsive AgBr-BiOBr Heterojunction Photocatalysts, L. Kong, Z. Jiang, T. Xiao, H. Lai, R. J. Nicholls, M. O. Jones, P. P. Edwards, *Journal of Catalysis*, 2012, 293, 116-125

3. BiOBr-$ZnFe_2O_4$ Heterojunctions with Exceptional Visible-Light-Driven Photocatalytic Activity for Water Purification, L. Kong, Z. Jiang, T. Xiao, M. O. Jones, P. P. Edwards, *Chemical Communications*, 2011, 47, 5512-5514

4. Visible-Light-Driven Photodegradation of Rhodamine B on Ag Modified BiOBr, L. Lu, L. Kong, Z. Jiang, H. Lai, T. Xiao, P. P. Edwards, *Catalysis Letters*, 2012, 142, 771-778

5. The Hydrothermal Synthesis of BiOBr Flakes for Visible-Light-Responsive Photocatalytic Degradation of Methyl Orange, Z. Jiang, F. Yang, G. Yang, L. Kong, M. O. Jones, T. Xiao, P. P. Edwards, *Journal of Photochemistry and Photobiology A*: *Chemistry*, 2010, 22:8-13

6. Catalytic Combustion of Propane over Mixed Oxides Derived from $Cu_xMg_{3-x}Al$ Hydrotalcites, Z. Jiang, L. Kong, L. J. France, T. Xiao, P. P. Edwards, *Fuel*, 2012, 96, 257-263

7. Ultrasound Induced Self-Assembly of BiOBr as a Robust Visible-Light-Responsive Photocatalyst, Z. Jiang, L. Kong, H. F. Greer, P. Aeberhard, H. Lai, J. Tang, W. Zhou, M. O. Jones, T. Xiao, P. P. Edwards, *Energy Environmental Science*, Accepted

# Contents

# Chapter 1

# Introduction

The urgent need for development and utilisation of technology for renewable energy should be promoted by increasing the public's awareness that Earth's oil reserves could run out during this century as the energy needs of the planet are likely to double within the next 50 years.[1, 2] The technologies for renewable energy include the $CO_2$ capture and storage, which offers the conversion of $CO_2$ to syn-gas, methanol and/or basic chemicals through either catalysis or photocatalysis process;[3, 4, 5, 1] hydrogen generation utilising sunlight through water splitting, which can then be used for fuel;[6, 7, 8, 9, 10, 11, 12] and solar photovoltaics (PV) use sunlight to generate electricity.[13]

Public concerns have been highlighted by the disastrous environmental pollution arising from the use of fossil fuels, such as $NO_x$, $SO_x$ and soot.[14, 15, 16] Efforts to eliminate environmental contamination can increase the emission of carbon dioxide ($CO_2$), either through catalyst generation or utilisation of technology. This presents a dilemma due to the need to clean up pollutants however energy concerns need to be considered. Hence energy balances and ultimately pollution balances become im-

portant. Under such conditions, we have come to the stage that requires exploration of new systems that can gently harmonise the contaminated environment to restore original conditions by using renewable energy.[1]

Utilising solar energy in various forms, such as solar photovoltaics, solar thermal electricity and solar fuels, can make considerable contributions to solving the major challenges, including climate change, energy security and universal access to modern energy services.[17, 18] Solar energy offers a clean, climate-friendly, abundant and inexhaustible energy resource to mankind, therefore, utilising and converting solar energy efficiently has become the priority for the sustainable future of human beings.[19, 20, 11]

## 1.1 Photodegradation of water pollutants

Environmental contamination, which is growing around the world and affecting the daily life of human beings, is a serious problem not to be neglected. Such contamination as water pollution is due both to microbial infection and to the presence of organic and inorganic waste materials, including harmful chemicals.[21, 22, 23] Great breakthroughs have been made with the introduction of chlorine as chlorinated lime in 1835. Chlorine, usually added in concentration between 1 ppm and 3 ppm, is now widely used to disinfect drinking water supplies and swimming pools, which has been a major factor in preventing the transmission of water-borne disease.[24] However, chlorine is ineffective against most organic and inorganic chemical pollutants, which include toxic heavy metals and anions; organic solvents such as hydrocarbons and chlorocarbons, agrochemicals such as pesticide, fertilisers and herbicides.[25]

*Advanced oxidation processes* (AOPs) for wastewater treatment refer to a set of

chemical treatment procedures designed to remove organic or inorganic materials by oxidation through reactions with hydroxyl radicals (·OH), with or without ultraviolet (UV) irradiation, ozonation, and $O_3$/UV treatment.[26] With a relatively high oxidation potential ($E^0 = +2.07\,\text{eV}$), ozone alone reacts very slowly with various compounds, though improved treatments methods have been utilised to generate the ·OH radicals by combining ozone with UV light, the radicals are even more reactive oxidants ($E^0 = +3.06\,\text{eV}$).[27, 28, 29] A major problem preventing the widespread application of ozone is the high cost of this treatment. In contrast to the above AOPs in homogeneous solutions in which the oxidants are consumed, heterogeneous photocatalytic oxidations use near-UV and visible-light as the energy source may overcome the required activation energy.[30] Conventionally, water or dissolved oxygen usually provides the necessary oxidants; the photocatalysts, such as $TiO_2$, ZnO, *etc* could be reused, or in a fixed-bed reactor for extended lifetime.[31] Also, sunlight is considered an inexpensive light source, which is the ultimate renewable energy, modern UV/visible-light sources, such as the Xenon and Mercury lamps, may enable economic application of photocatalysis.[32]

One of the most important fields in photocatalysis focuses on semiconductor photocatalyst for degradation of organic pollutants in water, with the use of inexpensive and clean solar light as the energy source. The major advantage of this method is that a lot of organic pollutants can be mineralised completely into $CO_2$, $H_2O$ and inorganic ions. Pollution controls either in aqueous solutions or air, is so far the most studied application of photocatalysis. It may also be applied to the production of fuels such as hydrogen or as a green route to obtain fine chemicals.[33, 34, 22] Photocatalysts are usually solid semiconductors which are (i) able to absorb visible and/or

UV light, (ii) chemically and biologically inert and photo-stable, (iii) inexpensive and (iv) nontoxic/low-toxic.[35, 2, 23] Therefore, photocatalysis has attracted great potential in the applications of environmental pollutant cleanup and solar energy conversion.

## 1.2 Basic theory of photocatalysis

The term 'photocatalysis' is mostly described as the 'acceleration of a photoreaction by the presence of a photocatalyst', it involves photoreactions which occur at the surface of a catalyst. Semiconductor photocatalysis offers great potential in the application of renewable energy conversion and utilisation. This area has been intensively investigated since Fujishima and Honda firstly reported that a $TiO_2$ electrode could generate hydrogen and oxygen via water splitting under light irradiation in 1972.[36] The various applications of photocatalyst materials include *water purification*-the decomposition and disposal of refractory organic compounds in the sewage and waste water; *antibacterial*-the sterilisation, purification and prevention of the viruses and bacteria such as Escherichia coli; *air purification*-the disposal of the noxious compounds such as nitrogen oxide (NOx), sulphur oxide (SOx) and formaldehyde ($CH_2O$) in the air; *deodorisation*-the decomposition of odor compounds such as acetaldehyde ($CH_3CHO$), ammonia ($NH_3$) and hydrogen sulphide ($H_2S$); *decontamination*-the decomposition and disposal of organic compounds that stick to the surface of catalysts such as cigarette smoke and oil dredges.[37, 38] The advantages such as energy-saving, high efficiency, and no second-hand pollution generated provide it great potential in environmental cleanup. More importantly, photocatalyst materials could reduce $CO_2$ into ethanol, ethane, *etc.* through photo-generated charge carriers under

light excitation, which is significantly promising in the photo-reduction of $CO_2$, the most thermodynamically stable greenhouse gas (GHG).[39, 23, 16]

The basic process of heterogeneous photocatalysis over organic/inorganic semiconductor photocatalysts is illustrated in Figure 1.1. The absorption of photons by photocatalysts is regarded as the first step of photocatalysis. When the energy of incident light is larger than that of a band gap, electrons and holes are generated in the conduction band and valence band, respectively. The photo-generated electrons and holes cause redox reactions. The second step consists of the charge carrier separation and migration. A range of factors, such as crystal structure, crystallinity and particle size strongly affect this step.[34] Low crystallinity of the semiconductor photocatalysts leads to high concentrations of defects, and the defects act as trapping and recombination centres for the electron-hole charge carriers. Therefore the defects will decrease the reactivity of semiconductor photocatalysts. A small particle size means that the distance for photo-generated electrons and holes to migrate to reaction sites on the surface of semiconductor becomes short, and this might result in a decrease in the recombination probability. The final step in Figure 1.1 involves the surface chemical reactions. The important factors that affect the reactivity are the nature of the active sites and the surface area of the semiconductor photocatalyst.

Figure 1.2 gives band gaps and band edge position for a number of semiconductor materials. The data refers to conditions where the semiconductor is in contact with aqueous electrolyte of pH 1, the band levels usually shift with a change in pH ($-\frac{0.059\,eV}{pH}$).[40, 17, 41] The standard potentials for several redox couples are shown in figure 1.2, which indicates the thermodynamic limitations for the photocatalytic

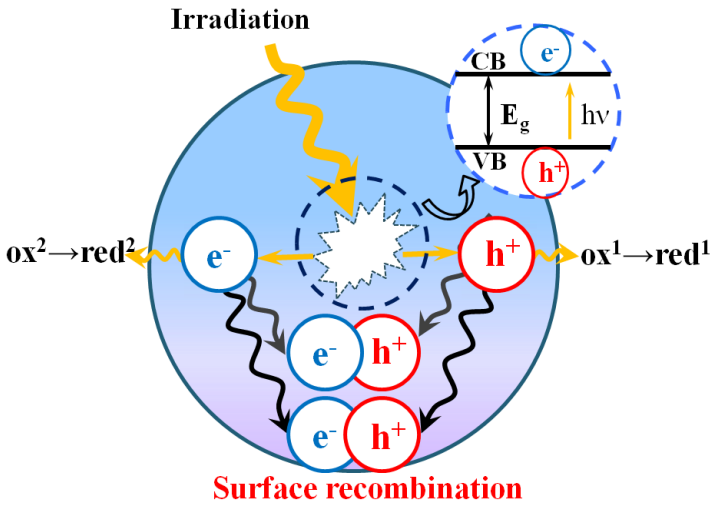


Figure 1.1: Illustration of photo-generated electron and hole transfer pathway

reactions that could be carried out with the charge carriers. For example, if a reduction reaction of the species in the electrolyte is to be performed, the conduction band position of the semiconductor material has to be located above the relevant redox level; and for an oxidation reaction, the valence band position of the semiconductor has to be positioned below the relevant redox level.[41, 42, 28, 18] The free energy of the charge carriers (electron-hole pairs) generated by photo-excitation of semiconductors is directly related to their chemical potential. In the dark, upon thermal equilibrium, the chemical potential of the electron is equal to that of the hole and corresponds to the Fermi level of the solid.

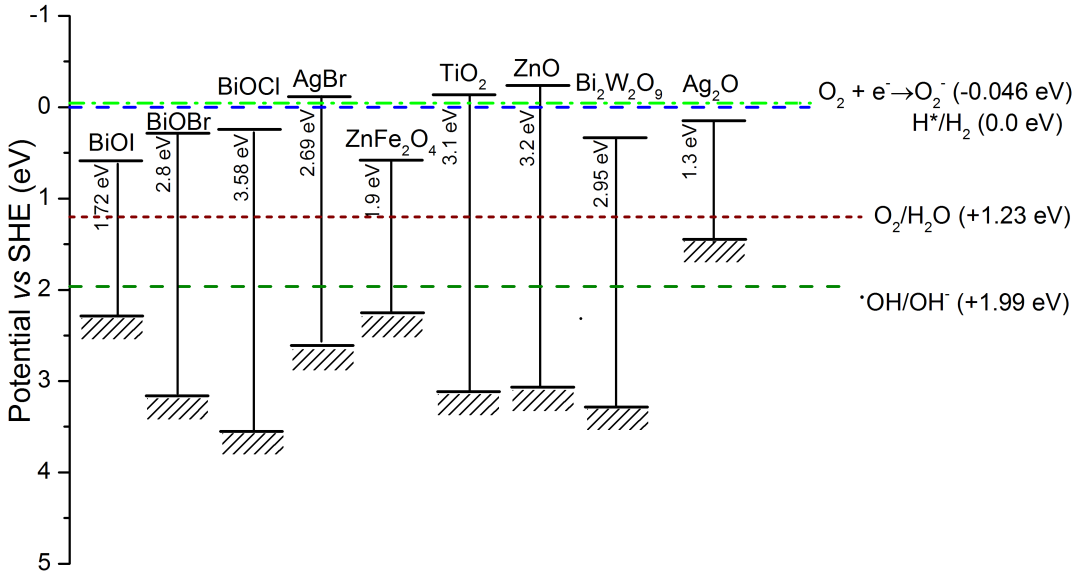


Figure 1.2: Valence and conduction band position for a range of semiconductors on a potential scale (eV) *versus* the standard hydrogen electrode (SHE).

## 1.3 Basic theory of semiconductors

### 1.3.1 General background

A semiconductor is a crystalline or amorphous solid whose electrical conductivity is typically intermediate between that of a metal and an insulator and can be changed significantly by altering the temperature or the impurity content of the material, or by illumination with light.[43] The energy levels of semiconductors take the form of groups of closely spaced levels that form bands. In the absence of thermal excitations (at $T = 0\,K$), these are either completely occupied by electrons or completely empty. The highest filled band is the valence band and the empty band above the valence band is the conduction band.[44, 37] Semiconductors have a band structure in which the conduction band is separated from the valence band by a band gap with a

suitable width. Thermal and optical interactions will impart energy to an electron, causing it to jump across the gap from the valence band into the conduction band, leaving a hole behind. The inverse process can also occur when an electron decays from the conduction band into the valence band to fill an empty state by means of a process known as electron-hole recombination.[33, 34] The lifetime of photo-generated electron-hole charge carriers is typically of the order of one nanosecond, which enables the transfer of the electrons onto the species absorbed on the surface of the semiconductors. A semiconductor may exhibit conductivity which is either n-type (mobile electrons in the conduction band) or p-type (mobile holes in the valence band) as shown in Figure 1.3. The mobile charge carriers in the semiconductor could interact with different redox couples in solution.[45]

### 1.3.2 Energy band and charge carrier

In general, the energies of electrons in a solid are referenced to the vacuum level. Photoemission measurements can be performed to determine the electron affinity of the semiconductor.[46, 45] In the study of photocatalysis, it is often desirable to relate the vacuum-level energies to the electrochemical scale of redox potentials. The redox potential of a solution, $E(\mathrm{A}^+/\mathrm{A})$, is related to the standard reduction potential $E^{\Theta}(\mathrm{A}^+/\mathrm{A})$ by the Nernst equation:

$$E(\mathrm{A}^+/\mathrm{A}) = E^{\Theta}(\mathrm{A}^+/\mathrm{A}) + (\frac{kT}{q}) \ln(\frac{C_{red}}{C_{ox}})$$

In this equation, $C_{red}$ and $C_{ox}$ are the concentrations of A and $\mathrm{A}^+$ in units of mol/mL, and $E^{\Theta}$ is the standard reduction potential for the $\mathrm{A}^+/\mathrm{A}$ couple in the particular

solvent and electrolyte of interest. At present, the best estimates for the absolute value of the redox energy scale indicate that a standard hydrogen electrode (SHE) is at 4.5 eV *versus* vacuum level.[47, 48, 49]

By consideration of the Mulliken electronegativity of the atoms involved, the valence band (VB) edge potential of a semiconductor at the point of zero charge can be expressed:

$$E_{\mathrm{VB}} = \chi_{\mathrm{Semiconductor}} - E^e + \frac{1}{2}E_g$$

where $E_{\mathrm{VB}}$ is the VB edge potential, $\chi_{\mathrm{Semiconductor}}$ is the electronegativity of the semiconductor, which is the geometric mean of the electronegativity of the constituent atoms, $E^e$ is the energy of free electrons on the hydrogen scale (ca. 4.5 eV), and $E_g$ is the band gap energy of the semiconductor.[50, 51, 52] According to the equation: $E_{CB} = E_{VB} - E_g$, the conduction band edge could also be estimated by knowing the band gap energy of a semiconductor material.

Fermi level is determined as the energy point where the probability of occupancy by an electron is exactly 50%. It is used to describe the top of the collection of electron energy levels at absolute zero temperature, it could be calculated from the density of states in the conduction and valence band. The Fermi level may change with increasing temperature, depending on the number of states in the conduction and valence band. When two semiconductor materials with different Fermi levels are in contact, charge carriers will flow between the two regions until the Fermi level is aligned across the interface.

The process whereby electrons are excited into the conduction band and consequently leave a hole, is known as electron-hole pair generation.[53] The electrons in

the valence band need to have enough extra energy to go across the bandgap to get into the energy levels of the conduction band. If, for instance, an external electric field is applied to the material, the electrons in the conduction band are free to move because there are many states available around them at their energy level. They also tend to recombine, which is the opposite process to the creation of an electron-hole pair. The conservation of energy demands that these recombination process in which an electron loses a certain amount of energy will be accompanied by the emission of thermal energy or radiation.[54]

Electrons excited to the conduction band also leave behind electron holes, i.e., unoccupied states in the valence band. Both the conduction band electrons and the valence band holes contribute to electrical conductivity. Basically the electrons transfer between conduction band and valence band while the holes actually do not move, but a neighboring electron could move to fill the hole, leaving a hole at the place it has just come from, and in this way the holes appear to move.[55]

### 1.3.3 Intrinsic and extrinsic semiconductors

In most pure semiconductors at room temperature, the population of thermally excited charge carriers is very limited. Therefore it could be speculated that when the semiconductors are extremely pure, these materials have very low electrical conductivities, which could be overcome by doping a semiconductor material with impurity atoms. An intrinsic semiconductor is ideally a perfect crystal.[56] Even very tiny controlled addition of impurity atoms can make a very large difference to the conductivity of a semiconductor. In a pure semiconductor the valence band is completely filled at absolute zero.[48] At finite temperature the only charge carriers are the elec-

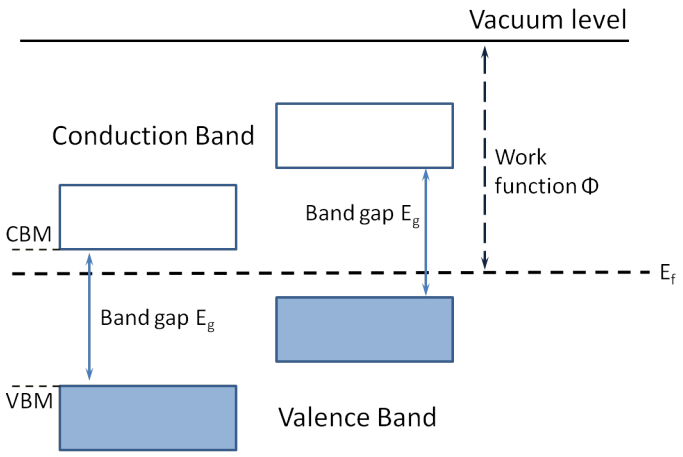


Figure 1.3: Illustration of p-type and n-type semiconductors. Shaded areas represent energy levels filled at absolute zero, below the Fermi level.

trons in the conduction band and the holes in the valence band that arises from the thermal excitation of electrons from valence band to conduction band. These are known as intrinsic charge carriers, and the numbers of electrons and holes are equal since electrons and holes are always created in pairs, $n = p = n_i$, where $n$ is the number of electrons in the conduction band per unit volume (electron concentration), $p$ is the number of holes in the valence band per unit volume (hole concentration) and $n_i$ is the symbol for 'intrinsic carrier concentration'.[20]

Extrinsic semiconductors are made by introducing different atoms, which are called dopant atoms, into the crystal. There are two types of extrinsic material, p-type and n-type. In an extrinsic semiconductor there is a contribution to the total number of charge carriers from intrinsic electrons and holes, but at room temperature this contribution is usually very small in comparison with the number of charge carriers introduced by the controlled impurity doping of the semiconductor.

In n-type semiconductors, the dopant atoms added to the semiconductor crystal are donor atoms. For instance, phosphorus (P), arsenic (As) or antimony (Sb) can be used as donors in crystalline semiconductors such as Si or Ge. If a small number of atoms of a group V element such as nitrogen (N) are added to the pure semiconductor as substitutional atoms in the lattice, additional electrons are introduced into the material due to the extra valence electrons that the impurity has.[57] These additional electrons are bound only weakly to their parent dopant, and even at very low temperature these electrons can be promoted into the conduction band of the semiconductor, leaving a positively charged atom behind. This process is sometimes called 'activation' of the donor atom. The positively charged donor atom that is left behind is immobile and does not contribute to conduction. On the other hand, the electron leaving the atom does and is counted in the electron concentration $n$. Because the activation energy is very low, at room temperature almost all of the donor atoms included in the crystal will give an electron to the conduction band. So if $N_D$ is the donor concentration, for an n-type semiconductor at equilibrium: $n_0 \approx N_D$.

In n-type semiconductors, electrons are the majority carriers; conversely, if a group III element such as boron (B), aluminum (Al) and gallium (Ga) is used for doping p-type semiconductors. The dopant atoms in p-type semiconductors are acceptor atoms. These acceptor atoms introduce electron-accepting levels just above the top of the valence band. When these atoms are included in the crystal, one of the electrons in the semiconductor valence band can easily jump to the valence band shell of one of the acceptor atoms, leaving a hole and making the acceptor atom negatively charged. The negatively charged acceptor atom after an electron joins its valence shell is immobile and does not contribute to conduction. The hole left

behind by the electron does and is counted in the hole concentration $p$. Because the activation energy is low, at room temperature almost all of the acceptor atoms included in the crystal will accept an electron from the valence band. So if $N_A$ is the acceptor concentration, for a p-type semiconductor at equilibrium: $p_0 \approx N_A$.[58]

In an intrinsic semiconductor, $n = p$, which implies that there is an equal chance of finding an electron at the conduction band edge as there is of finding a hole at the valence band edge. It can be deduced that the Fermi level $E_F$ must be in the middle of the band gap for an intrinsic semiconductor.

For an n-type semiconductor, there are more electrons in the conduction band than there are holes in the valence band, which also implies that the probability of finding an electron near the conduction band edge is larger than the probability of finding a hole at the valence band edge. Therefore, the Fermi level is closer to the conduction band in an n-type semiconductor. For a p-type semiconductor, there are more holes in the valence band than there are electrons in the conduction band, which implies that the probability of finding an electron near the conduction band edge is smaller than the probability of finding a hole at the valence band edge. Therefore, the Fermi level is closer to the valence band in a p-type semiconductor.

### 1.3.4 Thermal and optical excitations in semiconductors

In an undoped semiconductor at 0 K, the valence band is completely occupied, the conduction band is completely unoccupied, and no current can flow. Increases in conductivity could be obtained by exposure of the semiconductor to either light or heat irradiation, because the energy could promote electrons from the valence band to the conduction band. When carriers in a semiconductor are excited thermally,

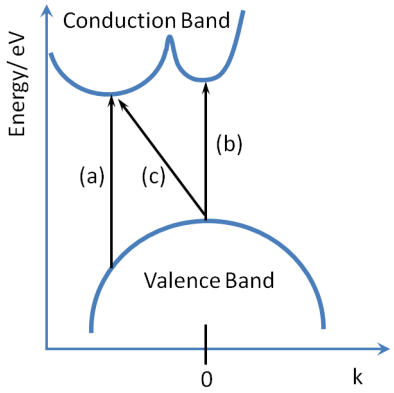


Figure 1.4: Electronic absorption processes between semiconductor bands. Process (a) requires the lowest-energy photon, but involves a momentum change and is an indirect transition. (a) and (b) are higher-energy, direct transitions.

electrons are transferred to the conduction band, and an equal number of holes are generated in the valence band.[25]

As has been mentioned previously, a photon can provide the energy to produce an electron-hole pair. Each photon of energy $E$ has momentum $p = \frac{E}{c}$, where $c$ is the velocity of light ($3 \times 10^8\, m/s$). An optical photon has an energy of the order of $10^{-19}$ J, therefore a typical photon has a very small amount of momentum $5.34 \times 10^{-28}\, kg \cdot m/s$.[59] Upon light irradiation, semiconductors absorb light below a threshold wavelength $\lambda_g$, the fundamental absorption edge, which is related to the band gap energy $E_g$ via

$$\lambda_g(nm) = \frac{1239.8}{E_g(eV)}$$

Near threshold, the value of $\alpha$, which is the reciprocal absorption length increases

with increasing photon energy. Generally, a function of the type of semiconductor

$$\alpha \times h\nu = A(h\nu - E_g)^n$$

gives a description of the absorption behavior in this wavelength domain. Here the exponent has the value $\frac{1}{2}$ for a direct transition and 2 for an indirect transition. A direct transition may be characterised by the minimum of wave vector in the conduction band states which is placed vertically above the maximum in the valence band energy states as indicated in Figure 1.4. The absorption of a photon can produce an electron-hole pair quite easily, however, for an indirect transition the two extremes are located at different wave-vectors, so the electron must interact not only with the photon to gain energy, but also with a so-called lattice vibration phonon in order to either gain or lose momentum.[53] This process reduces the absorption cross section and hence the value of $\alpha$. Hence, the indirect process takes place at a much lower rate, as it requires three entities to intersect in order to proceed: an electron, a photon and a phonon. Similarly, the principle applies to the recombination of electrons and holes to produce photons. The recombination process is much more efficient for a direct semiconductor than that for an indirect semiconductor, where the process must be mediated by a phonon.

## 1.4 Strategies to improve the photocatalytic performance of semiconductor materials

### 1.4.1 Nonmetal doping

The property of semiconductor materials can easily be modified by introducing impurities into their crystal lattice, and the process of adding controlled impurities to a semiconductor is known as doping. The amount of impurity, or dopant, added to an intrinsic semiconductor varies its level of conduction and/or valence band. The most widely investigated conventional semiconductors are $TiO_2$ and ZnO, and visible-light response has been stimulated by anion elements doping, such as nitrogen, carbon, and sulphur etc..[60, 61, 62] Some N-doped $TiO_2$ samples are more active than commercial $TiO_2$ Degussa P25, a widely used photocatalyst composing of anatase and rutile crystallites, for the photodegradation process under visible-light illumination. The nitrogen substituted at some of the oxygen sites in $TiO_2$, which formed a narrow N $2p$ band above the valence band, which was responsible for the visible-light sensitivity.[63, 16]

### 1.4.2 Metal doping

The work function of a material is the energy required to remove an electron from the level of the chemical potential and give it enough energy to escape to vacuum level, which are labeled $\Phi_M$ and $\Phi_S$ respectively in Figure 1.5. When a metal and a semiconductor are in contact, two possible types of contact can result, depending on the combination of metal and semiconductor used. The contact may be rectifying, which only allows current to flow in one direction. Ohmic contact allows current

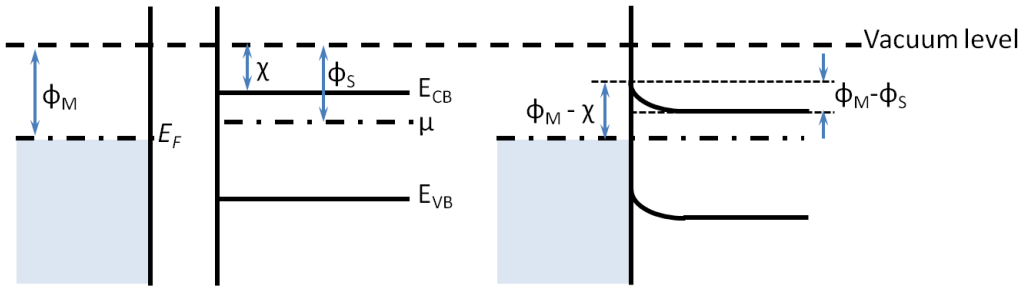


Figure 1.5: Illustration of metal-semiconductor junction before (left) and after contact (right); the dashed line at the top represents the vacuum level, which is the zero of energy at infinity. The chemical potential of the semiconductor is represented by the dash dot line labeled $\mu$; while for the metal, the chemical potential is located at the Fermi level, labeled $E_F$. The energy difference labeled as $\chi$ between the bottom of the conduction band and vacuum level is the electron affinity of the semiconductor.

to pass in either direction. A rectifying contact is also know as a Schottky barrier contact.

Figure 1.5 shows a metal and n-type semiconductor contact. Electrons could lower their energy by flowing from the conduction band of the semiconductor into the metal. Consequently the charge aggregation built on the metal-semiconductor interface will cause a bending of the bands, which continues until the chemical potential of the semiconductor reaches equilibrium with the Fermi energy of the metal. The deformed band structure will form a potential barrier which the electrons must overcome in order to flow from the semiconductor into the metal.

Doping (metals/nonmetals) generates impurity levels in the band gap of semiconductors; if these states lie close to the band edges they give rise to shallow donor or acceptor states. However, if they are located deep in the band gap they may act as recombination centres for photogenerated charge carrier.[62] High photocatalytic

activity can be achieved if the charge carriers can be transferred efficiently from the impurity levels to the surface. Photocatalytic activity is determined by the competition between this charge carrier promotion rate to the surface and the recombination rate. Photogenerated charge carriers cannot get enough time to engage in redox reactions at the surface of semiconductors if the recombination rate is too high. It has been confirmed that impurity doping can sometimes improve the photocatalytic activity. However, the density of impurity states increase with an increase in the doping level, which can also accelerate recombination process.

### 1.4.3 p-n junctions (semiconductor coupling)

A junction between an n-type semiconductor and a p-type semiconductor could be generated when the two types of semiconductor come into contact, and electrons flow from the n-type semiconductor into the p-type semiconductor. Simultaneously holes flow from the p-type into the n-type material. The chemical potentials move towards equilibrium and the bands will be deformed as a consequence. Charge transfer from one semiconductor to another with suitable band edge position that is thermodynamically favourable can increase the lifetime of the charge carriers and thus promote interfacial charge transfer and photocatalytic efficiency. In addition to the proper location of the band edges of two coupled semiconductors, the extent of visible-light absorption is also crucial for deciding the observed visible-light efficiency of coupled semiconductors.[62]

By coupling a wide band gap semiconductor such as ZnO and $TiO_2$ with a narrow band gap semiconductor, the photo-response is extended to the visible-light region and charge carrier separation can therefore be achieved.[64, 65, 66] The proportion of

the narrow band gap semiconductors may determine the visible-light activity of the coupled system. In some cases, improved visible-light absorption and degradation activity can be observed under visible-light irradiation with an enhancement in the concentration of narrow band gap semiconductors. However, with higher concentration of the sensitiser the surface of host semiconductor can be covered entirely and inhibiting surface redox reactions, which leads to the deactivation of the coupled semiconductors system.[65]

## 1.5 Bismuth oxyhalides semiconductor photocatalysts

The semiconductors $TiO_2$, ZnO, CdS, CdSe, $SrTiO_3$, $CeO_2$, $WO_3$, $Fe_2O_3$ and $Bi_2S_3$ can all act as photoactive materials for charge-transfer processes due to their electronic structures which are characterised by a filled valence band and an empty conduction band.[37] However, these traditional visible-light-responsive photocatalysts are either unstable under solar light irradiation (i.e., CdS and CdSe) or have low activity such as $Fe_2O_3$. So far, bismuth-based binary/ternary compounds have been investigated in the application of photocatalysis.

$Bi_2O_3$ is an important metal oxide semiconductor with four crystallographic polymorphs, which gives band gap energy ranging from 2.0 eV to 3.96 eV.[67] Photogenerated electrons on the conduction band and holes on the valence band will be separated on the surface of $Bi_2O_3$ upon light excitation with energy more than the band gap energy of $Bi_2O_3$. Those electrons and holes will react with $H_2O$ and $O_2$, and then generate free radicals with very strong reducing and oxidising ability. Therefore the redox reactions would take place between the radicals and the organics absorbed

on the surface of the particles, and the organics will be photo-decomposed ultimately.

It has been reported that $Bi_2O_3$ nano-particles synthesised by an ammonia co-precipitation method displayed better photocatalytic performance comparing to the commercial $Bi_2O_3$ nano-particles. Zhang et al. reported a surfactant-assisted sono-chemical route to synthesise $Bi_2O_3$ nano-particles with grain size of 40 nm to 100 nm and band gap energy of 2.85 eV. The visible-light responsive $Bi_2O_3$ nano-crystals exhibit superior activity to that of microsized $Bi_2O_3$ and commercial $TiO_2$ P-25.[67] There are several strategies for decorating the $Bi_2O_3$ semiconductor to improve the photocatalytic activity, such as doping with transition metals (i.e., Co(II), Ni(II), Fe(III), Pd(II), Cr(VI), and Ru(III)), and combining $Bi_2O_3$ with other semiconductors (such as $TiO_2$ and $Bi_2WO_6$), both of which display better reactivity than pure $Bi_2O_3$ and commercial $TiO_2$ P-25. However, the binary bismuth-based semiconductors are not very effective for photocatalytic degradation under visible-light irradiation. More attention has been paid to the investigation of bismuth-based ternary semiconductor compounds with enhanced visible light response and better photocatalytic activity, for example, bismuth oxyhalides.

Bismuth oxyhalides, BiOX (X=F, Cl, Br, and I) crystallise in the tetragonal space group $P4/nmm$ (PbFCl structure type).[68, 69] The crystal structure of BiOX could be thought of as consisting of tetragonal $[Bi_2O_2]$ layers which are 'sandwiched' by two halogen layers (Figure 1.6 A to C). The $Bi_2O_2X_2$ layers interact mainly via Van-der-Waals forces.[70] Therefore, this structure is not closely packed along the $c-$axis. From BiOCl to BiOI, the lattice parameter $a$ increases by only 0.1 Å (from 3.89 Å to 3.98 Å) while $c$ increases by 1.8 Å (from 7.35 Å to 9.13 Å).[71] The bismuth atoms adopt a distorted square antiprismatic coordination geometry, with four halide

atoms forming one of the square faces, each at a characteristic distance from Bi, and four oxygen atoms forming the other square face, each at a distance of 2.32 Å from Bi.[72] The oxygen atoms are tetrahedrally coordinated by four bismuth atoms. The layered structure of BiOX could provide a space large enough to polarise the related atoms and orbitals, and the induced dipole can separate the electron-hole pair efficiently.[73, 74] The bismuth oxyhalides materials exhibit significantly improved visible light absorption ability and photocatalytic performance compared to that of commercial $TiO_2$. BiOBr has an indirect band gap so that the excited electron has to undergo a significant change in its momentum for a photon of energy $E_g$ to produce an electron-hole pair (as shown in Figure 1.6 D). The recombination process is much less efficient for an in-direct band gap semiconductor than for a direct band gap semiconductor, where the process must be mediated by a phonon.[75] This process reduces the recombination probability of the photo-excited electrons and holes. Both the loose packed structure and indirect-transitions may facilitate the electron-hole separation and the charge transport, hence the photocatalytic reactions.[76]

Among the bismuth oxyhalides, bismuth oxybromide (BiOBr) is the most efficient photocatalyst for decomposition of organic pollutants. It was experimentally demonstrated that its reactivity is higher compared to commercial nano-$TiO_2$ (Degussa P25) under both UV and visible-light irradiation.[78, 79, 80]

The valence band consists of Br $4p$, O $2p$ and Bi $6s$ hybridised orbitals as shown in Figure 1.6 E. The valence band (VB) edge potential of a semiconductor at the point of zero charge can be expressed empirically via Mulliken electron negativity theory:

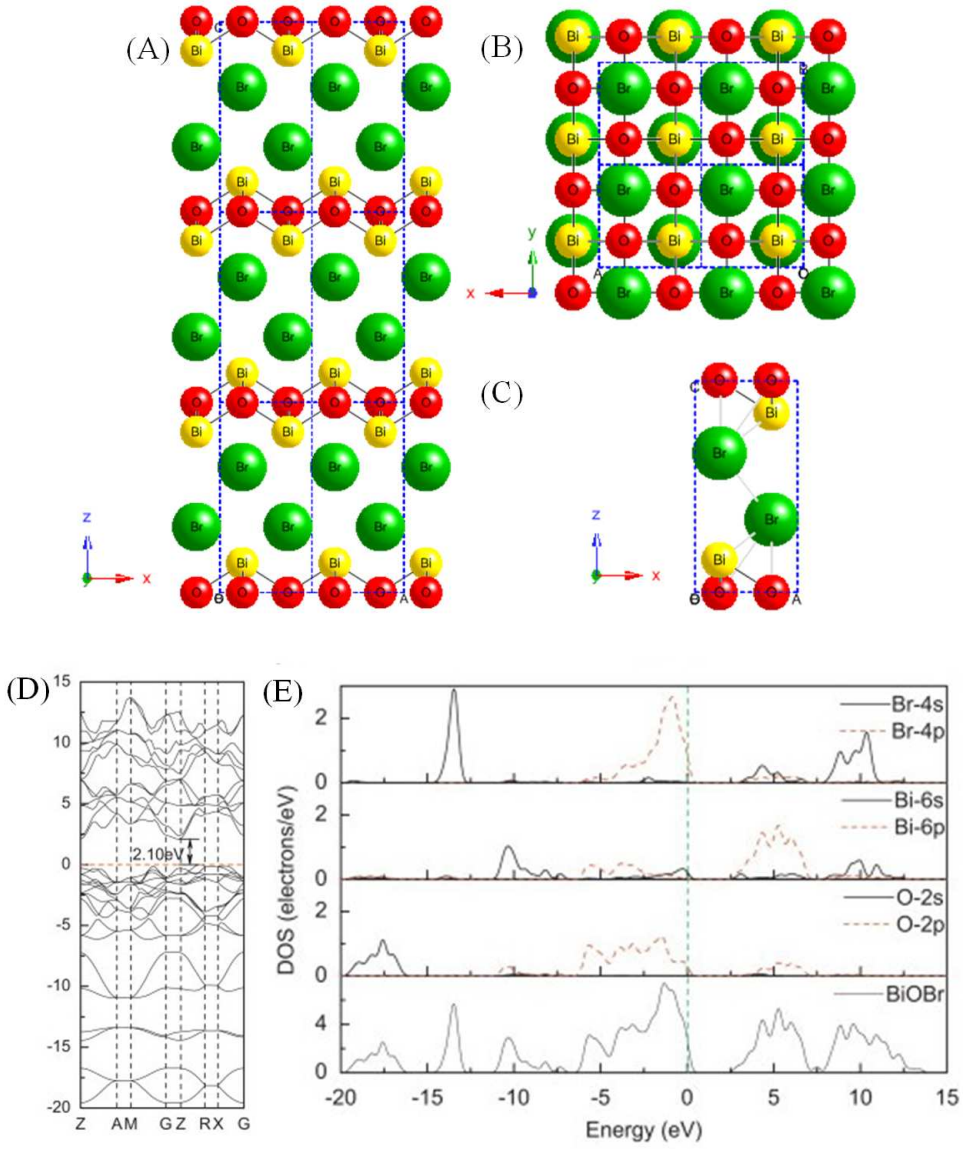


Figure 1.6: (A) Representation of a BiOBr structure (green, Br atoms; yellow, Bi atoms; red, O atoms), (B) the top view, (C) the unit cell of tetragonal BiOBr crystal, (D) the band structure and (E) density of states (DOS) and partial density of states (PDOS) for BiOBr crystal.[77]

$$E_{\mathrm{VB}} = \chi - E^e + \frac{1}{2}E_g$$

where $E_{\mathrm{VB}}$ is the VB edge potential, $\chi$ is the electronegativity of the semiconductor, which is the geometric mean of the electronegativity of the constituent atoms, and the electronegativity of each atom is defined as the arithmetic mean of the atomic electron affinity ($A$) and the first ionisation energy ($I$). For instance, the electronegativity $\chi$ of BiOBr and $Ag_2O$ is expressed in the form:

$$\chi_{\mathrm{BiOBr}} = \sqrt[3]{(\chi_{\mathrm{Bi}} \cdot \chi_{\mathrm{O}} \cdot \chi_{\mathrm{Br}})}$$

$$\chi_{\mathrm{TiO_2}} = \sqrt[3]{(\chi_{\mathrm{Ti}} \cdot \chi_{\mathrm{O}}^2)}$$

where the electronegativity of Br atom can be expressed as $\chi_{\mathrm{Bi}} = \frac{1}{2}(I_{\mathrm{Bi}} + A_{\mathrm{Bi}})$, $E^e$ is the energy of free electrons on the hydrogen scale ($\sim$4.5 eV), and $E_g$ is the band gap of the semiconductor. According to the equation: $E_{CB} = E_{VB} - E_g$, the conduction band edge could also be estimated by knowing the band gap energy of a semiconductor material.[50, 51, 52] It has been speculated that the valence band (VB) top potential of BiOBr lies in more positive position than that of $TiO_2$, implying that the photo-excited hole might have stronger oxidation ability towards organic molecules. BiOBr also has advantages such as low cost and low-toxicity, therefore it could be selected as a promising photocatalyst. [81]

## 1.6 Applications of photocatalysis

### 1.6.1 Photodegradation of organic pollutants

One of the most important applications of photocatalysis is the use of metal oxide semiconductors for photodegradation of organic pollutants in water under ambient conditions, with the utilisation of inexpensive and clean solar energy and atmospheric oxygen as the energy source and oxidant, respectively.[82] The major advantage of this method is that organic pollutants can be mineralised completely into $CO_2$, $H_2O$ and inorganic ions.[24]

The photodegradation pathway of the dye pollutants under visible-light irradiation differs from that under UV light irradiation. The major difference is that the photosensitisation process involves initial excitation of the dye molecules, rather than the semiconductor photocatalysts particles. In order to investigate the photodegradation mechanism and distinguish it from the photosensitisation process, two basic methods can be used to avoid photosensitisation of organic dyes, namely using UV light cut-off filter and colourless organic dyes. In the photosensitisation process, the electron is injected from the excited dye into the semiconductor conduction band. While the dye is converted into its radical cation, the injected electron in the conduction band can reduce surface-absorbed oxidants, usually the molecular oxygen, to yield the oxidising species such as $H_2O_2$, $O_2^{\bullet-}/HO_2^{\bullet}$, and $^{\bullet}OH$ radicals, which presumably cause the dye degradation.[22] As a matter of fact, the process of the dye photo-oxidation under visible-light irradiation in an aqueous suspension of semiconductor photocatalysts is rather complicated. The subsequent details of the degradation pathway remains uncertain, especially the role of oxygen and the radical

during the photodegradation process.

### 1.6.2 Photoelectrochemical water splitting

Photochemical splitting of water into $H_2$ and $O_2$ utilising solar energy is a process of great economic and environmental importance; the production of hydrogen fuel has gained increased attention as fossil fuels and other non-renewable resources become depleted. Photocatalytic water splitting has the simplicity of using powders in aqueous media under sunlight to produce $H_2$ and $O_2$ from water, which could provide a clean and renewable energy without generating greenhouse gas or causing side effects to the atmosphere.[10]

When $H_2O$ splits into $H_2$ and $O_2$ with the stoichiometric ratio 2:1 of its products: $2H_2O \xrightarrow{Heat} 2H_2 + O_2$, the process is highly endothermic ($\Delta H > 0$).[34] Water splitting occurs naturally in photosynthesis whereby a photon is absorbed and converted into chemical energy through a complex biological pathway. On the other hand, hydrogen production efficiency is considerably low comparing to the large amount of energy input, which makes it incompatible under current circumstances with existing energy generation. There are several requirements for a photocatalyst to be used in the water splitting process; the minimum potential difference needed to split water is 1.23 eV at pH=0, which means the minimum band gap energy for successful water splitting at pH=0 is 1.23 eV.[34] This corresponds to wavelength of 1008 nm. In order to make efficient use of the energy across the full spectrum of sunlight, the potential must be less than 3.0 eV. Materials used for photocatalytic water splitting must fulfill the band requirements and typically have dopants and/or co-catalysts added to optimise their performance. For example, conventional $TiO_2$ is usually utilised with a co-catalyst such as Pt and Pd to increase the rate of $H_2$ production.[83, 84] Most

semiconductor materials with suitable band structures can absorb UV light to split water; in order to absorb visible-light, it is necessary to narrow the band gap.

Though water splitting can transfer photo-generated charge carriers, corrosion of the photocatalysts used is inevitable under long-term irradiation, and the stability of the catalysts needs to be improved.[85, 23, 33] Defects within crystalline photocatalysts can act as recombination sites, which ultimately lower efficiency of $H_2$ production. The utilisation and conversion of solar energy into hydrogen by means of photocatalysis is one of the most promising techniques to achieve a clean and renewable energy system. The prime measure of photocatalyst efficiency in water splitting is the quantum yield (QY), which is:

$$\mathrm{QY}(\%) = \frac{\text{Photochemical reaction rate}}{\text{Photon absorption rate}} \times 100\%$$

However, this quantity can be misleading due to different experimental conditions. To assist the comparison, the rate of gas evolution can also be used despite the fact that the normalisation of the gas amount is significantly difficult. The best photocatalyst needs to have a high quantum yield as well as a high rate of hydrogen production.[34]

### 1.6.3 Photo-reduction of $CO_2$

Photo-reduction of $CO_2$ is an electrochemical reduction process which involves reducing $CO_2$ to higher order hydrocarbon species with light illumination.[3] Such application is of great significance because part of the energy that required for the $CO_2$ reduction comes from solar energy, which is a renewable source.

The catalytic conversion of $CO_2$ into liquid fuels has been a critical issue for

a long time as it could positively impact the global carbon balance by recycling $CO_2$ into fuels. However, the most difficult part of this process is that $CO_2$ is a highly stable molecule at room temperature.[1] Returning $CO_2$ to a useful state by activation and/or reduction is scientifically challenging, which requires appropriate catalysts and energy input. The ultimate goal is to produce hydrocarbons, such as methanol or methane via the photo-reduction of $CO_2$ mimicking the artificial photosynthesis process. That is to say, solar energy can be transformed and stored as chemical energy. More importantly, methanol is the most promising product of $CO_2$ photo-reduction because it can be transformed into other useful chemicals.

From a thermodynamic perspective, the transformation of 1 mol $CO_2$ into methanol is endothermic, and requires 228 kJ per mole and at the same time six electrons are required to reduce $CO_2$ from $C^{4+}$ to the $C^{2-}$ of methanol. The overall reaction is

$$CO_2 + 2H_2O \xrightarrow{h\nu} CH_3OH + O_2$$

The efficiency of $CO_2$ photo-reduction is one of the most challenging issues of environmental catalysis.[3] Various p-type semiconductors have been successfully employed for $CO_2$ photo-reduction including GaP, CdTe, $TiO_2$ and ZnS *etc.*.[86, 5, 87] From a kinetic perspective, these reactions are extremely slow on a given semiconductor surfaces though these systems have a couple of advantages such as sustainability, direct conversion of solar energy into chemical energy, and stability of the process.

## 1.7 Aim of this thesis

This thesis aims to explore useful systems under sunlight-type excitation; photocatalytic reactions under both UV and visible-light excitations are considered.

It will concentrate on bismuth oxyhalide-based photocatalysts, particularly BiOBr semiconductor materials that demonstrate extraordinary activity under light illumination for applications concerned with the elimination of pollutants and partial oxidation. Here the emphasis will be on developing effective photoactive materials with excellent stability obtained by various synthetic methodologies. The degradation pathway of the pollutants by visible-light photocatalysis will also be investigated and novel visible-light-responsive photocatalytic system with better photocatalytic performance will be described as well.

# Chapter 2

# Experimental Apparatus and Parameter Settings

Throughout this thesis, techniques such as X-ray diffraction, X-ray photoelectron spectroscopy and scanning/transmission electron microscopy, are used extensively to characterise the structural and electronic properties of the powder samples. This chapter presents a brief introduction to the background of these techniques utilised to generate the data presented in subsequent chapters.

## 2.1 Powder X-ray Diffraction (PXRD)

### 2.1.1 Explanation

X-ray diffraction yields the atomic structure of materials. It is based on the elastic scattering of X-rays from the electron clouds of the individual atoms in the system. Powder X-ray Diffraction (PXRD) is a technique used to characterise the crystal-

lographic structure, crystallite size (grain size), and preferred orientation in polycrystalline or powdered solid samples. Powder diffraction is commonly used which identifies unknown substances, by comparing the XRD pattern data with a database maintained by the International Centre for Diffraction Data. PXRD may also be used to characterise heterogeneous solid mixtures to determine relative abundance of crystalline compounds.[88]

The planes of atoms are labeled with a set of integers $(hkl)$, called Miller indices, which identify the reciprocals of the fractional intercepts which the plane of interest makes with the crystal axes. For cubic crystal the distance $d_{hkl}$ between adjacent Bragg planes is

$$d_{hkl} = a\frac{1}{\sqrt{h^2 + k^2 + l^2}}$$

When a beam of X-rays interacts one of the atoms in the crystal, the X-rays are diffracted in all directions. In general these diffracted waves from different atoms will be, on average, out of phase and cancel out. However, for an X-ray of wavelength $\lambda$ and angle of incidence $\theta$ with respect to a Bragg plane (not the normal to the plane), scattered waves from the various ions lying in a single Bragg plane will be coherent if the angle of reflection equals the angle of incidence, as shown in Figure 2.1. Scattering in this direction from successive planes a distance $d_{hkl}$ apart will be coherent, and will interfere constructively if

$$n\lambda = 2d_{hkl}\sin\theta$$

where $n$ is integer, and this equation is also known as the *Bragg law* of diffraction. Thus the diffracted beam makes an angle $\theta$ with the Bragg plane and the angle

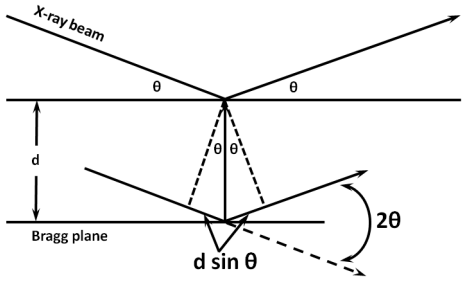


Figure 2.1: Illustration of condition required for Bragg diffraction.

between the incident beam and the diffracted beam is $2\theta$.[89]

## 2.1.2 Application

### 2.1.2.1 Scherrer equation

Powder X-ray diffraction is a common method for determining strain in crystalline materials. An effect of the finite crystalline sizes is seen as peak broadening in an X-ray diffraction pattern as is explained by the Scherrer Equation. By an approximation method, the equation for calculating crystallite size of powder samples could be obtained for the half-width of the diffracted beam in the form of

$$\tau = \frac{K\lambda}{\beta \cos\theta}$$

where $K$ is the Scherrer constant ($2{\cdot}(\ln\frac{\pi}{2})^{1/2} = 0.9503$), $\lambda$ is the wavelength of X-radiation, $\theta$ is half of the diffraction angle, and $\beta$ is the line broadening at half the maximum intensity (FWHM), $\tau$ is the mean size of the crystalline domains. However, the Scherrer equation only provides a lower boundary on the crystallite size due to a variety of factors that contribute to the width of a diffraction peak.

Such factors include inhomogeneities in the sample and instrumental effects.[90]

#### 2.1.2.2 Lattice parameters

The position of a diffraction peak is independent of the type of atoms within the cell and entirely determined by the size and shape of the unit cell of the crystalline phase. Each peak represents a certain lattice plane and therefore can be characterised by a Miller index. If the symmetry of the structure is high, i.e. cubic or tetragonal it is usually not too difficult to identify each peak, then to calculate the corresponding lattice parameters for comparison with the index. This is an important tool in solid solutions, where it is necessary to confirm and identify new materials. The interaction which takes place between X-rays and a crystal involves the electrons in the crystal: the more electrons an atom possesses, the more strongly will it scatter the X-rays. The effectiveness of an atom in scattering X-rays is called the scattering factor, $f_0$. The intensity of a reflection $I_{hkl}$ is proportional to the square of the structure factor $F_{hkl}$, which is dependent on both the position of each atom and its scattering factor.

### 2.1.3 Instrumentation

Powder X-ray diffraction (PXRD) measurements of all the prepared samples were performed on a PANalytical X'Pert PRO diffractometer in Bragg-Brentano geometry using monochromatised Cu $K\alpha 1$ ($\lambda = 0.15418\,\mathrm{nm}$) radiation. (Inorganic Chemistry Laboratory, University of Oxford) The voltage on the anode was fixed at 45 kV and the emission current was set as 40 mA. The diffraction angles ($2\theta$) were scanned over the range between 7° and 80° with a scan rate of $0.03°{\cdot}\mathrm{s}^{-1}$ and a step size of 0.008°. The slit which defines the incident beam was programmed to ensure the

whole sample being irradiated with X-rays throughout the scan, whereas the width of the receiving slit for the diffracted X-rays was at 0.02 mm.

## 2.2 X-ray Photoelectron Spectroscopy (XPS)

### 2.2.1 Introduction

X-ray photoelectron spectroscopy (XPS), also known as Electron Spectroscopy for Chemical Analysis (ESCA), is a quantitative spectroscopic technique that measures surface elemental composition and the chemical and electronic states of the elements. It also characterises the valence band structure that exist within a material. Generally XPS spectra are obtained as a plot of the number of detected electrons by irradiating a material with a beam of X-rays while simultaneously measuring the kinetic energy of the electrons emitted from the top 1 to 10 nm of the material being analysed. It is a surface-sensitive technique when applied to solids. The X-rays employed in XPS penetrate a substantial distance into the sample ($\sim \mu m$). This method of excitation imparts no surface sensitivity at the required atomic scale. If, for instance, electrons of a given energy, $E_0$, are emitted from atoms in a solid at various depths, $d$, below a flat surface. Only those electrons which reach the surface and, at the same time leaving the solid, still have their initial energy ($E_0$) are detected. This is not literally true in an XPS experiment, but in XPS experiments it is only those photoelectrons possessing characteristic emission energies and contributing to the peaks and that will be considered in the subsequent analysis. Photoelectrons which have lost some energy and contribute to the background of the spectrum rather than a specific peak are not considered. The process by which an

electron can lose energy as it travels through the solid is known as 'inelastic scattering'. Each inelastic scattering leads to a reduction in the electron energy and a change in the direction of travel. Apparently if the source atom had been closer to the surface, then a greater fraction of the emitted electrons would have been detected since there would be less chance of inelastic scattering before it escaped from the solid. Therefore, the surface sensitivity must arise from the emission and detection of the photo-emitted electrons. The chemical state information obtained with XPS includes oxidation states and hybridisation states for chemical bonds of the elements. Application of peak fitting routines is generally required to distinguish peaks from overlapping oxidation or hybridisation states.

### 2.2.2 Principles of the technique

The fundamental theory of XPS is based on Einstein's theory of the photoelectric effect as shown in Figure 2.2. The energy of a photon of all types of electromagnetic radiation is expressed by the Einstein relation $E = h\nu$, where $h$ is the Planck constant ($6.62 \times 10^{-34} J{\cdot}s$) and $\nu$ is the frequency (Hz) of the radiation.

A photon (X-ray) passes through a material, it can interact with the electrons in the material. Absorption of the X-ray by an atom in a molecule or solid can lead to ionisation and the emission of a core (inner shell) electron.

The process of photoionisation can thus be considered on basis of

$$A + h\nu \rightarrow A^{+} + e^{-}$$

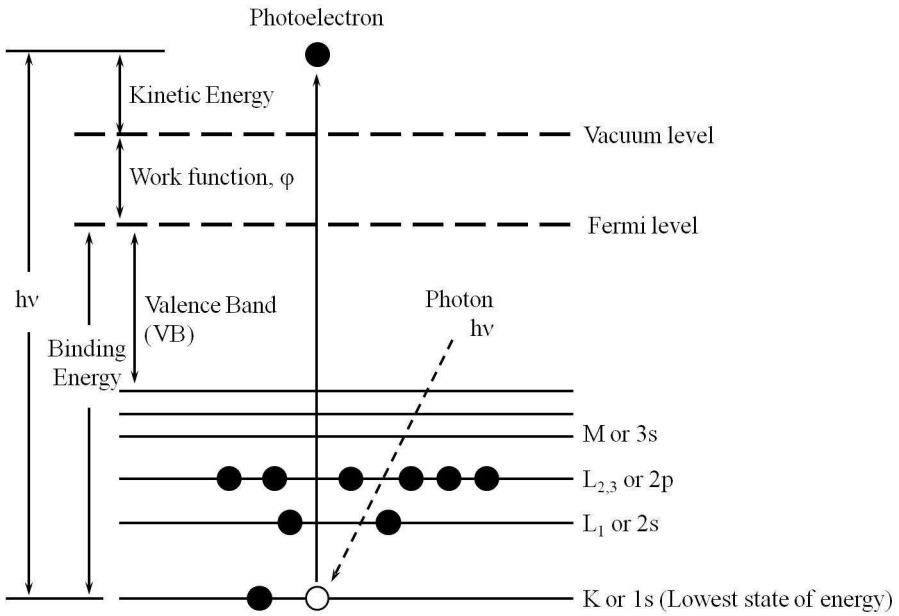


Figure 2.2: Schematic representation of the XPS emission process for a model atom. The incident beam consists of monoenergetic X-rays. The emitted beam is made up of electrons. (diagram adapted from chemwiki.ucdavis.edu)

where $A$ is the atom exposed to X-ray and $A^+$ is its ionised equivalent. This could also be expressed as

$$E(A) + h\nu = E(A^+) + E(e^-)$$

where $E(A)$, $E(A^+)$ and $E(e^-)$ represent the state energies for $A$, $A^+$ and $e^-$, respectively. Since the electron's energy is presented solely as kinetic energy ($KE$), this equation can be rearranged to give the following expression for the photoelectron $KE$

$$KE = h\nu - (E(A^+) - E(A))$$

The difference $(E(A^+) - E(A))$ is generally called the binding energy ($BE$) of the electron, in which commonly expressed as $KE = h\nu - BE$.

This formula is further arranged under the following formula

$$KE = h\nu - (BE + \varphi_s)$$

where $\varphi_s$ is the spectrometer work function.[89]

The binding energy may be regarded as the energy difference between the initial and final states after the photoelectron has left the atom. Because there are a variety of possible final ions states from each type of atom, there are a corresponding variety of kinetic energies of the emitted electrons. Moreover, there is a different probability or cross-section for each final state. Each element has a unique set of binding energies, therefore XPS could be used to identify and determine the concentration of an element on the surface of the material. Variations in the elemental binding energies (the chemical shift) arise from differences in the chemical potential and polarisability of compounds. These chemical shifts could also be used to identify the chemical state of the materials being analysed.

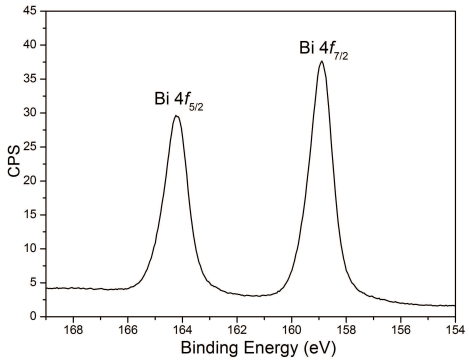


Figure 2.3: XPS core level of Bi $4f$ spectrum consists of spin-orbital splitting with binding energy of 164.1 eV for Bi $4f_{5/2}$ and 158.9 eV for Bi $4f_{7/2}$

Fermi level ($E_F$) is the highest energy level occupied by an electron in a neutral solid at absolute 0 temperature. Electron binding energy ($BE$) is calculated with respect to the $E_F$. The core electrons are local close to the nucleus and have binding energies characteristic of their particular element.

#### 2.2.2.1 Spin orbit splitting

For $p$, $d$ and $f$ peaks, energy splitting of the photoelectron peak is commonly observed in an XPS spectrum, due to the interaction between the spins of the electron, $s$, (up or down) and its orbital angular momentum, $l$. The $s$ orbitals do not split because they have no orbital angular momentum. This interaction leads to a splitting of the degenerate state into two components. The values of spin-orbit splitting of a core level of an element in different materials are nearly the same, as well as the peak area ratios. For instance, the Bi $4f$ electrons are split into two components with different binding energies as shown in Figure 2.3.

Spin-orbit coupling is generally treated using one of two models which correspond to the two limiting ways in which the coupling can occur-these being the $L-S$ (or Russell-Saunders) coupling approximation and the $j-j$ coupling approximation. In light atoms, the interaction between the orbital angular momenta of individual electron is stronger than the spin-orbit coupling between the spin and orbital angular momenta. It can be presumed that the orbital angular momenta of the individual electrons add to form a resultant orbital angular momentum L; likewise, the individual spin angular momenta are presumed to couple to produce a resultant spin angular momentum S. Then L and S combine to form the total angular momentum: $J = L + S$. The total angular momentum determined by the vectorial sum of the total spin angular momentum ($S$) and the total orbital angular momentum ($L$) is called '$L-S$ coupling'. For heavier elements with larger nuclear charger, another coupling scheme is the '$j-j$ coupling'. The spin-orbit interactions become as strong as the interactions between individual spins or orbital angular momenta, where the spin and orbital angular momenta of individual electrons tend to couple to form individual electron angular momenta.

As $s$ orbitals have no angular momentum, electrons in spin-up or spin-down configurations have the same magnitude of total angular momentum. In $p$ orbitals, vector coupling of spin-up and spin-down states with the $\pm 1$ orbital angular momentum vectors give total angular momentum of either $\frac{1}{2}$ (from $\mid 1-\frac{1}{2} \mid$ or $\mid -1+\frac{1}{2} \mid$) or $\frac{3}{2}$ ($\mid 1+\frac{1}{2} \mid$ or $\mid -1-\frac{1}{2} \mid$). These two spin-orbit states have different binding energies, leading to the splitting of the levels. The spin-orbit split levels have different relative occupancies, roughly in proportion to the respective degeneracy of the levels, in

which case $p$ 1:2, $d$ 2:3, and $f$ 3:4.[89, 90]

#### 2.2.2.2 Chemical shift

The chemical shift of a peak's position observed in XPS spectra can be attributed to a change in binding energy of a core electron of an element due to a change in its chemical bonding. In other words, different chemical environments lead to a change of the binding energy of the core level and therefore causes a chemical shift. From a qualitative point of view, core binding energies are determined by the electrostatic effect between the core level and the nucleus. The binding energy is also reduced by the electrostatic shielding of the nuclear charge from all other electrons in the atoms (including valence electrons).[89] The removal or addition of electronic charge as a result of changes in bonding will alter the shielding, in which the withdrawal of valence electron charge will lead to an increase in binding energy whereas the addition of valence electron will cause a decrease in binding energy.

#### 2.2.2.3 Initial and final state effect

There are two main factors that may affect both the apparent position and shape of a photoemission peak of an element, which are called initial-state and final-state effects. The chemical state is an initial-state effect, which is defined before the photoemission process occurs. Factors that occur after the photoemission process can also influence the apparent $BE$ of the photoelectron, which are known as final-state effects. Generally the core and valence band hole ($h^+$) lifetimes are on the order of $10^{-14}$ to $10^{-16}$ second, leading to lifetime broadening on the order of 0.05 eV to as much as 5 eV.

Final-state effect basically consists of five types which are briefly discussed below:

1. *Auger excitation* : Following core ionisation by photoelectron emission an outer shell electron can fill the created vacancy and the energy released can result in the emission of an Auger electron. The energy of an emitted Auger electron will be equal to the emitted photoelectron binding energy minus the binding energy of electron that fills the vacancy in the core, minus the binding energy (in the presence of the core hole) of the level from where the Auger electron is emitted. The process of an excited ion decaying into a doubly charged ion by ejection of an electron is the Auger process. This energy configuration will affect the measured binding energy of the outgoing photoelectron. The consequences are such that the energy gained by filling the initial core hole with an electron is subsequently lost by creation of the second core hole, for a balance that is nearly zero.

2. *Plasmon loss* : There are two types of plasmon loss processes, bulk and surface. The outgoing photoelectron loses energy by interacting via collective oscillations in the bulk of material. The surface plasmon loss occurs when the outgoing photoelectrons interact with surface plasmon states in the material, generally the surface plasmon loss energies are lower than those for the bulk plasmon losses. The net effect of the plasmon loss process is the creation of a new peak or peaks at higher apparent $BE$ than the main XPS peak. The plasmon loss process is quantised, which will give rise to a series of peaks at equally spaced increments in $BE$ above the primary XPS peak. The intensity

of these multiple plasmon-loss peaks decreases with distance from the primary peak. The position of a plasmon loss peak relative to a primary photoemission peak will depend on the type of material. Plasmon loss peaks are broader and generally lower in intensity than the primary XPS peaks. As with inelastically scattered electrons, bulk and surface plasmon loss peaks are not included in the calculations of the total number of electrons emitted from a given orbital for a given element in the sample.[91]

3. *Relaxation*: The relaxation process is a partial filling of the positive charge in the initial hole. This process can occur via a rehybridisation of the atom, in which case it is an intra-atomic process by removing the partial charge from the valence band. Relaxation can also occur by extra-atomic (interatomic) processes, in particular through a process equivalent to diffusion of the localised core hole throughout the valence band of the material. The magnitude of the decrease in $BE$ due to relaxation can be on the order of several electron volts. The magnitude of the relaxation shift can be different for atoms in different chemical environments. It occurs to the same extent for all atoms in a material to the extent that the atoms are in the same chemical and structural state. Therefore it does not typically result in a new peak in an XPS spectrum. It may only be apparent in comparing of the position of a photoemission peak from one sample to another.

4. $Shake-up\ or\ shake-off$ : This process involves rehybridisation of the ion to excite a valence band electron. In the shake-up process, the electronic excitation leads to promotion of a valence band electron. In the shake-off process, the electron is promoted to a higher virtual state. Both shake-up and

shake-off processes create a localised, occupied state above the initial $E_F$ of the material which gives rise to a shift of the $BE$ of the initial hole to higher values. Unlike relaxation, which leads to an overall increase in the background of a spectrum, the shake-up or shake-off processes lead to the appearance of a new peak, called a satellite peak. The position of the satellite peak can be up to a few electron volts in $BE$ above the primary photoelectron peak. The intensity of the satellite peak can be comparable to that of the main peak in some cases.[91]

5. *Multiplet splitting* is similar to that leading to the spin-orbital splitting of $p$, $d$ and $f$ levels, which occurs when the hole created by the photoemission process leaves behind an unpaired electron. Multiplet splitting is particularly important for photoemission from filled $s$ levels in open shell systems, since photoemission always leaves behind an unpaired electron. The unpaired electron in the core can couple with the unpaired electrons in the outer shell and remaining electron spins as either spin-up or spin-down. Both of the two couplings could affect the shift of the position of the orbital, and the magnitude of the splitting is on the order of a few electron volts. The width of the multiplet splitting will be largest for valence $s$ levels, and it decreases in magnitude with the increasing of binding energy.[92]

Initial-state effect also influences the binding energy of the orbital before the photoemission process occurs, which generally includes chemical state shifts and inhomogeneous matrix broadening.

1. *Chemical state shifts* occur between the different chemical states of an atom,

which depends on the type of bond it forms: i.e., metallic, covalent or ionic. Dispersive or hydrogen bonding also play a role, as well as the hybridisation in a covalently bonded system. All these factors affect the partial charge on the atom. However, the differentiation of chemical state information is not this straightforward for all elements, as the background information on final-state effect already suggests.

2. *Inhomogeneous matrix brodening* arises because not all atoms are in exactly equivalent bonding configurations in a material. The $BE$ of an orbital will differ from atom to atom due to localised differences either in composition or structure surrounding each atom.[93]

### 2.2.3 Instrumentation

Electron spectrometers consist of five main components (1) a radiation source; (2) a sample holder; (3) an analyzer, which has the function of monochromator; (4) a detector and (5) a signal processor and readout. Figure 2.4 shows a typical arrangement of these components. Electron spectrometers systems generally require elaborate vacuum systems to reduce the pressure in all of the components to as low as $10^{-8}$ to $10^{-10}$ torr. The sample is placed in an ultrahigh vacuum environment and exposed to a low-energy, monochromatic X-ray beam. The incident X-rays eject core-level and valence electrons electrons from sample atoms. The energy emitted by the photoelectron is a function of its binding energy which is characteristic of the element.

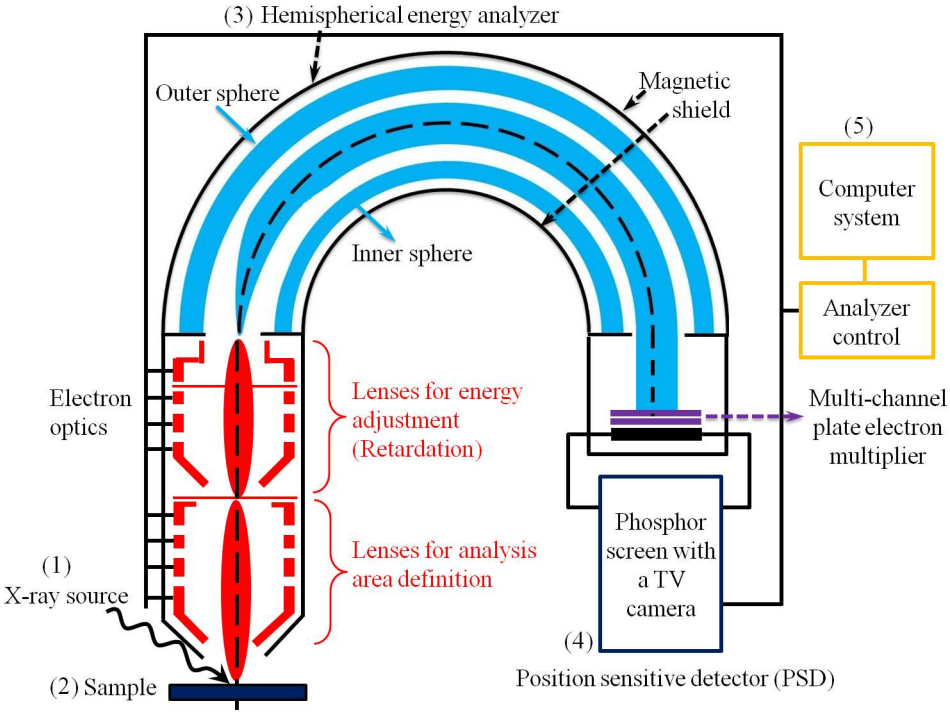


Figure 2.4: Illustration of XPS instrumentation (diagram adapted from casaxps.com)

The high resolution X-ray photoelectron spectra were performed using Scienta ESCA-300 Spectrometer equipped in the National Centre for Electron Spectroscopy and Surface Analysis at Daresbury Laboratory (NCESS), UK. The spectrometer consists of a rotating-anode X-ray source, a 7-crystal monochromator, ESCA 300 hemispherical analyser and a channel plate electron detection system (Figure 2.4). These components are located within a system consisting three chambers operating under ultra-high vacuum (UHV). A complete description of the performance and application of the Scienta ESCA 300 spectrometer has been provided by Beamson *et al.*.[94, 93]

The X-ray source was operated with a 200 mA emission current and a 14 kV anode bias whilst the analyzer operated at 150 eV pass energy with 0.5 mm slits. The Gaussian convolution of the analyzer resolution with a linewidth of 260 meV for the X-ray source gives an effective instrument resolution of 350 meV. Binding energies are referenced to the C 1*s* line which is regularly used to calibrate the spectrometer.

Some of the samples were measured using VG ESCALAB XPS Spectrometer consists of a dual-anode Mg (1253.4 eV) and Al (1486.3 eV) X-ray source, a 5-channel detector with base pressure around $1 \times 10^{-9}$ torr, depth of analysis around 10 nm and variable aperture around 3 to 10 mm.

In *Chapter 3*, *Chapter 4* and *Chapter 7*, X-ray photoelectron spectra were conducted on a Scienta ESCA-300 XPS spectrometer at the National Centre for Electron Spectroscopy and Surface Analysis (NCESS), Daresbury Laboratory, UK. X-rays of energy $h\nu = 1486.6$ eV using a monochromatic rotating anode Al-K$\alpha$ source and a charge neutraliser. The ejected photoelectrons were analysed by a 300 mm mean-radius spherical-sector electron energy analyser with 0.8 mm slits at pass energy of

150 eV. The effective instrumental resolution is 0.45 eV derived from the Gaussian convolution of the analyser broadening and the natural linewidth of the X-ray source (0.27 eV). All the binding energies are referenced to the C 1$s$ peak at 284.5 eV of the adventitious surface carbon. Core level of Bi 4$f$, O 1$s$, Br 3$d$, I 3$d$, Ag 3$d$ and the narrow scan across valence band were identified, respectively.

In *Chapter 6*, X-ray photoemission spectra were recorded on a VG ESCALAB2 XPS spectrometer. All the binding energies were calibrated by referencing C 1$s$ peak to 284.5 eV. Core level of Bi 4$f$, O 1$s$, Br 3$d$, and Ag 3$d$ were identified individually.

## 2.3 Ultraviolet-Visible spectroscopy

### 2.3.1 Introduction

Ultraviolet-visible spectroscopy also known as absorption spectroscopy or reflectance spectroscopy in the ultraviolet-visible spectral region, which means it uses light in the visible and near-infrared ranges. The absorption or reflectance in the visible range directly affects the perceived colour involved of the sample material, in which molecules or continuous solids undergo electronic transitions from the ground state to the excited state. UV-Visible spectroscopy is very useful for exploring the electronic properties of materials, including semiconductors and also materials for the solar energy conversion. In this thesis, UV-Visible spectroscopy has been utilised to characterise the photodegradation extent of the liquid organic dye pollutants, and also the solid samples for the characterising the absorption ability and electronic band gap energy.

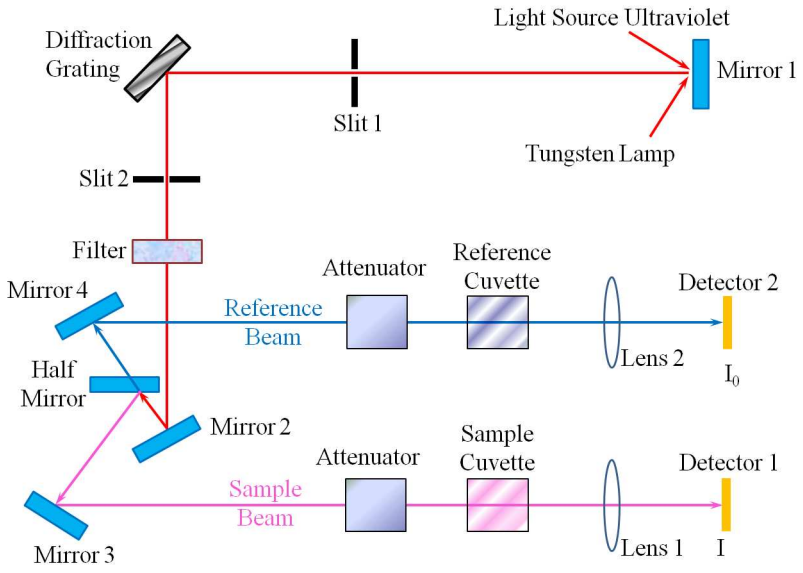


Figure 2.5: Diagram of the components of a typical spectrometer (diagram adapted from chemistry.msu.edu)

As shown in Figure 2.5, a beam of light from a visible and/or UV light source (coloured red) is separated into its component wavelength by a diffraction grating or prism. Each monochromatic beam in turn is split into two beams with equal intensity by a half-mirrored device. The sample beam (coloured magenta) passes through a small transparent cuvette containing a solution of the compound being studied in a transparent solvent. The other beam, the reference (coloured blue), passes through an identical cuvette containing only the solvent. The intensities of these light beams are then measured by electronic detectors and compared. The intensity of the reference beam, which should have little or no light absorption, is defined as $I_0$. The intensity of the sample beam is defined as $I$. Over a short period of time, the spectrometer automatically scans all the component wavelengths in the manner described. Different compounds may have very different absorption maxima. By calculating the relative peak intensity, the photodegradation extent

could be obtained.[90]

### 2.3.2 Materials properties measured by UV-Visible spectroscopy

#### 2.3.2.1 Band gap energy ($E_g$) of semiconductor materials

Electronic excitations in molecules usually occur in the UV and visible regions, and charge transfer bands can occur from the UV to the NIR region. The band gap of a semiconductor material depends on the specific material and can range from the UV to NIR.

In a material with parabolic bands at the band edges, the absorption coefficient $\alpha$ of a semiconductor material is given by the well known equation

$$\alpha h\nu = A(h\nu - E_g)^{n/2}$$

where $\alpha$ is the linear absorption coefficient of the material, $h\nu$ is the photon energy and $A$ is a proportionality constant. As mentioned in Chapter 1, this equation could be used to determine if the semiconductor is indirect or direct transition, depending on the value of $n$.[53]

#### 2.3.2.2 Diffuse reflectance spectroscopy (DRS)

For the powder samples, diffuse reflectance spectroscopy (DRS) is an excellent sampling tool for crystalline materials in the mid-IR and NIR spectral ranges. Diffuse reflectance relies upon the focused projection of the spectrometer beam into the sample where it is reflected, scattered, and transmitted through the sample material (as shown in Figure 2.6). Only the part of the beam that is scattered within a sample

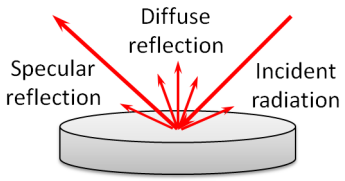


Figure 2.6: Illustration of incident radiation, diffuse reflection and specular reflection

and returned to the surface is considered to be diffuse reflection.

The specular reflectance component of a diffuse reflectance spectra causes changes in band shapes and relative intensity. There are some other factors which related to high spectral quality for diffuse reflectance sampling,

1. **Particle size**-reducing the size of the sample particles may reduce the contribution of reflection from the surface. Generally, smaller particles improve the quality of spectra (narrow bandwidth and better relative intensity), therefore the recommended size of the sample particles is 50 $\mu m$ or less.

2. **Homogeneity**-samples prepared for diffuse reflectance measurements should be uniformly and well mixed as non-homogenous samples will lack reproducibility and will be difficult to quantify.

3. **Packing**-the required sample depth is controlled by the amount of sample scattering, and the minimum necessary depth is around 1.5 mm. The sample should be loosely but evenly packed in the sample holder to maximise spectrometer beam penetration and minimise spectral distortions.

By far the most widely used theory of reflectance spectroscopy is the Kubelka-Munk theory that treats a powdered material as a continuous medium and describes the diffuse reflectance of a sample. Diffuse reflectance spectroscopy is commonly described as the relative reflectance $r_\infty$, where $r_\infty = \frac{r_{sample}}{r_{reference}}$.[95] The absorptive and scattering components can be extracted from the relative reflectance using the Kubelka-Munk equation

$$\frac{k}{s} = \frac{(1 - r_\infty)^2}{2r_\infty}$$

where $k$ is the absorption coefficient and $s$ is the scattering coefficient. Diffuse reflectance spectra make the analysis of a wide range of solid samples easier, faster and more efficient.

### 2.3.3 Instrumentation

The two UV-Visible spectrometers used in this thesis were a Perkin Elmer Lambda 750S and a Varian Cary 5000 UV-visible-NIR instrument. The radiation source in both spectrometers was a tungsten lamp and a deuterium arc lamp, the measurement ranges from 800 nm to 200 nm, with the data collection interval of 1.0 nm and scan speed of 266.75 nm/min and 600 nm/min.

Solid samples require a clean and polished surface to avoid contaminant and scattering losses. Liquid samples containing Rh.B solutions were measured by the Perkin Elmer Lambda 750S with a scan rate of 266.75 nm/min. In *Chapter 3* to *Chapter 7*, the diffuse reflectance spectra were recorded on a Varian Cary 5000 UV-visible-NIR spectrometer with a scan rate of 600 nm/min and $BaSO_4$ as reference, and the solid samples were measured in a sample holder.

## 2.4 Auxiliary techniques of characterisation

### 2.4.1 Scanning electron microscopy (SEM)

Scanning electron microscopy (SEM) provided information about the samples' surface topography and composition. In *Chapter 3*, Scanning electron microscopy (SEM) images were performed on a JEOL JSM 6700F field-emission gun scanning electron microscope. The Energy dispersive X-ray spectroscopy (EDS) was performed on a JSM 840A spectroscopy. In *Chapter 4*, Scanning electron microscopy (SEM) images were performed on a SERION field emission scanning electron microscope. In *Chapter 5*, The morphology of the BiOBr-$ZnFe_2O_4$ were characterised using a Field Emission Scanning Electron Microscopy (S-4800 UHR FE-SEM) with an accelerating voltage of 5.0 kV. The concentration and composition ratio was verified by EDX (SERION ESEM). In *Chapter 6* and *Chapter 7*, FE-SEM images were obtained on a JSM-6700F field emission scanning electron microscope operated at 10.0 kV. The compositions of the samples were tested by EDAX instrument equipped to JSM-6700F microscope.

### 2.4.2 Transmission electron microscopy (TEM)

Transmission electron microscopy (TEM) allows us to examine fine detail of the materials in the application of semiconductor research. Electron energy loss spectroscopy (EELS) was also carried out at the same time to identify each of the compound species in the sample. This device allows for the selection of particular energy values, i.e., different elements in a sample will result in different electron energies in the beam, which could provide information on elemental composition, based upon the

atomic transition during electron-electron interaction.

In *Chapter 3*, transmission electron microscopy (TEM) images were performed on a JEOL-2011 transmission electron microscope fitted with a $LaB_6$ filament operating at an accelerating voltage of 200 kV. In *Chapter 5*, a JEOL 3000F transmission electron microscope equipped with a Gatan imaging filter operated at 3000 kV was used to analyse the diffraction pattern, lattice parameters and lattice fringes of the semiconductor materials.

### 2.4.3 Electron spin resonance (ESR)

Electron spin resonance measures the absorption of electromagnetic energy by a paramagnetic centre in a magnetic field with one or more unpaired electrons. Consequently it is also called electron paramagnetic resonance (EPR) spectroscopy. In the presence of a magnetic field, the degeneracy of the electron spin energy levels is removed and transitions between the energy levels can be caused to occur by supplying energy.[90] The fundamental equation for a paramagnetic center with one unpaired electron could be described as $h\nu = g\beta B$, where $h$ is Planck's constant, $\nu$ is the frequency of the microwaves, $g$ is the g-factor of the electrons, $\beta$ is the Bohr magneton, and $B$ is the strength of the magnetic field in which the sample is placed.

X-band ESR measurements were performed on a Bruker EMX continuous wave (CW) spectrometer at room temperature. All the samples were loaded into quartz ESR tubes (Internal diameter 3 mm). CW ESR spectra were measured with modulation amplitudes between 0.05 mT to 0.5 mT and a modulation frequency of 100 kHz. Measurements were conducted with microwave powers between 10 dB and 44 dB and signals were carefully checked to ensure that they were not saturated at room tem-

perature.

### 2.4.4 Total organic carbon (TOC)

Total organic carbon is generally known as the amount of carbon bound in an organic compound, and has been recongnised as an analytical technique to measure water quality since the early 1970s.[96] A typical analysis for TOC measures both the total carbon present and the so-called 'inorganic carbon' (IC), in which the latter represents the content of dissolved carbon dioxide and carbonic acid salts. Subtracting the inorganic carbon from the total carbon yields TOC. TOC detection is an important measurement, and also a highly sensitive, non-specific technique to evaluate the organics present in a sample which may affect the environment, human health, and manufacturing processes. Low TOC can confirm the absence of potentially hazardous organic pollutant in the water, and it is also of great interest in the application of water purification due to disinfection of byproducts.[97]

In *Chapter 4*, TOC will be utilised to determine the photodegradation extent of the organic dye Rhodamine B at different stage of photocatalytic reactions. The total organic carbon (TOC) of the separated Rh.B solution in the photocatalysis process was measured on a Shimadzu TOC-VCPH instrument.

## 2.5 Photocatalytic degradation of organic dye

Photocatalytic activities were evaluated by the degradation of Rhodamine B (Rh.B) aqueous solution under visible-light irradiation. The optical system used for the photocatalytic reaction consisted of an overhead 300 W Xenon lamp (PLS-SXE 300, Beijing TrustTech) equipped with a UV cutoff filter (UVCUT 400, Beijing Trust-Tech), the filter was attached to the lamp source to remove all incoming wavelengths

shorter than 400 nm to ensure irradiation with visible-light only. In each experiment, 0.1 g photocatalyst was dispersed into 100 mL of Rh.B in aqueous solution (20 mg/L) in a 500 mL beaker. Prior to irradiation, the suspensions were syncopated in dark for 1 h to ensure the establishment of absorption-desorption equilibrium of the dye on the surface of catalysts. During the absorption and irradiation process, at time intervals of 5 min, approximately 3 mL of suspension is collected and then the slurry samples including the photocatalyst and Rh.B solution were centrifuged (14000 rpm, 4 min) to remove the photocatalyst particles. The solutions were analysed by a Perkin-Elmer Lambda 750S UV-Visible spectrophotometer, and the intensity of the characteristic absorption peak of Rh.B at 553 nm is used to determine the extent of Rh.B degradation. Because the photocatalysis process is following a first-order kinetics law, the apparent reaction kinetics constant can be derived from a plot of $\ln(C/C_0)$ against irradiation time.[98]

For the stability measurements, 0.2 g photocatalyst was dispersed in 200 mL of Rh.B solution (20 mg/L) and the photoactivity tested as described above. After each photoactivity test, both the separated catalyst particles and the solution were returned to the reaction system. Photocatalysis stability tests were performed in five separated runs. In *Chapter 4*, once these tests were completed the photocatalyst was reclaimed, washed, dried over night at 65 °C and then analysed by XRD and XPS.

# Chapter 3

# Ultrasound-induced BiOBr assemblages

## 3.1 Overview

The hierarchical architectures of nano-crystals often result in unique properties and exceptional performance which depend significantly on the morphology, shape, orientation geometry and crystal surface of the constituent nano-blocks. However, the manipulation of assemblages with three-dimensional (3D) structure remain a formidable mission due to enormous thermodynamic, kinetic and technical challenges arising from the complexity of the structures of the constituent nanoblocks. In the past decades, exploring new chemical synthetic methodologies with the aim of reduction in time and energy consumption towards environment has become a great concern for the society of human beings. Here, in this chapter, a rapid and effective ultrasonification synthesis has been developed to fabricate flower-like assem-

blages of BiOBr nano-flakes without the involvement of organic constituents; they exhibit both excellent photocatalytic activity and photo-stability under visible-light irradiation. A mechanism for the ultrasound-induced orientational assembly of these flower-like BiOBr architectures is proposed here, which provides insights into the role of sonification in the synthesis of self-organised nano-crystals and micro-crystals in the application of crystal surface engineering.

## 3.2 Introduction

Three-dimensional (3D) assemblies of nano-/micro-crystal photocatalysts generally outperform both their constituent nano-scale building blocks and their corresponding bulk materials in important applications such as photocatalytic environment remediation, solar fuel generation and solar cells.[42, 1, 99, 80, 15, 98, 4] The enhanced photo-response and photocatalytic performance of the assemblages are closely related to their intrinsic high surface-to-volume ratio, facile transportation of reactants, anti-aggregation and easy recycling.[100, 101] However, it is accepted that assembling such structures from finite-scale crystals represents a thermodynamically non-spontaneous process with a significant reduction of the systems entropy and consequently necessitates either additional energy input or special reagents to enhance or catalyse the nucleation, growth and elaborate assembly of constituent nano-blocks.[102, 103, 104, 105, 106] The hierarchical architecture of semiconductor nano-crystals have been successfully fabricated through either template-directed or non-aqueous syntheses with sophisticated procedures.[1, 99, 80, 15, 100, 101, 107, 7] The nano-blocks can also be assembled using external force fields (e.g. magnetic,[108, 109] electronic,[110, 111]

and microwave,[80] etc.) to self-organise the nano-blocks.[103, 112]

Bismuth oxybromide (BiOBr) possesses a lamellar crystal structure, and an attractive electronic energy band gap ($E_g$ = 2.9 eV) for sunlight harvesting. BiOBr has recently been demonstrated to show exceptional visible-light-responsive photocatalytic activity and photo-stability.[80, 81, 113] In particular, assembled BiOBr photocatalysts exhibited superior performance as compared to bulky and randomly arranged BiOBr nano-flakes.[80, 113, 114, 115] Although various chemical methodologies have been developed to prepare the BiOBr nanostructures, in non-aqueous solvents and/or with the assistance of organic templates;[80, 98, 81, 113, 114, 115] the target of creating 3D hierarchical architecture remains tremendously challenging. For instance, hydrolysis synthesis can lead to poor crystallinity and failure to tune the assembly and morphology of the particles. Micro-emulsion and solvothermal synthetic methods are successful in the formation of 3D assemblies of nano-particles, though time/energy-consuming, and/or environmentally unfavourable.[113, 116, 68, 69] Hydrothermal synthesis may adjust the morphology and crystallinity of BiOBr. Additionally, the assistance of expensive surfactants is a prerequisite in fabricating 3D assemblies.[81] All such synthetic protocols can either be energy inefficient, time-consuming or potentially harmful to the environment.[117] Therefore an attractive tailored synthesis of BiOBr hierarchical nanostructures in more environmentally compatible aqueous solutions, without the use of organic reagents, has yet to be realised.

In this chapter, a rapid ultrasonification synthesis method for preparing nano-/micro-crystal BiOBr assemblages with individual structures exhibiting a flower-like morphology-somewhat akin to that of the peony flower. We also propose a formation mechanism elucidating the roles of ultrasound on the assembly of BiOBr nano-flakes.

Sonochemical synthesis has been shown to be a highly effective and environmentally benign methodology for preparing nano-structured functional materials.[118, 119, 120, 121] However, the ultrasound-induced self-assembly of nano-blocks to larger, microscopic or mesoscopic structures has yet to be achieved.

## 3.3 Experimental

In a typical experiment, flower-like BiOBr crystallites were synthesised via the ultrasonic treatment of aged BiOBr precipitates (hereafter BiOBr$-CP$; $CP$ denotes Co-Precipitation method) which were obtained from mixing $Bi(NO_3)_3 \cdot 5\,H_2O$ and aqueous KBr solutions and aged for 5 min prior to the sonification process. Such sonochemically produced BiOBr materials are labeled here as BiOBr$-US-t$, where $US$ and $t$ denote ultrasonification treatment and its duration in minutes, respectively. Such BiOBr 'flowers' exhibited both exceptional photoactivity and high stability with respect to photo-degradation of dye under visible-light irradiation.

All chemical reagents involved were used without further purification. Ultrasonification treatments of BiOBr samples were performed in a 3 L ultrasound cleaning bath (KQ 2200E, 220 V, 50 Hz) under ambient conditions. The power and frequency of the generated ultrasonic wave was 100 W and 40 kHz, respectively. A 50 mL 0.33 mol/L KBr aqueous solution was rapidly poured into 100 mL $Bi(NO_3)_3 \cdot 5\,H_2O$ aqueous solution (5 mL HAc in 95 mL distilled water, containing 33 mmol $Bi(NO_3)_3 \cdot 5\,H_2O$) under rigorous stirring. Upon the addition of KBr solution, pale yellow precipitates were produced to form a suspension. The suspensions were aged 5 min prior to treatment by ultrasonic irradiation for various durations (10, 15, 20 and 30 min). The precipitates obtained after ultrasonic treatment were further aged for 6 h before

careful centrifugation and washing with distilled water and ethanol, and then dried at 60°C overnight. The BiOBr obtained samples were labeled as BiOBr$-US-t$, where $-US$ and $-t$ denote ultrasonification synthesis and its duration, respectively. For comparison, a BiOBr$-CP$ sample was synthesized by co-precipitation under similar conditions without ultrasound irradiation. Specimens were also prepared by ultrasonic treatment for 20 min and 60 min but without the initial 5 min aging.

## 3.4 Results and discussions

### 3.4.1 Crystal structure

Powder X-ray diffraction patterns (PXRD) of the BiOBr materials derived from different synthetic methodologies, ultrasound and co-precipitation are compared in Figure 3.1 A, where all the Bragg diffraction peaks can be indexed to the tetragonal BiOBr (JCPDS: 78-0348, space group $P4/\mathrm{nmm}$, a = 3.92 Å, b = 8.11 Å).[81] Despite the fact that all the BiOBr products have identical crystal phase, they exhibit different diffraction features. The relative intensities of the (110) and (200) diffraction peaks of the BiOBr$-US-15$ are noticeably stronger than those of BiOBr$-CP$, implying the BiOBr$-US-15$ flakes are found to either grow as orientationally ordered or organise along the [$hk$0] and [$h$00] crystal axes.[98, 115] It can be observed from the XRD patterns that the characteristic diffraction peak (110) is narrower than the (102) peak, the broadening of the diffraction peak (102) could be attributed to several factors, such as not enough long-range order in that direction, irregular

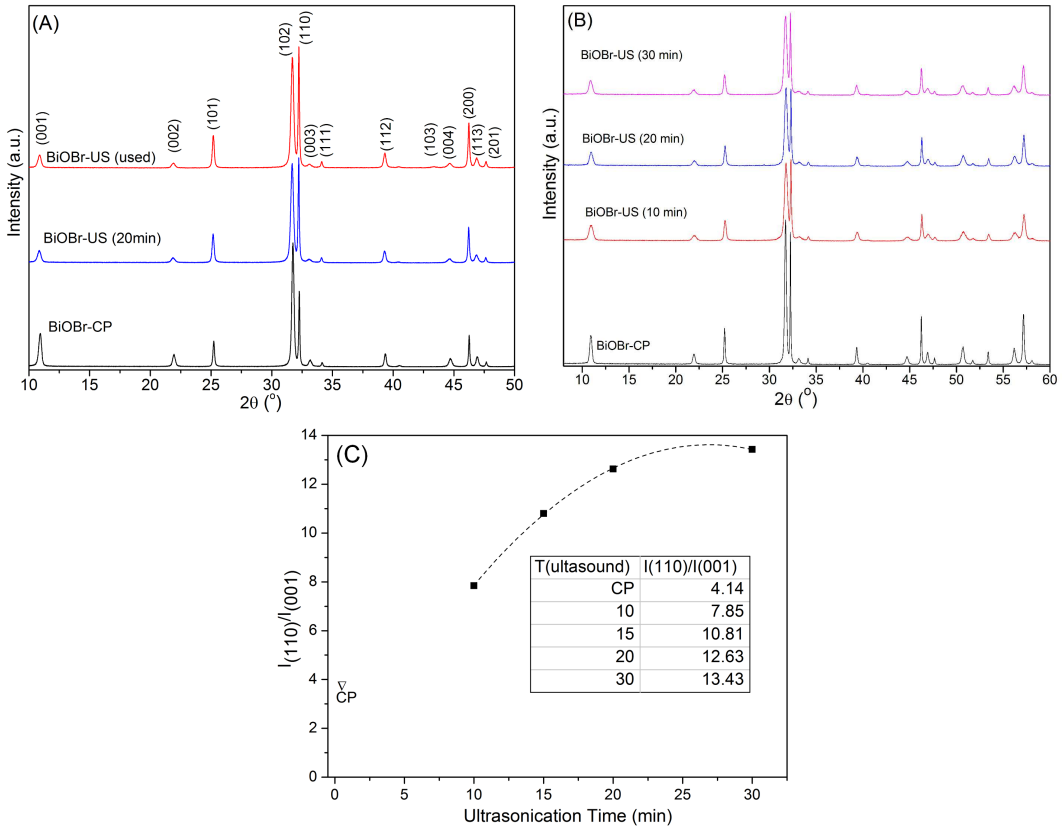


Figure 3.1: (A) Powder X-ray diffraction patterns of BiOBr−*CP* and BiOBr−*US* − 15 samples both before and after photo-reaction; (B) XRD pattern of BiOBr samples prepared via ultrasonification method with different time and (C) Ratio of (110) to (001) diffraction intensities of BiOBr-*US* samples as a function of ultrasonification time.

arrangement in the periodic order and some crystal defects in the direction though the long-range order is enough.

Further study of the PXRD data of a series of BiOBr$-US-t$ samples indicates that the enhanced ($hk$0) and ($h$00) diffractions depended critically on the ultrasonic treatment duration (see Figure 3.1 B), and therefore lead to a special specimen morphology which was identified by SEM and TEM characterisations. As can be seen from Figure 3.1 C, the intensity ratio of (110) to (001) Bragg diffraction peaks $\left(I_{(110)}/I_{(001)}\right)$ are 12.63 and 4.14 for the BiOBr$-US$ and BiOBr$-CP$, respectively, suggesting the preferential orientation of the BiOBr$-US-t$ samples is (110) rather than the (102) facet compared to the BiOBr$-CP$ sample. It is reasonable to infer that the ultrasound irradiation plays the key role in the preferential orientation of the BiOBr$-US-t$ sample, in which the peak intensity ratio $I_{(110)}/I_{(001)}$ was found to increase systematically along with the increasing ultrasound irradiation time from 10 min to 30 min. However the trend in $I_{(110)}/I_{(001)}$ as a function of ultrasonification time for BiOBr$-US$ samples is non-linear, revealing that the influence of ultrasonification on the anisotropic growth rate of BiOBr decreased with prolonged ultrasound irradiation time.

### 3.4.2 Morphology

Scanning electron microscopy images (SEM) reveal that the BiOBr$-US-15$ sample consists of micro-particles with a flower-like architecture, which is akin to

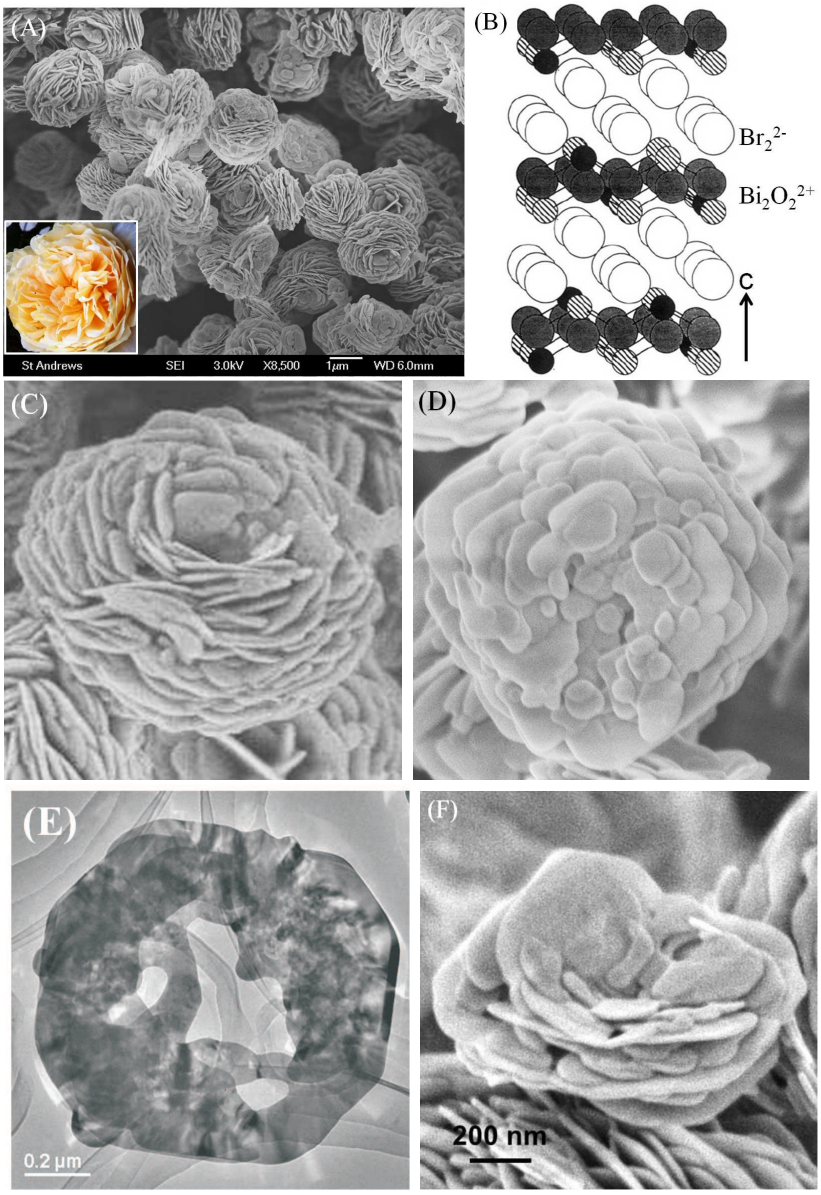


Figure 3.2: (A) A SEM image of the BiOBr$-US-15$ assemblages showing the peony-like individual particles, and the inset is a photograph of a peony flower; (B) Simplified structural model of BiOBr; (C) and (D) Enlarged SEM images with respect to face and bottom of the peony-like particles; (E) TEM image of a very large single octagon-shaped nano-flake with a hollow centre, and (F) SEM image of an early stage peony-like particle.

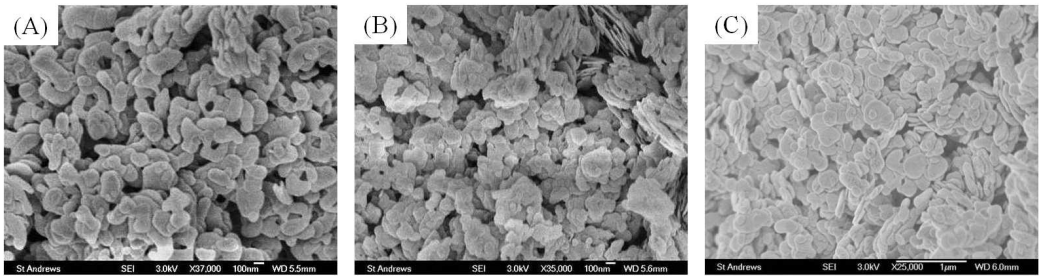


Figure 3.3: (A) SEM image of BiOBr samples synthesised with immediate ultrasound irradiation durations of 20 min and (B) 60 min, respectively; and (C) BiOBr$-CP$ sample.

a peony flower (insert in Figure 3.2 A), with a uniform diameter of approximately 2 μm (Figure 3.2 A). The individual flower-like particles (Figure 3.2 C, D) are constructed hierarchically by a number of thin nano-flake 'petals' with average thickness of approximately 20 nm and diameters in the range of 200 nm to 500 nm. In the BiOBr$-US-15$ 'micro-flower', the adjacent nano-flakes are joined with a small incident angle of less than 30°. Perpendicularly or randomly stacked nano-flakes were typically observed in other BiOBr flower-like architectures synthesised via previously reported methodologies.[80, 98, 113, 114, 115]

The SEM images of BiOBr$-US-t$ specimens (Figure 3.3 A and B), synthesised under immediate ultrasound irradiation without any ageing process, revealed the samples are also randomly attached without a flower-like assembled morphology. The BiOBr$-CP$ specimen contains loosely-attached micro-flakes rather than 3D self-assembly as shown in Figure 3.3 C. The SEM characterisations suggest both

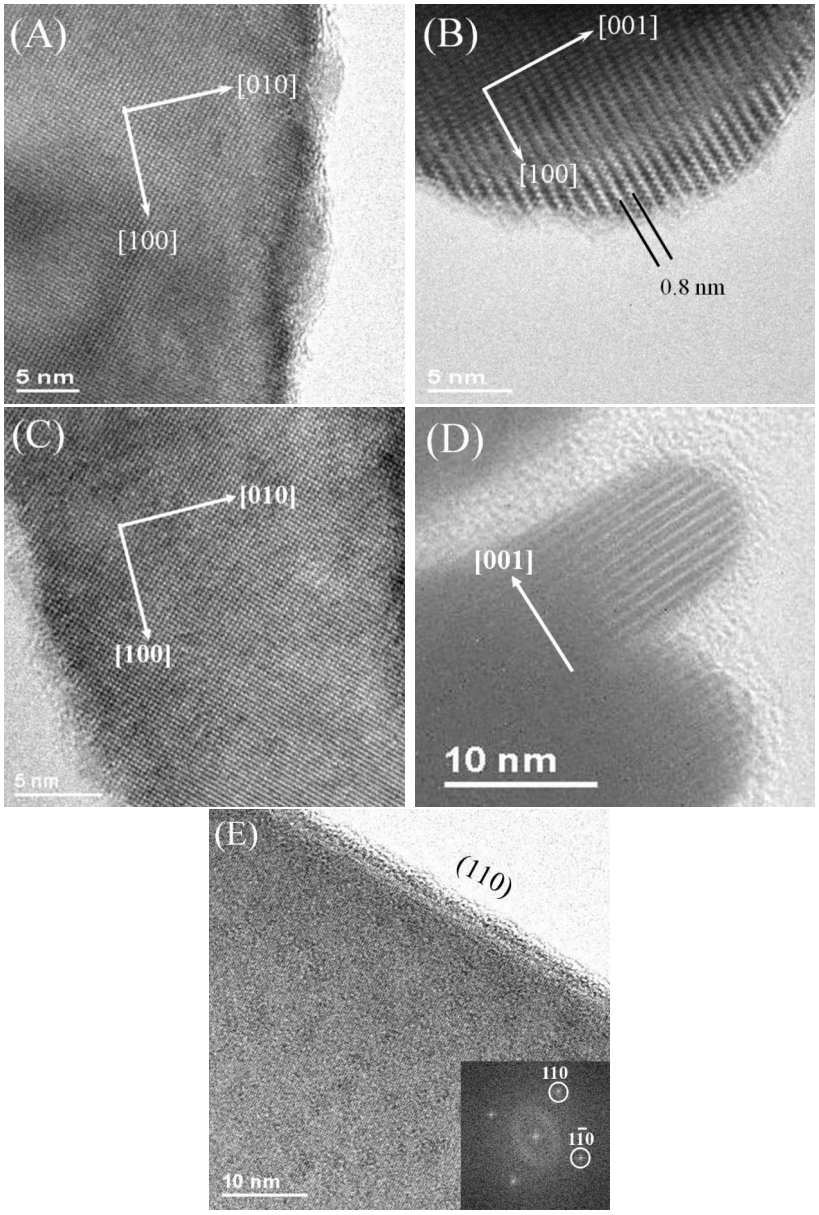


Figure 3.4: HRTEM images from (A, B) BiOBr$-CP$ and (C, D) BiOBr$-US-15$; (A and C) viewed down the short axis of BiOBr nano-flakes, (B) and (D) are profile images of the nano-flakes; and (E) HRTEM image of an octagon-shape nano-flake showing the terminated flat surface is along the [110] axis, the inset is the corresponding FFT pattern.

the ageing and ultrasonic treatments are critical for forming such 'micro-flowers' morphology of the BiOBr samples. The particles are aggregated along the {001} surface without angular alignment. A number of the nano-flakes with the diameter larger than 500 nm were observed from the samples after ageing, while no such large nano-flakes were detected in the samples without ageing. It was found that the key effect of ageing is to increase the diameter of the nano-flakes as evidenced by particle sizes measured via SEM for 300 nm to 500 nm particles for each BiOBr sample. The increase of the particle size not only leads to the increase of the intensities of the diffraction peaks of (110) and (200) (Figure 3.1 A and C), but also becomes a crucial factor for the subsequent formation of the flower-like aggregates. The crystal structures of the BiOBr$-US$ and BiOBr$-CP$ nano-flakes were confirmed by high resolution transmission electron microscopic (HRTEM) images (Figure 3.4). The short axes of the BiOBr nano-flakes are always along the [001] zone axis, suggesting that the major flat surface of the BiOBr flake is associated with {001} crystal face.

### 3.4.3 Surface elemental analysis

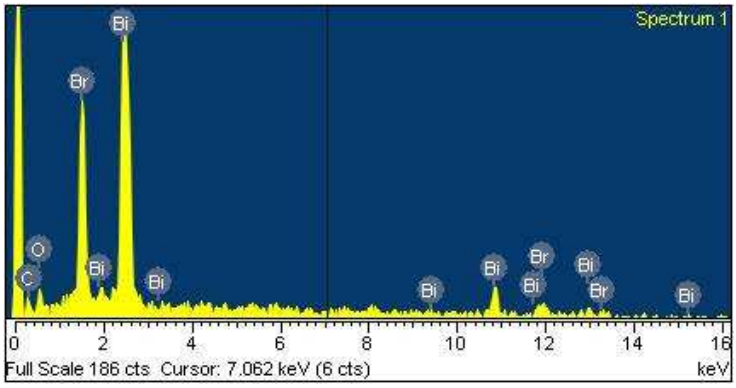


Figure 3.5: Energy Dispersive X-Ray Spectroscopy (EDS) spectrum of the as-synthesised BiOBr$-US-15$ sample

Table 3.1: Experimental elemental ratio of BiOBr sample taken from Energy Dispersive X-ray Spectroscopy

| Element | Weight percentage (%) | Atomic percentage (%) | Atomic ratio |
|---|---|---|---|
| C | 13.66 | 56.59 | - |
| Bi | 56.47 | 13.44 | 1.0 |
| O | 4.57 | 14.22 | 1.06 |
| Br | 25.29 | 15.75 | 1.17 |
| Total | 100 | 100 | - |

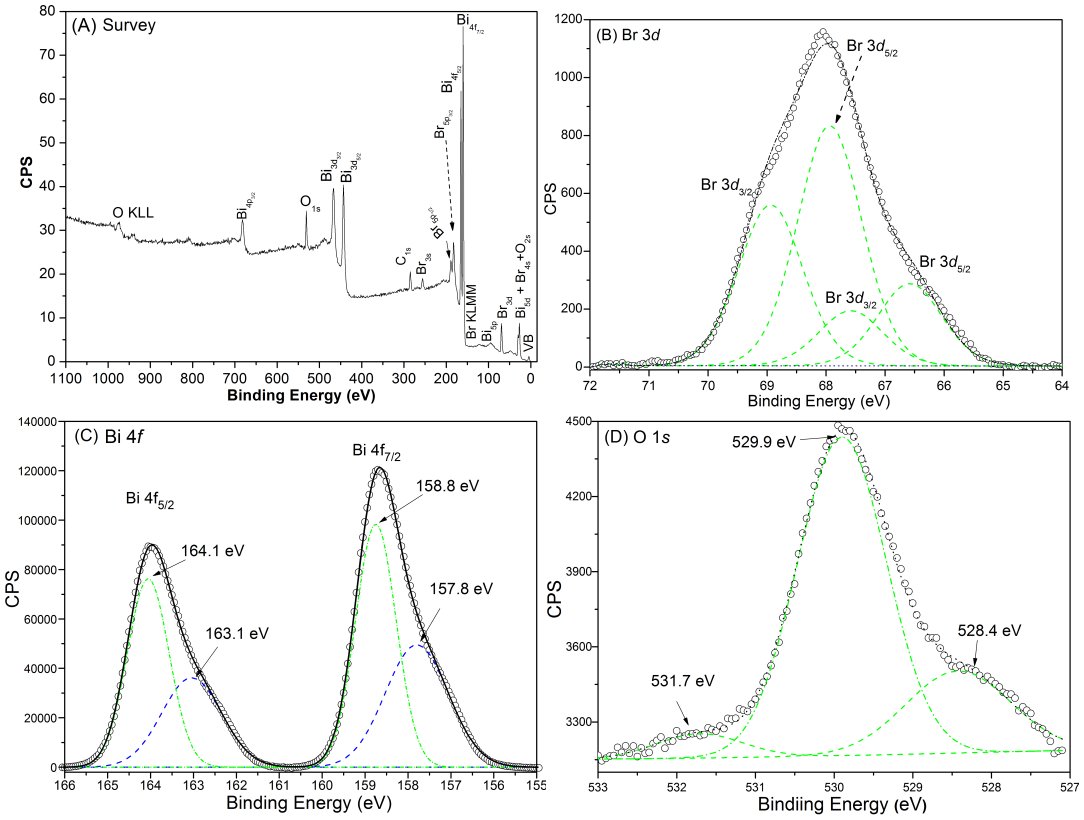


Figure 3.6: XPS spectra of BiOBr$-US-15$ (A) survey; (B) Br $3d$; (C) Bi $4f$ and (D) O $1s$

The chemical composition of the flakes matches the composition of BiOBr as verified by energy dispersive X-ray spectroscopy (EDS) and X-ray photoelectron spectroscopy (XPS). (Figure 3.5) The EDS spectrum reveals that the sample is composed of Bi, O and Br and the atomic molar ratio has been calculated derived from the EDS data (Table 3.1), which is $n_{Bi} : n_O : n_{Br} = 1.0 : 1.06 : 1.17$. The result is consistent with the BiOBr composition. The surface composition of the BiOBr$-US-15$ sample was analysed by high resolution X-ray photoelectron spectroscopy (HR-XPS). XPS survey spectrum (Figure 3.6 A) reveals that the sample is composed of Bi, O and Br. They all occupy equivalent position within the crystal structure. The curve fitted high resolution XPS spectra of the individual element are shown in Figure 3.6 B-D. The curve fitting procedure deconvolutes the Br $3d$ envelope into two sets of spin-orbit doublets as shown in Figure 3.6 B. The positions of main Br $3d_{3/2}$ and Br $3d_{5/2}$ peaks fall in the ranges of 71$\pm$ 0.5 eV and 68$\pm$1.5 eV, which is characteristic of $Br^-$ in BiOBr materials. Two other peaks centred at 67.5 and 66.5 eV (relating to the Br $3d_{3/2}$ and Br $3d_{5/2}$ peaks) are found and very possibly arise from the charge neutralisation. Two strong peaks at 164 eV and 158.7 eV in the Bi $4f$ spectra were attributed to $4f_{5/2}$ and $4f_{7/2}$ of $Bi^{3+}$, respectively. The individual peak of Bi $4f$ was curve fitted into two peaks at 164.1 and 158.8 eV corresponding to $Bi^{3+}$ $4f_{5/2}$ and $4f_{7/2}$ in O-Bi-O bonds of the $[Bi_2O_2]$ slabs, which are consistent with those in $Bi_2O_3$ and Bi-doped $TiO_2$. These fitted binding energy values for $Bi^{3+}$ $4f_{5/2}$ and $4f_{7/2}$ with 3:4 area ratios well agreed to the quantum selection rules of XPS technique.[92] The O $1s$ spectrum, with a main peak at 530 eV, was also curve fitted into three peaks at 528.4 eV, 529.5 eV and 531.7 eV, in which the strongest peak at 529.5 eV is assigned to the Bi-O bond in the $[Bi_2O_2]$ slabs. due to its weak interactions with the intercalated

$Br^{-1}$. The binding energy 531.7 and 528.4 eV is attributed to the contribution of the surface hydroxyl (-OH) groups.[122] The multiplet splitting of the core lineshapes could be observed in all the elements, suggesting that charge neutralisation has not produced a homogeneously neutralised surface. This phenomenon might be caused by the special flower-like morphology.

### 3.4.4 Formation mechanism

Since no organic reagents were used in the ultrasonification synthesis, the accepted mechanisms of crystallisation and subsequent orientation attachment are not plausible to understand the self-assembly of such BiOBr$-US-t$ micro-flowers.[103, 104, 108, 112] Through detailed TEM/SEM investigation of the morphology and microstructures of our BiOBr$-US-t$ samples, an ultrasound-assisted self-assembly mechanism for such peony-like assemblies is proposed here. As illustrated in Figure 3.7, the assembly of these hierarchical peony-like BiOBr crystals involves the sequential processes of nucleation, ageing, surface erosion and the ultimate organised deposition of successive, individual nano-flakes under the influence of ultrasound irradiation.

The nucleation of BiOBr occurred immediately once the aqueous solution containing of $Bi^{3+}$ and $Br^{-}$ were mixed. The measured average particle size for 300 nm to 500 nm particles of the BiOBr with 5 min ageing suggests that the key effect of ageing is to increase the average diameter of the nano-flakes. With both ageing and subsequent sonification treatments, a number of large BiOBr nano-flakes approximately 500 nm were observed from the BiOBr$-US-t$ samples, but importantly there are no such large nano-flakes in the BiOBr$-US$ samples synthesised without

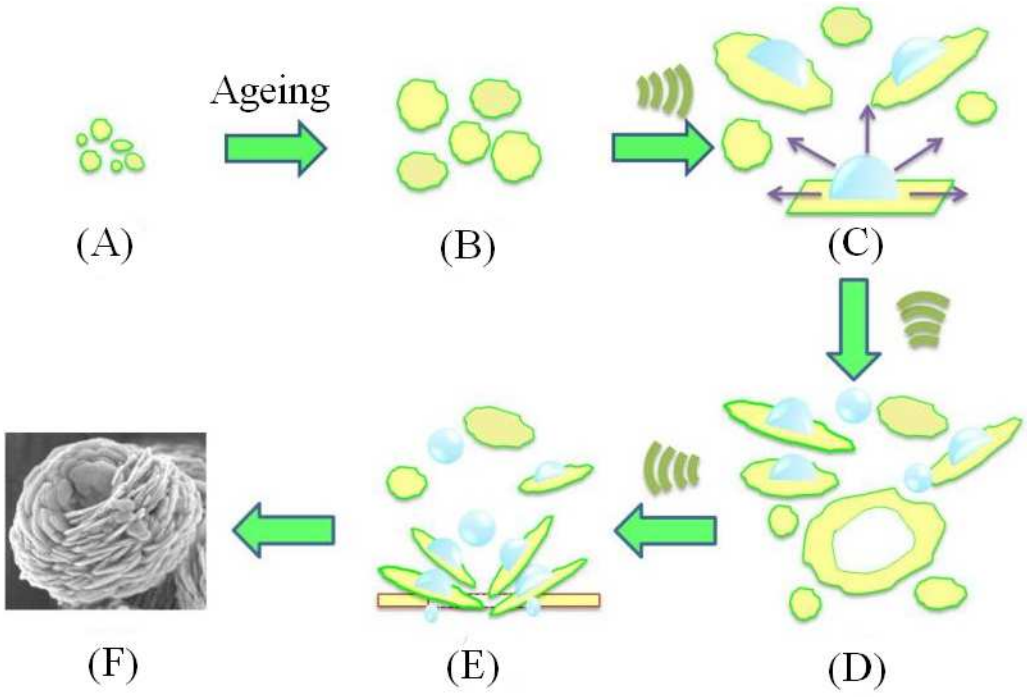


Figure 3.7: Schematic representation of the proposed step-by-step formation mechanism of flower-like BiOBr particles: (A) nano-flakes, (B) larger sized nano-flakes after subsequent ageing, (C) sonification-induced bubbles form on the surface of nano-flake, (D) a small hole induced by bubble collapsing on a large flake, (E) and (F) a large hole to form a hollow octagon, followed by successive deposition of further small nano-flakes with inclined positions to yield the flower-like structure.

ageing but direct ultrasonification (see Figure 3.3).

It has been proposed that a vast number of micro-bubbles are generated by ultrasound cavitations and thus significantly damage the surface of the nano-flakes (Figure 3.7 C).[119, 121, 123, 124] Transient and localised high temperatures and high pressures (∼1800 K and 1000 bar) associated with the bubbles allow this significant energy transfer to the solid surface, leading to fast crystallisation but also concomitant surface erosion.[119, 121, 125] It is reasonable to expect that small holes

can be created on the large flakes through ultrasound erosion (Figure 3.7 D). Various levels of developing, sonification-induced damage on the nano-flakes were indeed observed in the detailed SEM (Figure 3.2 E) and TEM examinations (Figure 3.8).

Further ultrasonic treatment ultimately results in a large 'hole' across the flat {001} planes (Figure 3.8 D). The holes are created by significant erosion of the large flakes, whilst the nano-flake changes to an octagon flake with smooth edges associated to {110} and {100} planes. We found that such damage can only be observed on large flakes (approximately 500 nm or larger in diameter in the present case). In other words, ultrasonification erosion requires a sufficiently large flake, on which bubbles 'punch' through the {001} planes of surface area. The prolonged ultrasonic treatment, typically 60 min, leads to destruction of the majority of ring-shaped crystals due to the harsh local temperature and pressure of the ultrasonic treatments (Figure 3.8 B).[119, 118, 125, 123]

During sonification, large nano-flakes with holes in the aged BiOBr serve as a base or initiator for the subsequent assembly of growing BiOBr nano-flakes, ultimately leading to hierarchical 'micro-flower' structures. The first group of nano-flakes deposit on the hole of the hollow octagon base-flake. This hinders the deposition of nano-flakes on its back-side (Figure 3.7 E). In addition, some small BiOBr flakes and small bubbles can 'wedge' the adjacent flakes and prevent continuous parallel stacking of the deposited BiOBr flakes along the {001} planes but, importantly, tilts them at a small angle (Figure 3.7 F). Within such a micro-flower, no parallel connection can be found between any two nano-flakes except for few small flakes perching at

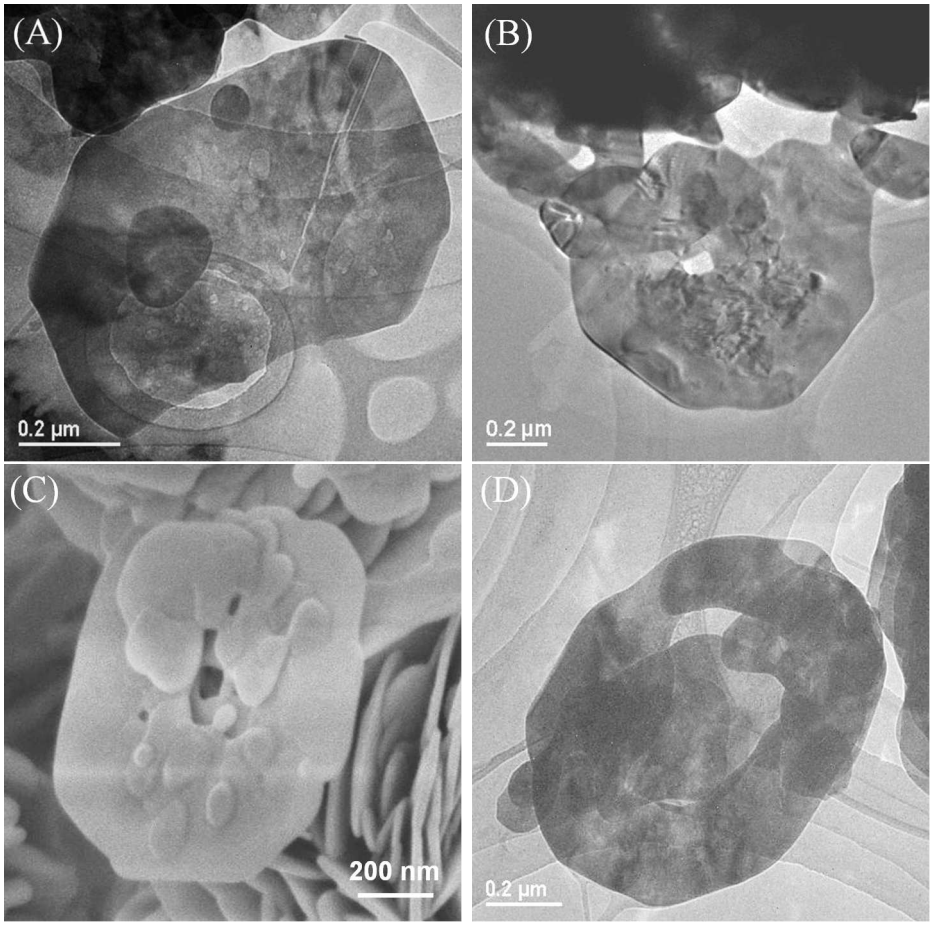


Figure 3.8: Erosion of BiOBr nano-flakes after 15 min ultrasonic treatment: (A) TEM image of a nano-flake showing the central area contains many defects, but the edge area is intact; (B) TEM image of a nano-flake with a small hole and damaged surrounding area; (C) SEM image of a nano-flake with a small hole; and (D) TEM of a nano-flake with a large hole.

its base (Figure 3.2 C and D). Considering the surface composition of BiOBr, the most likely termination would be in a $Br^-$ layer to give a repeating quadrupolar sequence of charges. The strong attraction between oppositely-charged surfaces of the nano-flake is expected, but the identically-charged surfaces would clearly repel each other and inhibit the formation of larger clusters.[112] After ultrasound irradiation, the damaged 'holes' of the BiOBr flakes terminated with {110}, {010} and {100}, while the nano-flakes self-organised orientationally with the {110} and {100} flat faces outwards. Both factors will result in increased exposure number of {110} and {200} surfaces in a consequence of enhanced (110) and (200) Bragg diffraction intensities for the BiOBr$-US-t$ materials.

### 3.4.5 UV-Visible diffuse reflectance spectra of BiOBr

The UV-Visible absorption spectra (Figure 3.9 A) reveals both the BiOBr$-US-$15 and BiOBr$-CP$ can absorb visible light up to wavelengths of 450 nm. The electronic band gap energy of these materials is approximately 2.90 eV. The plots of $(\alpha h\nu)^{n/2}$ versus $h\nu$ (n=1 for indirect and n=4 direct semiconductor) in the band gap region of BiOBr$-US$ have been shown in Figure 3.9 B, where $\alpha$ and $h\nu$ are the absorption coefficient and the discrete photon energy, respectively.[80, 98, 81, 113] The linear plot of $(\alpha h\nu)^{1/2}\sim h\nu$ verifies the indirect transition of photo-generated electrons through the band gap region of BiOBr. The indirect transition is widely regarded as an important factor to elongate the transfer and mean-free path of photo-generated electrons thereby retarding their recombination with photo-generated holes.[81, 126] Light absorption of BiOBr$-US-15$ is stronger than that of BiOBr$-CP$ across the broad UV-Visible region, and the enhanced light absorption of the BiOBr$-US-15$

is attributed to the hierarchical, flower-like 3D structure synthesised by the sonochemical technique. As schematically shown in inset of Figure 3.9 A, the hierarchical flower-like 3D architectures of the BiOBr$-US-15$ can considerably attenuate incident light and, importantly, thus suppress energy losses by reflection. The similar attenuated light scattering had ever been observed for hierarchical nano-porous structures synthesised using a bio-template.[108]

### 3.4.6 Photocatalytic performance

The results of Rh.B photo-degradation experiments (Figure 3.10 A) reveal that the photocatalytic activity of the ultrasonification produced flower-like assemblages are superior to that of BiOBr synthesised by conventional co-precipitation routes. The characteristic absorption of Rh.B at 554 nm completely disappears in the BiOBr$-US-15$ and BiOBr$-CP$ systems within 10 min and 40 min visible-light irradiation, respectively. The concentration of Rh.B remained unchanged in the absence of photocatalysts and less than 50% Rh.B decomposed over commercially sourced $TiO_2$ P-25 (Degussa P-25), even after two-hour visible light irradiation. The bleaching of Rh.B on P-25 $TiO_2$ arises from dye-sensitised photodegradation since $TiO_2$ can only be activated by UV light due to its large band gap ($E_g = 3.2$ eV).[98, 114]

The superb activity of BiOBr systems, which decompose Rh.B in such a short period, suggests photocatalysis rather than dye-sensitisation is the dominant factor in

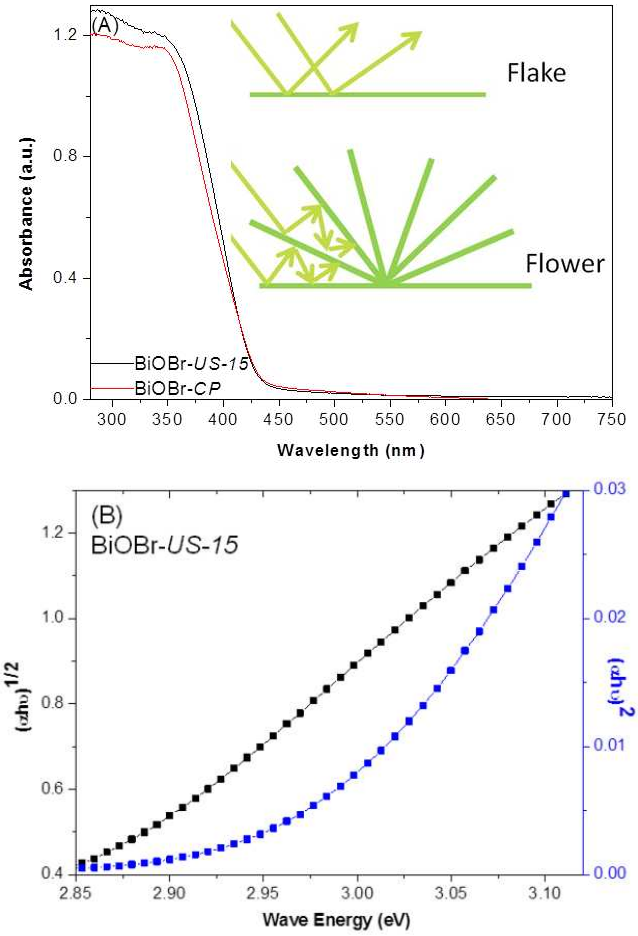


Figure 3.9: (A) UV-Visible absorbance spectra of BiOBr$-US-15$ and BiOBr$-CP$. The inset is schematic illustration of light absorption process occurring on the surface of BiOBr samples with different surface morphologies; and (B) the plots of $(\alpha h\nu)^{n/2}$ *versus* h$\nu$ of BiOBr$-US-15$.

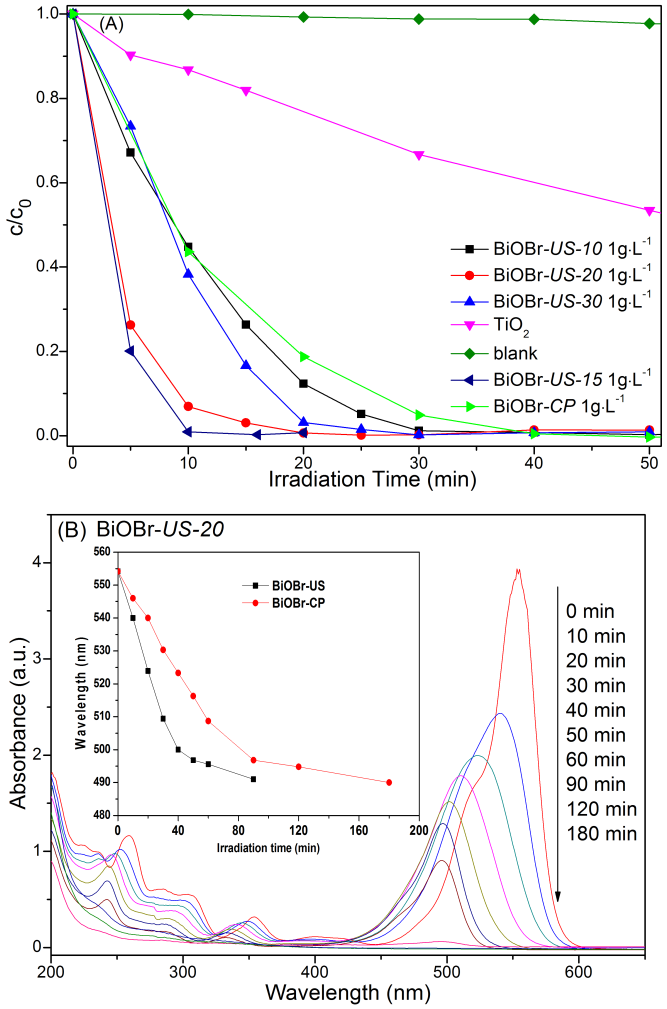


Figure 3.10: (A) Visible-light-driven photodegradation of Rh.B on various BiOBr samples and P-25 $TiO_2$ and without photocatalyst (1.0 g/L); (B) UV-Visible spectral changes of Rh.B as a function of photo-reaction time; and inset of (B) Wavelength shift as a function of the decrease in absorption maximum.

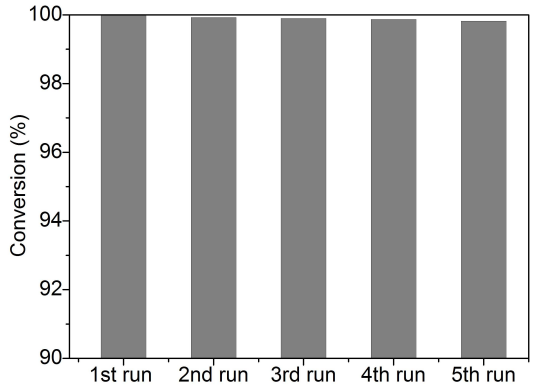


Figure 3.11: Cycling runs showing efficiencies of BiOBr$-US-15$ sample in the photodegradation of Rh.B

the photodegradation reaction. It has also been observed that all the BiOBr$-US-t$ samples are considerably more active than the corresponding BiOBr$-CP$ materials (Figure 3.10 A). From Figure 3.10 B it can be observed that the colour of the solution changed and vanished after 90 min and 180 min under photoreaction with the BiOBr$-US-15$ and BiOBr$-CP$ samples (0.5 g/L), respectively. A BiOBr$-US-15$ sample exhibited very similar photocatalytic activity in five cycling tests of Rh.B photodegradation under similar reaction conditions (Figure 3.11). The fresh and recycled BiOBr$-US-15$ retained the original PXRD data (Figure 3.1 A). Both the cycling photoreactions and the PXRD results suggest that BiOBr$-US-15$ with this new, flower-like hierarchical structure is a highly stable, visible-light-responsive photocatalyst both in structure and reactivity.

## 3.5 Conclusion

In summary, a sonification methodology for the rapid synthesis of intriguing flower-like BiOBr architectures in an aqueous medium has been developed without the necessity of organic solvents or templates. The flower-like BiOBr assembled photocatalysts possess both excellent photocatalytic activity and photo-stability in the visible-light-driven photodegradation of Rh.B, which is believed to derive from the attenuated light scattering and increased surface adsorption of the dye on the flower-like BiOBr hierarchical architectures. The sonochemical processes attendant upon ultrasound irradiation on the aged BiOBr nano-flakes and the detailed formation mechanism of the flower-like self-assembled morphology has also been proposed here. It is believed that this sonochemical procedure can be readily adapted and optimised to other important oriented layered materials for energy generation, storage and utilisation.

# Chapter 4

# AgBr-BiOBr p-n heterojunction

## 4.1 Overview

AgBr-BiOBr heterojunction photocatalysts with varying loadings of AgBr (the mass fraction is less than 5.0%) were synthesised through an effective co-precipitation method and used for the photodegradation of Rhodamine B under visible-light irradiation. Superior photocatalytic activities relative to that of pure BiOBr were observed on the AgBr-BiOBr catalysts with low AgBr loading (up to 0.5%). Higher AgBr loadings ($>0.5\%$) lead to isolated AgBr species and reduced photocatalytic activity. Among such catalysts, the AgBr (0.2%)-BiOBr sample exhibits the highest visible-light-responsive photoactivity, which can decolourise Rhodamine B within 30 min. However, these AgBr-BiOBr materials gradually lost their photoactivity in the cycling photocatalytic tests. Possible mechanisms for both the enhanced photocatalytic activity and deactivation of the AgBr-BiOBr heterojunctions were proposed on basis of theoretical speculation and experimental observations.

## 4.2 Introduction

Increasing concerns of fossil-fuel depletion and environment deterioration have stimulated great progresses in the potential photocatalytic utilisation of solar energy for both the environmental remediation and harvesting solar power.[34, 1] However, most of oxide semiconductor photocatalysts (i.e., $TiO_2$, $SnO_x$, ZnO, etc.) can mainly harvest UV light, which accounts for less than 5% of the total energy in solar spectrum.[54] Great efforts have been made in exploring new visible-light-responsive photocatalysts in order to utilise a larger portion of solar energy, particularly extending to the visible-light region, which accounts for more than 45% of the solar spectrum.[127] Bismuth oxybromide (BiOBr, see Figure 4.1, left), a simple p-type semiconductor, has emerged as a potential visible-light-responsive photocatalyst with excellent photocatalytic activity and stability. Unfortunately, its absorption of visible sunlight is limited by the relatively large electronic band gap ($E_g = 2.90\,\text{eV}$) of BiOBr.[122]

A variety of strategies, such as impurity doping,[128] surface decoration (metal deposition or heterojunction)[127, 129] and photo-sensitisation,[129] have been developed to modify the photocatalysts in order to improve their absorption to visible-light and photocatalytic performance. Among the modified photocatalysts, semiconductor heterojunctions, particularly p-n heterojunctions, offer great potential due to their tunable light absorption, low cost, and additional synergism between their closely contacted p-type and n-type semiconductor constituents.[38] In practice, an effective heterojunction should have the matched band structure, requisite band gap energy, suitable molar ratio and close contact interface between the hybrid semiconductors,[129, 130] which enable increased light absorption, efficient charge

separation, and accelerated transfer of photo-generated $e^- - h^+$ through the interfaces for subsequent photo-reactions.[131, 42]

So far, enhanced visible-light-responsive photocatalytic activity has been realised over BiOCl/$Bi_2O_3$[132] and AgI/BiOI[133] hybrid p-n heterojunction photocatalysts, in which the bismuth oxyhalide (BiOX, X = Cl, Br, I) semiconductors play key roles. Excellent visible-light-driven photocatalytic activity and stability were also observed over AgBr-based n-n typed heterojunctions, such as AgBr/$TiO_2$,[134] AgBr/ZnO,[135] and AgBr/$SiO_2$,[136] on which a significant amount of AgBr loaded on n-type UV-responsive semiconductors. However, the working mechanism currently remains uncertain since the high AgBr loading amount would hinder the identification of the key roles of the underlying heterojunctions. AgBr ($E_g = 2.69\,\text{eV}$)[137] has a smaller band gap and its anionic component might favour a close interface contact with BiOBr, which could allow AgBr and BiOBr to form a desirable AgBr-BiOBr p-n heterojunction. Therefore, it is reasonable to expect that a resulting AgBr-BiOBr p-n heterojunction would have enhanced absorption to visible light and thus improved photocatalytic performance compared to the individual component materials. Furthermore, considering that AgBr is itself a highly photosensitive material and BiOBr is of high photo-oxidation ability, we set out to investigate the photocatalytic performance and stability of the new AgBr-BiOBr heterojunctions and their working mechanism as visible-light-responsive photocatalysis.

Here, an effective yet simple co-precipitation method has been utilised to synthesise novel AgBr-BiOBr heterojunction photocatalysts and explore their performance in the photodegradation of a refractory organic dye, Rhodamine B (Rh.B, 20 mg/L in aqueous solution). Relatively low amount of AgBr loadings in the AgBr-BiOBr

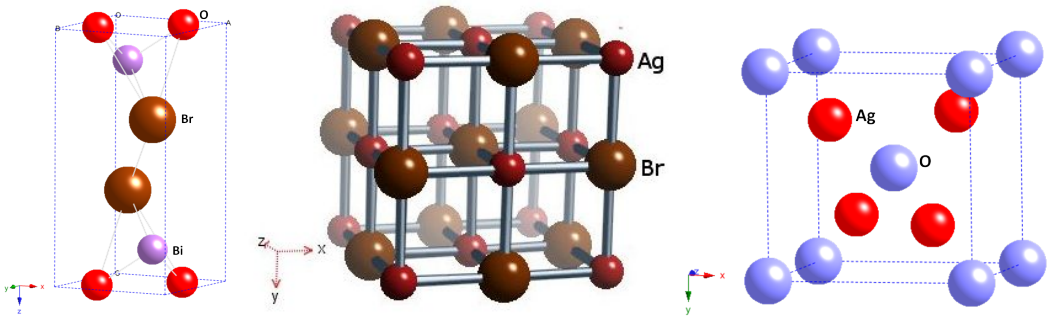


Figure 4.1: Illustration of primitive cell of BiOBr (left), AgBr (middle), and $Ag_2O$ (right)

heterojunctions were deliberately targeted in order to help clarify the key reactive species and photo-mechanisms in the photocatalysis process. A variety of characterisation techniques have been used to study the structure, morphology and optical property of the fabricated AgBr-BiOBr heterojunctions.

## 4.3 Experimental

### 4.3.1 Synthesis

AgBr-BiOBr samples were synthesised using a co-precipitation method under acid conditions. All reagents were purchased from Sigma Aldrich and used without further treatment. In a typical synthesis, 0.003 mol $Bi(NO_3)_3 \cdot 5\,H_2O$ (AR, 99.0%) was dissolved in aqueous solution of volume 30 mL containing 3 mL acetic acid (HAc). The solution was mixed with various amounts of $AgNO_3$ in order to obtain the AgBr-BiOBr composite with AgBr weight percentage of 0, 0.1, 0.2, 0.5, 1.0, 3.0 and 5.0. The $Bi(NO_3)_3 \cdot 5\,H_2O$ and $AgNO_3$ mixed solution was vigorously stirred for 30 min in the dark prior to adding to 30 mL de-ionised water containing stoichio-

metric amounts of KBr (AR, 99.0%). Light yellow precipitates were immediately observed upon mixing the solutions. After stirring for another 30 min at room temperature, the suspension was aged for 3 h. The resulting precipitate was filtered, washed thoroughly with distilled water, and then dried at 65 °C overnight.

### 4.3.2 Characterisation

The transition characteristics (direct or indirect) of the photocatalysts were analysed by processing the sharp absorption edge according to the equation:

$$\alpha \cdot h\nu = \mathrm{A} \cdot (h\nu - E_g)^{n/2}$$

where $\alpha$, $\nu$, $E_g$, and A are absorption coefficient, light frequency, band gap, and a constant, respectively. Among them, n is determined by the type of optical transition of a semiconductor.[138] Waters LCT premier with CTC-PAL autosampler and liquid chromatography mass spectroscopy (LC/MS) and Electrospray Ionization Mass Spectrometry (ESI-MS) were also used to determine the organic species in the supernatant solution and to identify the intermediates at different stages of photocatalytic reaction. The valence band (VB) edge potential of a semiconductor at the point of zero charge can be expressed empirically via Mulliken electronegativity theory:

$$E_{\mathrm{VB}} = \chi - E^e + \frac{1}{2}E_g$$

where $E_{\mathrm{VB}}$ is the VB edge potential, $\chi$ is the electronegativity of the semiconductor, which is the geometric mean of the electronegativity of the constituent atoms,

and the electronegativity of each atom is defined as the arithmetic mean of the atomic electron affinity ($A$) and the first ionisation energy ($I$). For instance, the electronegativity of BiOBr ($\chi_{\mathrm{BiOBr}}$) and $Ag_2O$ ($\chi_{\mathrm{Ag_2O}}$) can be calculated as follows:

$$\chi_{\mathrm{BiOBr}} = \sqrt[3]{(\chi_{\mathrm{Bi}} \cdot \chi_{\mathrm{O}} \cdot \chi_{\mathrm{Br}})}$$

$$\chi_{\mathrm{Ag_2O}} = \sqrt[3]{(\chi_{\mathrm{Ag}}^2 \cdot \chi_{\mathrm{O}})}$$

where the electronegativity of Br atom can be expressed as $\chi_{\mathrm{Bi}} = \frac{1}{2}(I_{\mathrm{Bi}} + A_{\mathrm{Bi}})$, $E^e$ is the energy of free electrons on the hydrogen scale ($\sim$4.5 eV), and $E_g$ is the band gap of the semiconductor. According to the equation: $E_{CB} = E_{VB} - E_g$, the conduction band edge could also be estimated by knowing the band gap energy of a semiconductor material.[50, 51, 52]

## 4.4 Results and discussions

### 4.4.1 Crystallinity of as-synthesised powders

The PXRD patterns of the AgBr-BiOBr samples with AgBr loading under 0.5% (Figure 4.2 A) showed only the characteristic Bragg diffractions of tetragonal BiOBr (JCPDS 73-2061, space group $P4/nmm$) (Figure 4.1).[81] This suggests the AgBr is either highly dispersed or under the detection limit of XRD. The lattice parameters of BiOBr in the AgBr-BiOBr heterojunctions with lower loading amount, as listed in Table 4.1, are in good agreement with those of pure BiOBr ($a$ = 3.923(5) Å,

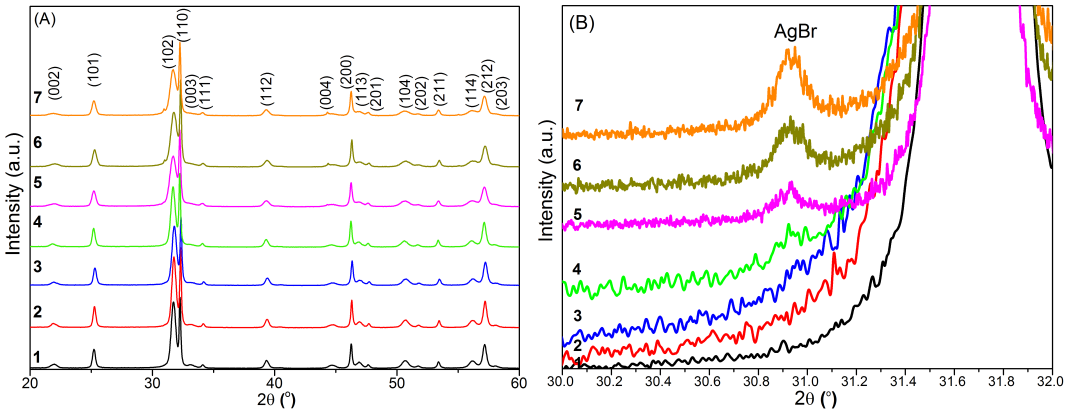


Figure 4.2: (A) XRD patterns of AgBr-BiOBr samples with different AgBr loadings: (1) 0.0%, (2) 0.1%, (3) 0.2%, (4) 0.5%, (5) 1.0%, (6) 3.0% and (7) 5.0% and (B) characteristic X-ray diffraction of AgBr around 31.0°

$c = 8.105(2)$ Å, $V = 124.74$ Å$^3$).[139] The unit cell volume and lattice parameter $a$ expanded insignificantly ($< 0.2\%$), and such extension could be ascribed to larger AgBr cell volume ($V = 192.55$ Å$^3$) compared to BiOBr.[140]

Amplified XRD patterns in the 30° to 32° region are presented in Figure 4.2 B. A Bragg peak at 30.9° appears adjacent to the (102) diffraction of BiOBr once AgBr loading exceeds 1.0%. This peak can be indexed to the most prominent Bragg peak ([002]) for cubic AgBr which increases intensity in as the AgBr loading increase (as shown in Figure 4.2 B). This correlation reveals the incorporated AgBr grows orientationally along the {102} plane of BiOBr. The crystallite size of the AgBr-BiOBr composite was calculated using Scherrer equation on (110) diffraction of BiOBr, as listed in Table 4.1. The crystallite size of BiOBr in the heterojunctions also significantly increased as the AgBr loading is increase up to 0.5%. The lattice parameters of BiOBr samples with AgBr loading equal to or greater than 1.0% are unchanged

Table 4.1: Lattice parameters, crystallite size, $E_g$, and photodegradation rate constants ($k_{RhB}$) of the as-synthesised AgBr-BiOBr samples

| Photocatalyst | Lattice parameters | | Crystallite size (nm) | $E_g$ (eV) | $k_{RhB}$ ($min^{-1}$) |
|---|---|---|---|---|---|
| | $a$ (Å) | $c$ (Å) | | | |
| BiOBr | 3.923(5) | 8.105(2) | 35.2 | 2.91 | 1.21 |
| AgBr(0.1%)-BiOBr | 3.926(1) | 8.110(3) | 40.1 | 2.88 | 1.26 |
| AgBr(0.2%)-BiOBr | 3.9259(10) | 8.113(3) | 58.3 | 2.88 | 1.58 |
| AgBr(0.5%)-BiOBr | 3.926(1) | 8.114(3) | 76.5 | 2.87 | 1.44 |
| AgBr(1.0%)-BiOBr | 3.9261(8) | 8.1098(21) | 52.6 | 2.86 | 0.863 |
| AgBr(3.0%)-BiOBr | 3.9259(10) | 8.110(2) | 74.7 | 2.82 | 0.943 |
| AgBr(5.0%)-BiOBr | 3.9261(8) | 8.111(2) | 61.6 | 2.80 | 0.810 |
| $TiO_2$ P-25 | - | - | - | 3.17 | 0.120 |

with respect to those with lower loadings (Table 4.1). It can be seen that the calculated crystallite sizes of BiOBr in all the AgBr-BiOBr heterojunctions are much larger than that of pure BiOBr. The slight variations in lattice parameters and crystallite sizes suggest AgBr was well dispersed in the AgBr-BiOBr samples at very low AgBr loading ($< 0.5\%$).

### 4.4.2 Morphology

Typical SEM images of as-prepared BiOBr and AgBr-BiOBr heterojunctions are shown in Figure 4.3. The samples obtained were flake-like powders with average diameter of approximately 300 nm and a thickness about 40 nm. Energy dispersive X-ray spectroscopy (EDS) performed on the series of samples revealed that all the Bi, Br and O elements coexist but that Ag can only be detected with AgBr loading greater than 1.0%. SEM images show that no significant morphological changes were induced by AgBr loading. TEM observations confirmed that no distinguished difference between the microstructure of BiOBr and heterojunctions were observed at AgBr loading below than 1.0%. Isolated AgBr particles can be observed for those

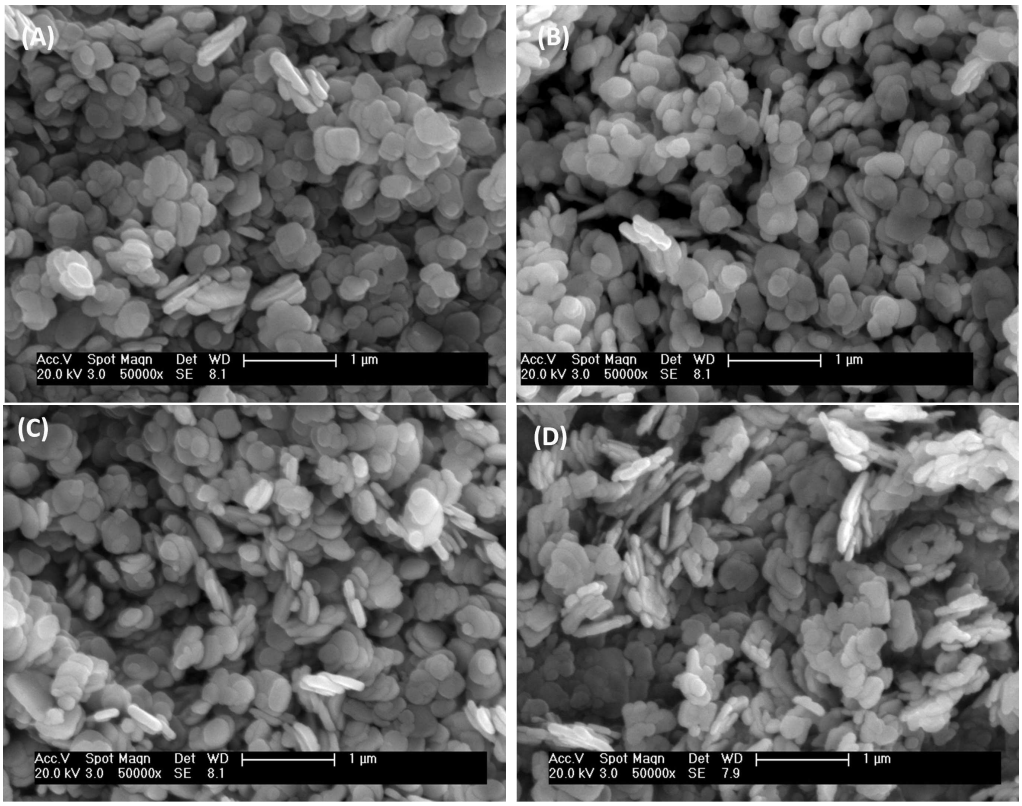


Figure 4.3: The FE-SEM images of AgBr-BiOBr samples with AgBr loading of: (A) 0.1 wt%, (B) 0.5 wt%, (C) 5.0 wt% and (D) pure BiOBr

samples of higher AgBr loading ($> 1.0\%$) (Figure 4.4).

TEM observations (Figure 4.4 A and B) of BiOBr and a typical heterojunction, AgBr(5.0%)-BiOBr, revealed that they have different microstructures. The pure BiOBr has smooth surface, but the surface of AgBr-BiOBr flake is well decorated with finite nano-particles with diameter around 5 nm to 10 nm. The d-spacing of the surface nano-particles (0.5 nm, as labeled in the insert of Figure 4.4 B) is consistent with the AgBr crystal structure. Electron energy loss spectroscopy (EELS) was used to detect the presence of Ag in the AgBr(5.0%)-BiOBr sample. Ag was detected in the region marked in Figure 4.4 B. No signal was detected from the nano-particles,

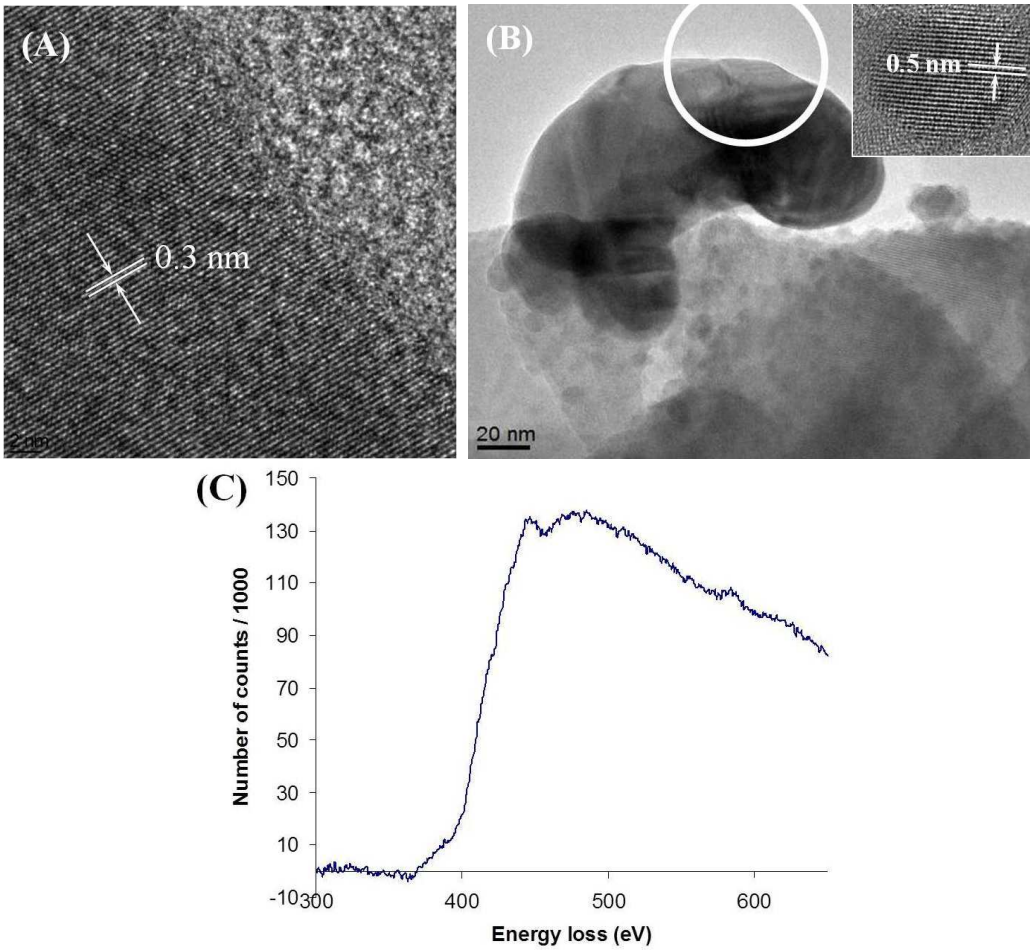


Figure 4.4: (A) TEM image of pure BiOBr, (B) a typical AgBr-BiOBr heterojunction, and (C) the EELS M edge of Ag taken from the region marked in B

which is potentially due to the size of the particles.

### 4.4.3 Surface elemental analysis

The surface composition of the AgBr-BiOBr samples were analysed using XPS (Figure 4.5). It is difficult to detect Ag as the loading of AgBr is less than 1.0%. How-

ever, AgBr may be verified indirectly through the changes of binding energy (B.E.) of Bi, O and Br in XPS because the elemental XPS is very sensitive to chemical environment.[141] Bi $4f$ XPS spectra are shown in Figure 4.5 A, where the two strong peaks centered at 163.9 eV and 158.6 eV are associated to core lines of Bi $4f_{5/2}$ and $4f_{7/2}$ in BiOBr. When the AgBr loading increased from 0% (pure BiOBr) to 5.0%, the Bi $4f_{5/2}$ and $4f_{7/2}$ peaks slightly blue shifted to 164.1 eV and 158.8 eV, respectively (Figure 4.5 A'). Correspondingly, as shown in Figure 4.5 B', the B.E. value of Br $3d$ photoelectron core line of AgBr(5.0%)-BiOBr, centering at 69.2 eV, is greater than that of BiOBr (69.0 eV, Figure 4.5 B). The B.E. values of Br $3d$ core line reveal that Br in the samples is $Br^{-1}$.[92] A similar shift was also observed in the O $1s$ spectra, as shown in Figure 4.5 C. The spectra could be fitted to two peaks at binding energy around 530.7 eV and 531.7 eV, respectively. The fitted peaks dominating around 530 eV can be attributed to bulk structural O species in BiOBr, while another peak around 532 eV could be attributed to the surface adsorbed components of hydroxyl group (-OH).[122] The lower intensity of such peak of AgBr-BiOBr than that of BiOBr arises from the surface coverage of AgBr, which partially covers the surface oxygen sites and thus lower XPS signals due to the reduced surface OH group. The B.E. shifts for Bi $4f$, Br $3d$ and O $1s$ in the AgBr(5.0%)-BiOBr sample were thought to arise from AgBr doping given the lower electronegativity of Ag ($\chi_{Ag} = 1.93$) than Bi ($\chi_{Bi} = 2.02$) which leads to stronger chemical binding of Ag-Br bond than Bi-Br.[88] The Ag $3d_{3/2}$ (373.3 eV) and $3d_{5/2}$ (367.3 eV) spectra of AgBr(5.0%)-BiOBr are presented in Figure 4.5 D, which are attributed to the $Ag^{+}$ in AgBr.[142] No $Ag^{0}$ signal was observed in the XPS spectra of these fresh heterojunction samples.

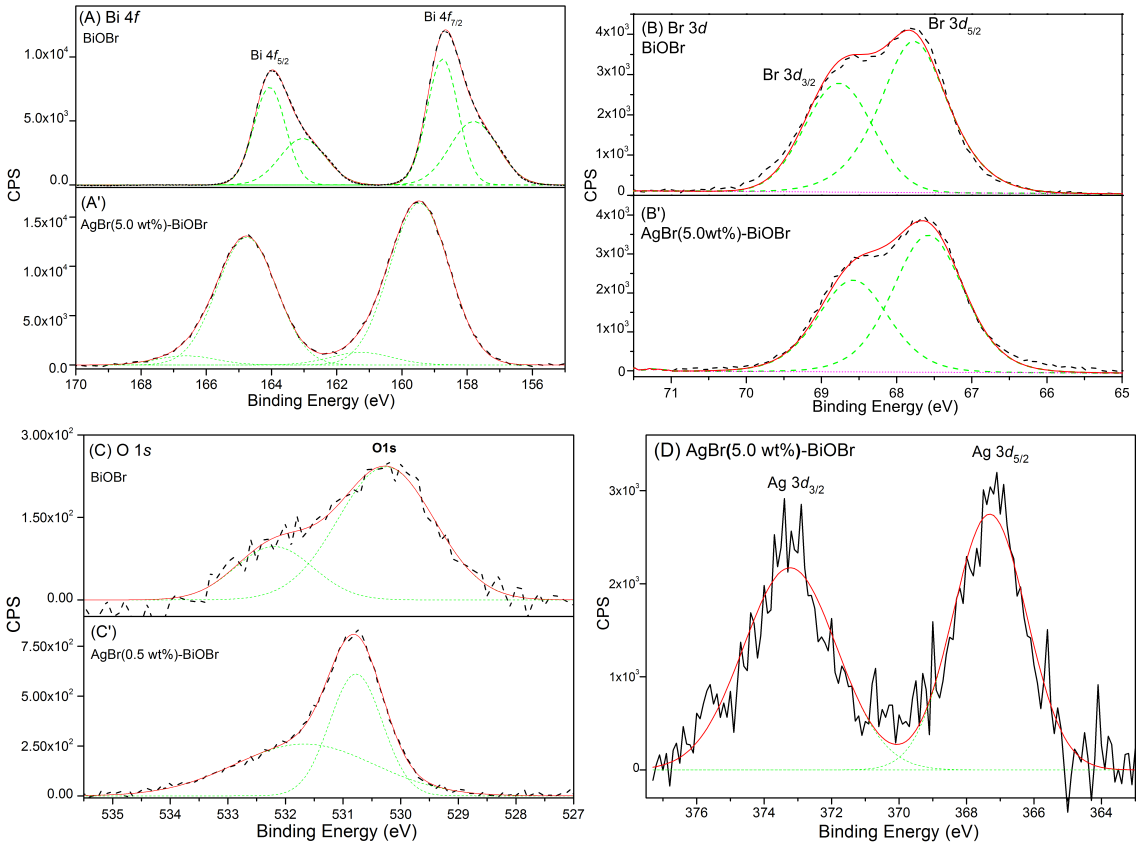


Figure 4.5: (A) Bi $4f$, (B) Br $3d$, (C) O $1s$, (D) Ag $3d$ XPS spectra of BiOBr and AgBr(5.0 wt%)-BiOBr sample

### 4.4.4 UV-Visible diffuse reflectance spectra of the AgBr-BiOBr

UV-Visible diffuse absorption or reflection spectra of a photocatalyst can reflect its ability to harvesting solar radiation and its band gap energy can be calculated from the corresponding spectrum. Figure 4.6 A shows the AgBr-BiOBr samples' UV-Visible diffuse reflectance spectra (UV-Visible DRS) transformed to show the absorption spectrum derived by the Kubelka-Munk theory. All the AgBr-BiOBr samples extend their light absorption edge to the visible-light region with respect to BiOBr. The addition of AgBr was shown to improve light absorption in the visible-light region, particularly in the 450 nm to 800 nm region. The results are consistent with the physical appearance of the pale yellow BiOBr and yellow AgBr-BiOBr powders. The corresponding band gap energy ($E_g$) values of AgBr and AgBr-BiOBr are approximately in the region of 2.60 eV to 2.82 eV dependent on AgBr loadings (Table 4.1), much smaller than that of $TiO_2$ ($E_g = 3.16$ eV). The sharp shapes of the reflectance spectra in the band gap region of the photocatalysts are characteristic of band gap transition. In addition, the charge transitions induced by bulky doping impurity levels, which produce characteristic tailed spectra.[138] It is worth noting that the absorption is not linearly varying to AgBr loadings. Their light absorption intensity in a broader region and the nonlinear change of absorption edges in the band gap region deviate the mechanistic spectrum superposition principle.[143, 144] A possible reason is that the UV-Visible DRS reveals surface absorption information, but only a small fraction of AgBr existing on the surfaces of the heterojunctions can be recorded in the UV-Visible DRS.

Figure 4.6 B and C show the transition plots of AgBr-BiOBr with 0.2% and 0.5% AgBr loadings, where the nonlinear plots of $(\alpha h\nu)^{n/2}$ *versus* $h\nu$ indicate that the

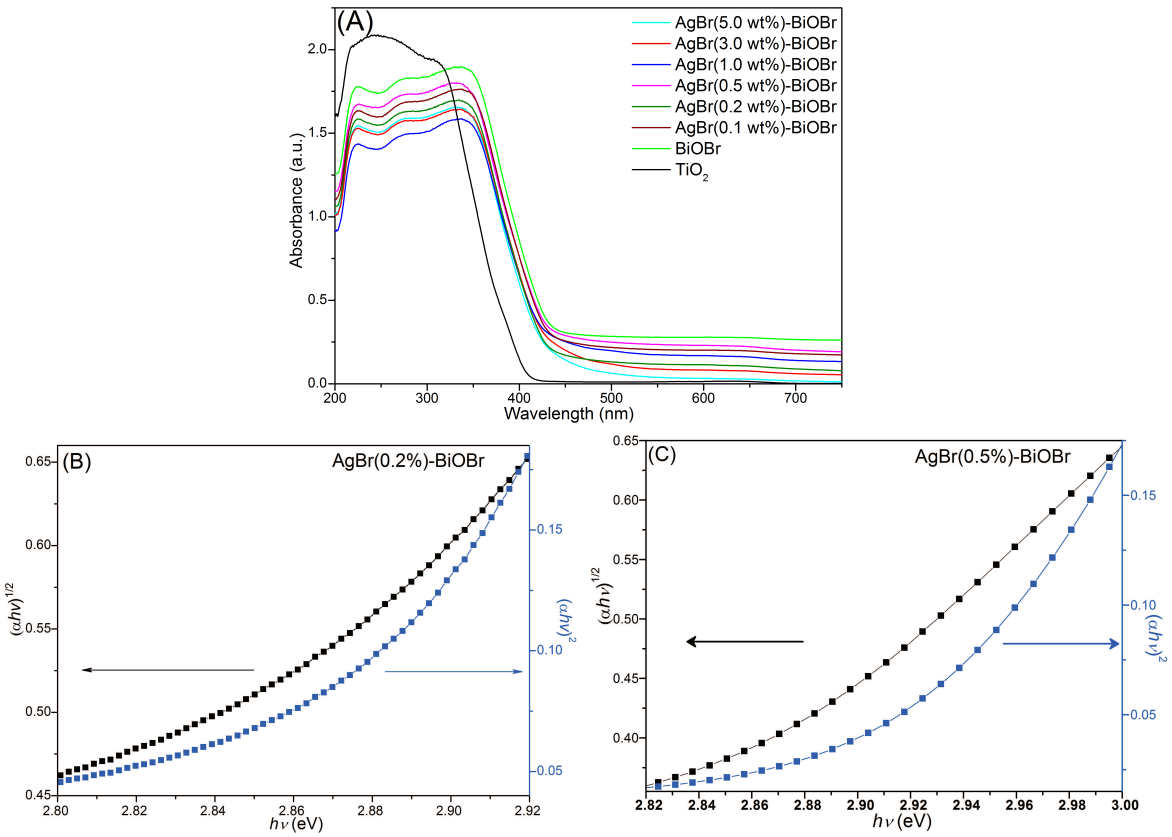


Figure 4.6: (A) UV-Visible diffuse reflectance spectra of BiOBr and AgBr-BiOBr samples, (B) the plots of $(\alpha h\nu)^{1/2}$ and $(\alpha h\nu)^2$ *versus* photo energy of AgBr(0.2%)-BiOBr sample and (C) AgBr(0.5%)-BiOBr

composite samples are not indirect or direct semiconductors.[74] The results suggest such AgBr-BiOBr heterojunctions have abnormal visible-light responses, and thus, the unusual photocatalytic activity could be expected from the heterojunctions under visible-light irradiation assuming the intimate contact interfaces generated.

### 4.4.5 Photocatalytic degradation of Rh.B and the photodegradation pathway

Rhodamine B, a chemically stable molecule with a characteristic absorption peak at 554 nm, was chosen as a probe molecule to assess reactivity of the photocatalysts. As shown in Figure 4.7 A, without catalyst the concentration of Rh.B remains unchanged even after 2 h of visible-light irradiation, while BiOBr and AgBr-BiOBr heterojunctions can decompose Rh.B completely in 50 min under the same reaction conditions. The apparent activity sequence of the catalysts are related to the AgBr loading, in the order as follows, AgBr(0.2%) > AgBr(0.5%) > AgBr(0.1%) > BiOBr > AgBr(3.0%) > AgBr(1.0%) > AgBr(5.0%) > $TiO_2$. The better activity of these BiOBr-based heterojunction than $TiO_2$ P-25 suggests they are active photocatalysts in cleaning up organic pollutant under visible-light irradiation. Less than 50% Rh.B may be decomposed over $TiO_2$ (Degussa P-25 aerosol) after 60 min of visible-light irradiation, which is assigned to the sensitisation effect of Rh.B to UV-responsive $TiO_2$.[81] The Rh.B photodegradation on each AgBr-BiOBr heterojunction follows the pseudo-first-order kinetics model, $\ln(C/C_0) = -kt$, where $C$ and $C_0$ are the concentration of the dye in solution at time $t$ and 0, respectively, and $k$ is the pseudo-first-order rate constant.[98] The rate constant, $k$, of Rh.B photodegradation were derived from the$-\ln(C/C_0) \sim t$ plots (Figure 4.7 B) and listed in Table 4.1.

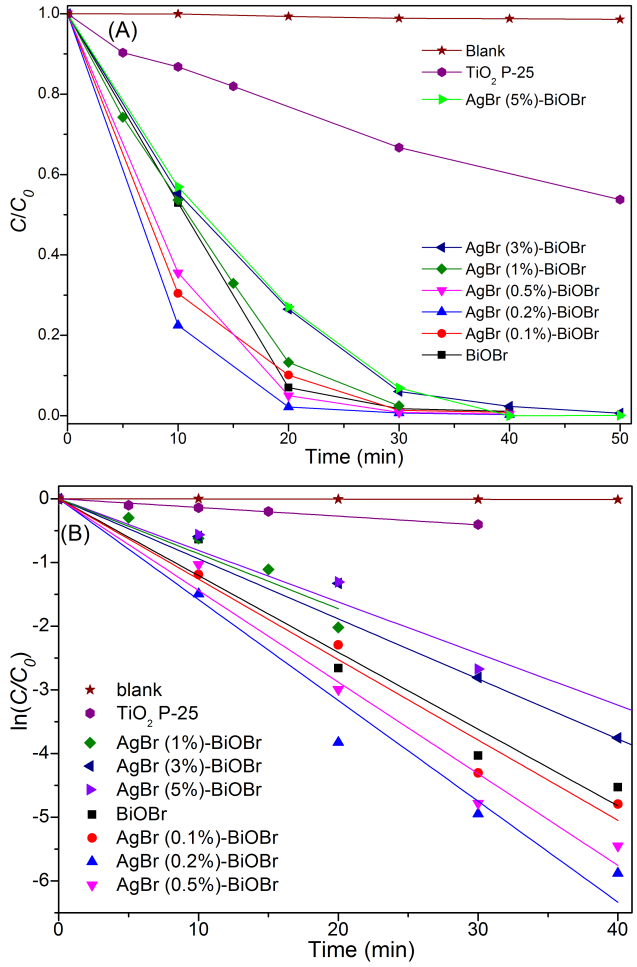


Figure 4.7: (A) Photodegradation of Rh.B over AgBr-BiOBr samples; and (B) plot of $\ln(C/C_0)$ versus irradiation time

Among such heterojunctions, AgBr(0.2%)-BiOBr exhibited the highest photocatalytic activity with nearly 80% Rh.B decomposed in the initial 10 min irradiation, while only 36% Rh.B degraded on AgBr(1.0%)-BiOBr. It is worth noting that the heterojunctions of low AgBr loadings are more active than pure BiOBr, though the activity of the heterojunctions with high AgBr loading decreased as AgBr isolated.

Considering the relationship of structure and optical properties of the heterojunctions with AgBr loading, the lower AgBr loading present better performance due to higher dispersion of AgBr on BiOBr which own closely contacted interface between AgBr and BiOBr.

Figure 4.8 A shows the variation of absorption spectra of Rh.B *versus* irradiation time on the AgBr(0.2%)-BiOBr, and the shift of maximum absorption wavelength as a function of irradiation time was inserted in Figure 4.8 A. It can be seen that the characteristic absorption band of Rh.B at 554 nm diminished quickly, accompanied by slight concomitant blue-shifts from 554 nm to 492 nm of the maximum absorption. This phenomenon can be interpreted by the incomplete mineralisation of Rh.B during the light irradiation as observed previously.[122]

The mineralisation extent of Rh.B dye was investigated through Total Organic Carbon (TOC) tests, which reveals the overall organic residuals in the aqueous solution. As shown in Figure 4.8 B, the TOC values significantly decrease to 80% on AgBr(0.2%)-BiOBr under 120 min light irradiation. The reduction of TOC is slower than the Rh.B decolourisation, suggesting that Rh.B is mineralised stepwise in the photocatalytic reaction.[129, 73] The gradual changes of TOC value inspired us to identify the residual organic species at different photocatalysis stage using Liquid Chromatography/Mass spectrometry (LC/MS). Figure 4.9 presents the mass spectra of the initial Rh.B solution and that after 40 min and 60 min photocatalytic reaction, respectively. The typical organic intermediate species were, therefore, able to be identified as listed in Table 4.2, which confirms that Rh.B was stepwise degraded

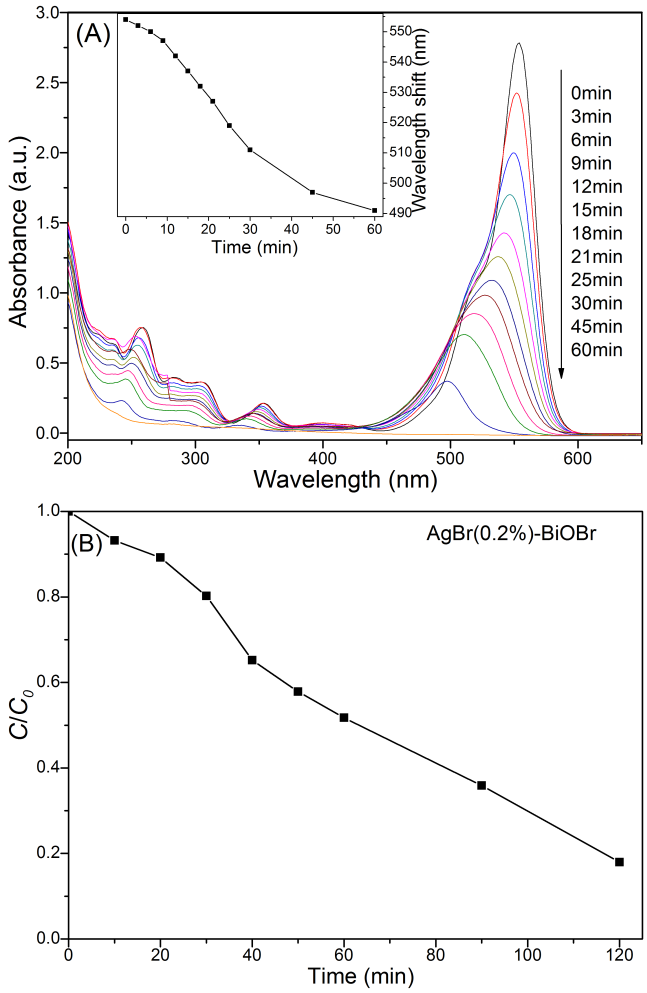


Figure 4.8: (A) UV-Visible spectral changes of Rh.B as a function of photoreaction time; inset: wavelength shifts as a function of the decrease in absorption maximum; and (B) the dependence of TOC on time for photodegradation of Rh.B on AgBr(0.2%)-BiOBr.

Table 4.2: Main intermediates from the degradation of Rh.B detected by MS

| Peak | m/z | Identified intermediates | Structural formula |
|---|---|---|---|
| a | 415 | N,N-diethyl-N'-ethyl rhodamine (DER) | 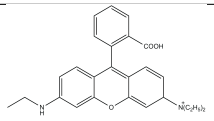 |
| b | 387 | N-ethyl-N'-ethyl rhodamine (EER) | 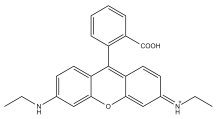 |
| b' | 387 | N,N-diethyl rhodamine (DR) | 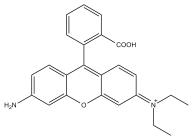 |
| c | 359 | N-ethyl rhodamine (ER) | 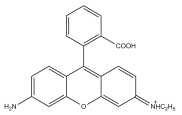 |
| d | 331 | Rhodamine (R) | 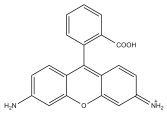 |
| e | 166 | Terephthalic acid | 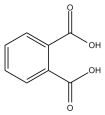 |
| e' | 166 | Phthalic acid | 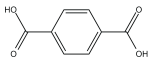 |
| f | 118 | Succinic acid | 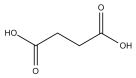 |

and mineralised on BiOBr and AgBr-BiOBr heterojunctions under visible-light irradiation.

Only Rh.B was observed in the solution prior to photocatalytic reaction, while N, N- diethyl- N'- ethylrhodamine (DER), N, N- diethylrhodamine (DR), N- ethyl- N'-

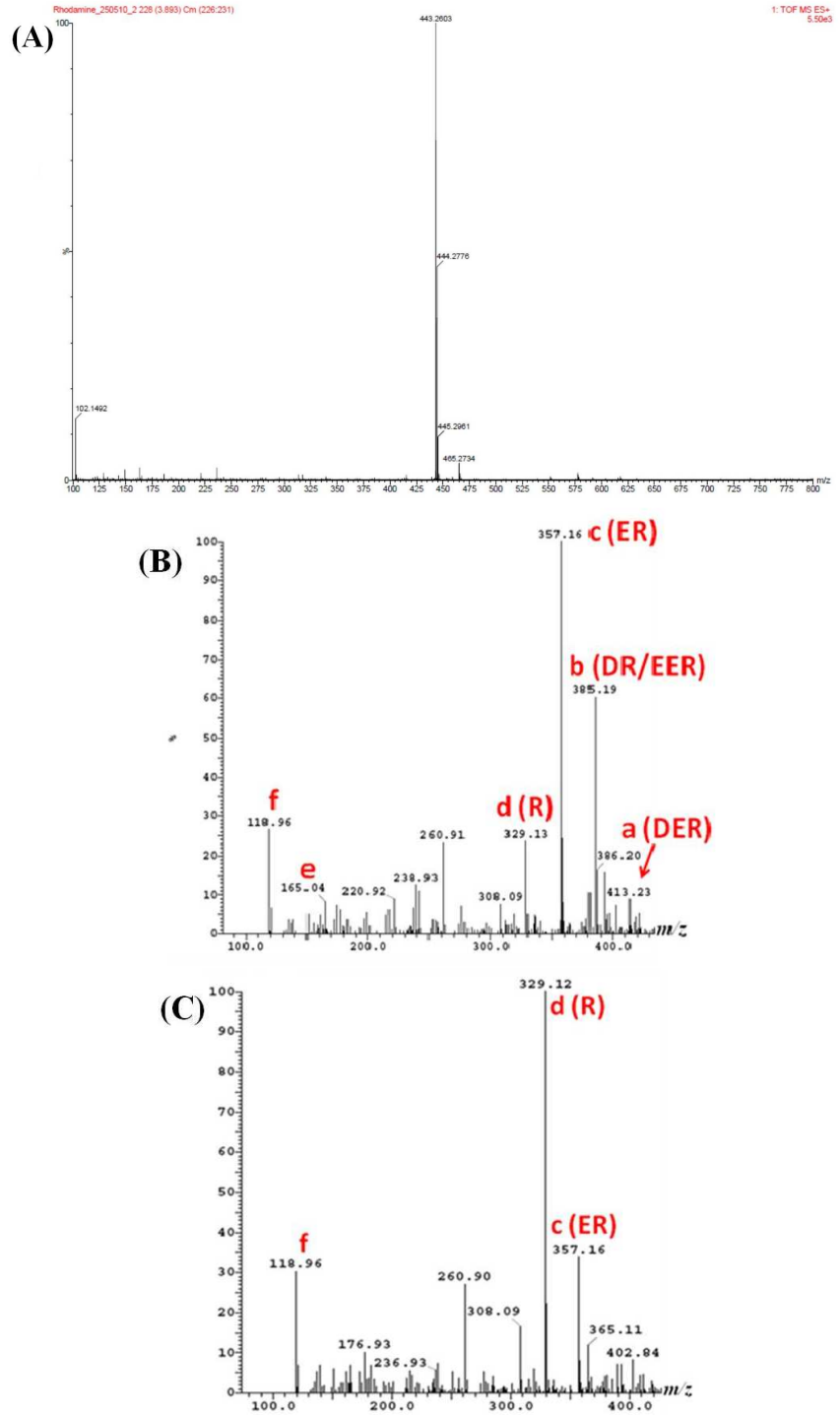


Figure 4.9: LC/MS spectra of Rh.B and its photodegradation products on AgBr-BiOBr at different irradiation time: (A) 0 min (Rh.B), (B) 40 minutes and (C) 60 minutes

ethylrhodamine (EER), N- ethylrhodamine (ER), and rhodamine (R) all appeared during a 40 min photoreaction.[78] The photodegradation process may therefore be described by an initial, rapid disappearance of Rh.B (Figure 4.8 A), accompanied with the increase of all four intermediates which subsequently decreased with further irradiation. These observations suggest the gradual and stepwise formation, transformation and decomposition of the reaction intermediates, which is in good agreement with the observations of the TOC analysis (Figure 4.8 B). The molecular-ion peaks of the intermediates differ exactly by 28 mass units in sequence (peak a-d), which is attributed to the sequential degradation of the N-ethyl groups from the maternal Rh.B molecule. The absence of $m/z$ 443 in Figure 4.9 B (after 40 min irradiation) indicates that Rh.B was completely transformed. Thus Rh.B photodegradation may be unambiguously described as a stepwise process in which N-de-ethylated decomposition is preferred.[78, 122] Some other organic acids such as succinic acid, phthalic acid and terephthalic acid *etc.*, were also observed by ESI-MS, and are listed in Table 4.2. These acids are mostly small molecular intermediates resulting from the cleavage of the xanthene ring in the maternal Rh.B and N-de-ethylated intermediates.[145] After 60 min irradiation all the refractory and coloured intermediates are almost fully decomposed, which corresponds to the decolourisation of the Rh.B solution, although the TOC value suggests this only accounts for half of the original Rh.B polluted solution (Figure 4.8 B).

### 4.4.6 Working mechanism of AgBr-BiOBr in Rh.B photodegradation

It is of great significance for the fundamental science and application of semiconductor heterojunctions to understand the photocatalytic working mechanisms of such AgBr-BiOBr photocatalysts. As a hybrid semiconductor, the photocatalytic activity of the p-n heterojunction relates directly to the electronic band structures of individual components, which determine the excitation, transportation, and ultimate fate of the photo-generated charge carriers.[34] Therefore, conduction and valence band positions (CB and VB) of AgBr-BiOBr heterojunctions are important factors in determining their reactivity for the decomposition of organic contaminants. The Mulliken Electronegativity principle was used to estimate the CB and VB positions of AgBr and BiOBr, and hence their photo-reactivity.[81] Despite the fact this methodology cannot give the discrete energy levels of individual semiconductors, it is acceptable for understanding the transportation of photo-generated charge carriers and is helpful to roughly judge the thermodynamic trends of photoreaction. Because of the complexity of the mechanistic energy principle, the charge carrier transportation mechanism based on energy bias law of heterojunctions has been widely accepted to simplify the depiction of photo-generated charge transportation.[146]

The calculated bottom of the conduction bands (CB) and top of the valence bands (VB) are listed in Table 4.3, and the schematic diagram of the band alignment of AgBr-BiOBr was drawn out and shown in Figure 4.10. BiOBr has more positive CB bottom and VB top than AgBr. The schematic band structure shows the band

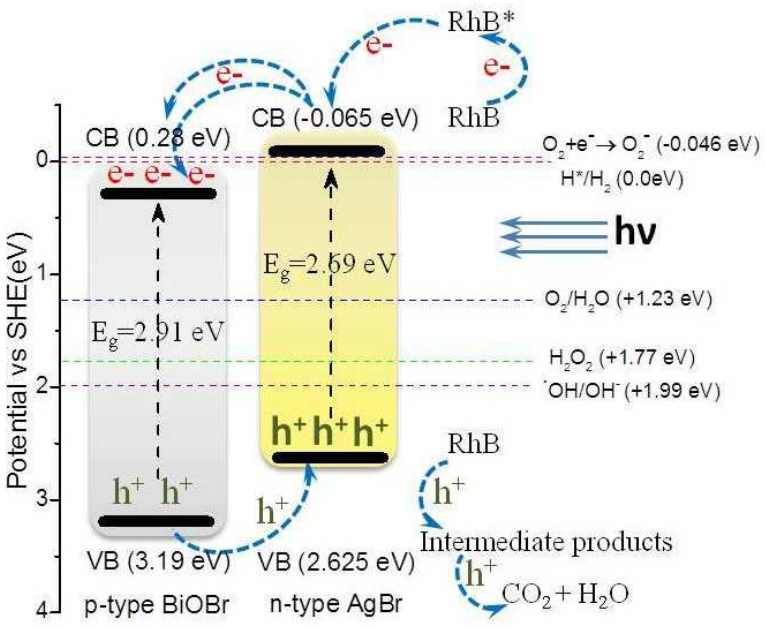


Figure 4.10: Schematic electronic band diagram of the AgBr-BiOBr system

potentials of p-type BiOBr and n-type AgBr fit the basic requirements to form a type II heterojunction of staggered band alignment, and thus, energy bias is naturally generated on the contact interfaces between the constituent AgBr and BiOBr. Such energy bias may facilitate the separation and subsequent transfer of photo-generated charge carriers.[146, 147] The intimate interface is expected because AgBr and BiOBr share the same $Br^-$ anion. The closely contacted interface was also observed in the TEM images of the AgBr-BiOBr heterojunctions (Figure 4.4). An intimate interface arising from sharing similar anion of individual semiconductor in heterojunction has also been reported in the $MoS_2$/CdS system by Can Li *et al.*.[147] The more dye adsorbed by AgBr(5.0%)-BiOBr than BiOBr but worse activity of the heterojunction reveals the surface adsorption is not the dominant factor determining their activity.

Table 4.3: Band energy position of AgBr and BiOBr (pH=1)

| Semiconductor | Electronegativity (eV) | Estimated $E_g$ (eV) | Calculated band position (eV) vs. NHE | |
|---|---|---|---|---|
| | | | VB | CB |
| AgBr | 5.780 | 2.69 | 2.625 | -0.065 |
| BiOBr | 6.238 | 2.91 | 3.193 | 0.283 |
| $Ag_2O$ | 5.298 | 1.30 | 1.448 | 0.148 |

As depicted in Figure 4.10, the photo-excited electrons ($e^-$) on $CB_{AgBr}$ preferentially flow down to the $CB_{BiOBr}$ crossing the interface, while the photo-generated positive carriers (holes, $h^+$) on $VB_{BiOBr}$ transfer to the $VB_{AgBr}$. Such transportation of the photo-generated carriers could either extend their transfer path or stabilise the photo-generated holes in the $VB_{BiOBr}$, leading to prolonged lifetime of the charge carriers and successfully hindering the unfavourable recombination of electron-hole ($e^- - h^+$) pairs. Besides the intrinsic photoexcitation of such p-n junction, the Rh.B may be excited by light irradiation (photo-activation) and the excited Rh.B* will inject electrons onto CB of either AgBr or BiOBr, and consequently Rh.B* relaxes back to Rh.B.

From the photoelectrochemistry point of view, the photo-generated holes on $VB_{AgBr}$ and $VB_{BiOBr}$ may oxidise organic dyes, while the electrons on the $CB_{AgBr}$ rather than $CB_{BiOBr}$ are able to reduce soluble $O_2$ to $O_2^-$, an oxidative species that can break down Rh.B. The $O_2 \cdot^-$ radicals maybe contribute to the heterojunctions' photoactivity but are unlikely to be the dominant factor because reduced reactivity was observed on the heterojunctions with higher AgBr loading ($> 1.0\%$) compared to AgBr-BiOBr with low AgBr loading. On the heterojunctions with lower AgBr loading, AgBr is highly dispersed and closely contacted with BiOBr which facilitates the transportation of charge carriers. Meanwhile, the holes on $VB_{BiOBr}$ are more

positive (more oxidative) than those on $VB_{AgBr}$, and hence such heterojunctions showed higher activity. The $VB_{BiOBr}$ and $VB_{AgBr}$ are more positive than the standard redox potentials of $\cdot OH/OH^-$ (1.99 eV) and $H_2O_2$ (1.77 eV), suggesting their photo-generated holes are far more oxidative than either $\cdot OH$ and $H_2O_2$.[51] In addition, the photo-generated hole cannot oxidise $OH^-$ to form $\cdot OH$ because of the more negative (reductive) potential of $Bi^V/Bi^{III}$ (1.59 eV). The reduction-oxidation (redox) half reaction $Bi^V/Bi^{III}$ would not happen since the BiOBr is much more stable both in air and solution.[81] Therefore, the photodegradation of Rh.B on the AgBr-BiOBr heterojunctions can be mainly associated with the photo-generated holes on the valance bands of AgBr and BiOBr.

Based on the discussions above, the mechanism of photocatalytic degradation of Rh.B on the AgBr-BiOBr heterojunctions can be proposed, and is described in the equations of (4.1 to 4.5). It is suppose that electrons are generated initially under visible-light irradiation, from the VB of the heterojunctions and photoexcited Rh.B dye, and subsequently flow up to the CBs of the heterojunctions. The CB electrons would react with soluble oxygen to form reactive $O_2^-$ radicals which either attack Rh.B or pass to the $CB_{BiOBr}$; correspondingly, the positively charged holes were left on VBs and the excited Rh.B (Rh.B*). The photocatalytic degradation reaction would subsequently take place, in which the Rh.B* would be transformed and decomposed into intermediate products and eventually converted to $CO_2$ and $H_2O$ by both the VB holes and $O_2^-$ radicals (Eqs. (4.6) and (4.7)). This mechanism is well supported by the decrease TOC and LC/MS results during the photocatalytic reaction.

1) Photo-excitation and photosensitised process of Rh.B

$$\mathrm{AgBr-BiOBr} \xrightarrow{h\nu} \mathrm{AgBr}(e^-_{CB} + h^+_{VB}) - \mathrm{BiOBr}(e^-_{CB} + h^+_{VB}) \tag{4.1}$$

$$\mathrm{RhB} \xrightarrow{h\nu} \mathrm{RhB}^* + e^- \tag{4.2}$$

$$e^-_{CB} + O_2 \rightarrow O_2^- \tag{4.3}$$

$$\mathrm{AgBr/BiOBr} + \mathrm{RhB}* \rightarrow \mathrm{RhB}^{+\cdot} + \mathrm{AgBr/BiOBr}(e^-_{CB}) \tag{4.4}$$

$$\mathrm{AgBr/BiOBr}(e^-_{CB}) + O_2 \rightarrow O_2^- + \mathrm{AgBr/BiOBr} \tag{4.5}$$

2) Simultaneous photocatalytic reaction

$$\mathrm{RhB}^{+\cdot} + O_2^- \rightarrow \text{intermediate products} \rightarrow CO_2 + H_2O \tag{4.6}$$

$$\mathrm{RhB} + h^+(\mathrm{AgBr-BiOBr}) \rightarrow \text{intermediate products} \rightarrow CO_2 + H_2O \tag{4.7}$$

### 4.4.7 Photocatalytic stability of the AgBr-BiOBr heterojunctions

It was reported that BiOBr, synthesised via either hydrothermal or co-precipitation, showed outstanding stability in photocatalysis.[81] The stability of the AgBr-BiOBr

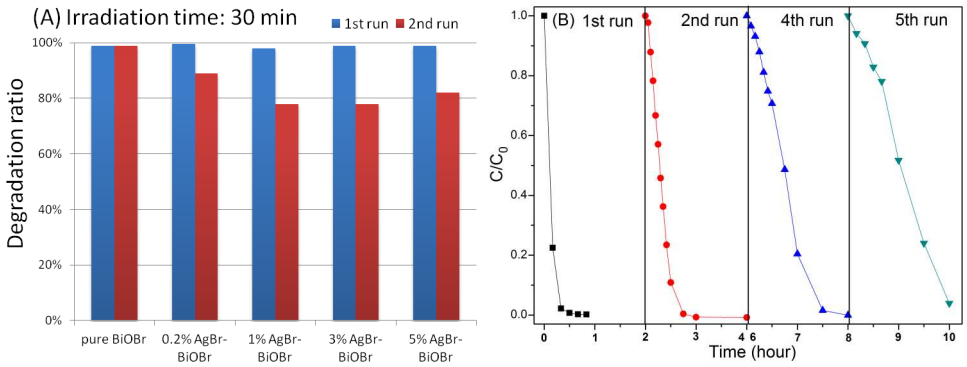


Figure 4.11: (A) Comparison of photoactivity on AgBr-BiOBr heterojunctions, and (B) cycling tests of Rhodamine B photodegradation on AgBr(0.2%)-BiOBr under visible-light irradiation

heterojunctions is a concern in photocatalysis due to the photosensitive AgBr involved. In order to investigate the stability of the photocatalysts, experiments of visible-light-driven photodegradation of Rh.B were repeated at different times on the recycled AgBr-BiOBr catalysts. After two cycling photocatalysis reactions, all the AgBr-BiOBr samples partially lost their activity (Figure 4.11 A), while the BiOBr retained its initial activity. AgBr(0.2%)-BiOBr showed better initial activity and stability than other AgBr-BiOBr heterojunctions, though it deactivated eventually and the deactivation was accelerated under prolonged visible-light irradiation (Figure 4.11 B). For example, AgBr(0.2%)-BiOBr completely decolourised Rh.B in 30 min in the first photocatalytic cycling test, but took nearly 120 min in the fifth cycling.

After each cycling test, the particulate AgBr-BiOBr photocatalysts were recovered and examined to investigate the evolution of the samples during the photocatalysis stability tests. The crystalline structure and surface composition of the recycled AgBr(0.2%)-BiOBr samples were characterised by XRD and XPS. As shown in the

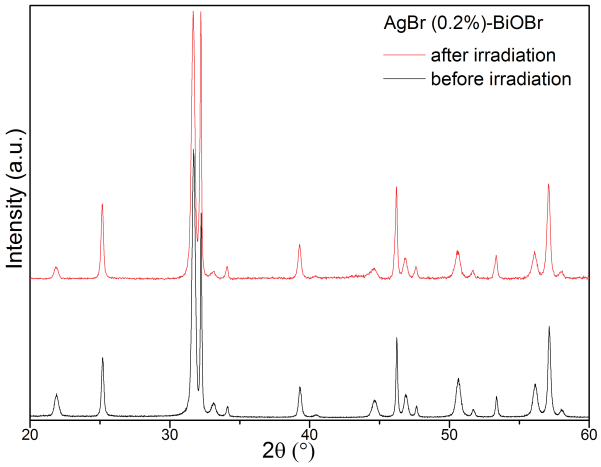


Figure 4.12: XRD patterns of the AgBr(0.2%)-BiOBr before and after irradiation

XRD pattern of the AgBr(0.2%)-BiOBr (Figure 4.12), there is no significant peak position or intensity change between the sample pre-/post-light irradiation after the $1^{st}$ run of visible-light irradiation, suggesting the low amount of AgBr on the surface of BiOBr stays relatively stable under short-term irradiation. As discussed in the XRD and XPS sections, low loading amount of AgBr cannot be identified by such X-ray analytic measurements. Nonetheless, the activity of the AgBr(0.2%)-BiOBr sample was greatly decreased in the long-term photocatalysis, which stimulated us to further study the transformation of AgBr-BiOBr with relatively high AgBr loading.

The AgBr(5.0%)-BiOBr was used to perform the cycling tests, and the diffraction patterns of the fresh and recycled AgBr(5.0%)-BiOBr are compared in Figure 4.13 A. Both the fresh and recycled heterojunction showed identical Bragg peaks for the BiOBr species, but new diffraction peaks centered at 38.1° were clearly observed on the recycled catalyst (Figure 4.13 B). The new diffraction peak can be well defined

to cubic $Ag_2O$ ($Pm\bar{3}m$, JCPDS 01-1041), a p-type oxide semiconductor with narrow band gap of 1.3 eV.[148] The diffraction intensity of the $Ag_2O$ became stronger with increased cycling times. For example, the XRD signal of $Ag_2O$ is stronger after fifth recycling than after the third cycling test. Correspondingly, the Bragg diffraction peak of AgBr was weak as the $Ag_2O$ signal intensified (Figure 4.13 C). These changes to the recycled AgBr(5.0%)-BiOBr suggest that the AgBr in the heterojunction was transformed into $Ag_2O$ along with the gradual deactivation of the heterojunction catalysts under long-term visible-light illumination.

The plausible formation process of $Ag_2O$ is depicted through photochemical reaction equations 8-11. During the photocatalysis process, trace amounts of $Ag^+$ and $Br^-$ would be generated via ionising AgBr in the heterojunction (Eq. 4.8), under the light irradiation. The $Ag^+$ will then react with $OH^-$ to generate AgOH, which spontaneously convert to $Ag_2O$ (Eq. 4.9). The overall reaction is summerised as equation 4.10, revealing that AgBr is gradually transformed into $Ag_2O$ and replaces AgBr in the active site during photocatalytic reaction. These changes may be accelerated by light irradiation, as a consequence of the photocatalyst deactivation.

$$H_2O \rightleftharpoons H^+ + OH^- \tag{4.8}$$

$$AgBr + H_2O \xrightarrow{h\nu} Ag^+ + Br^- + H^+_{aq} + OH^-_{aq} \tag{4.9}$$

$$2Ag^+ + 2OH^- \rightarrow 2AgOH \rightarrow Ag_2O + H_2O \tag{4.10}$$

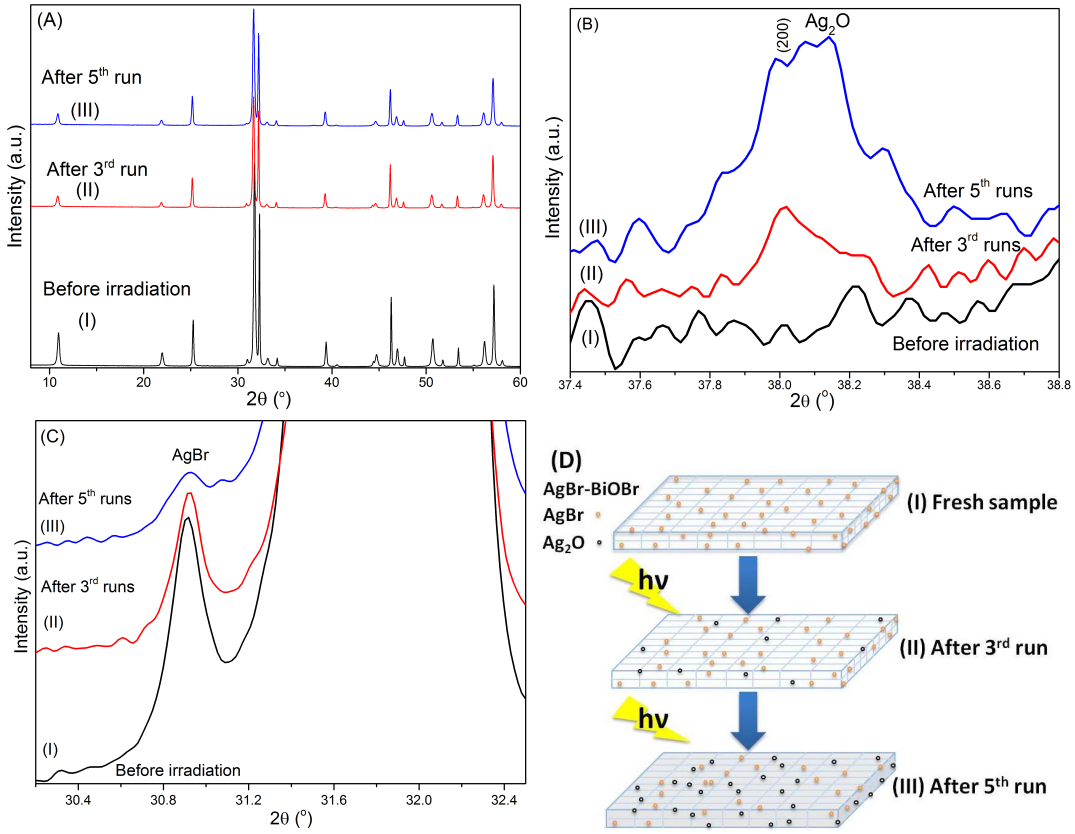


Figure 4.13: (A) XRD patterns of the fresh and recycled AgBr(5.0%)-BiOBr samples; (B, C) the characteristic XRD peaks of $Ag_2O$ at $38.1^o$ and AgBr at $31.0^o$ after cycling tests; and (D) schematic evolution of AgBr-BiOBr sample under long-term irradiation

Table 4.4: Ratio of AgBr, $Ag_2O$ and BiOBr characteristic diffraction peak intensity of AgBr(5.0%)-BiOBr *versus* repeat time

| | $\frac{I_{AgBr}}{I_{BiOBr}}$ (%) | $\frac{I_{Ag_2O}}{I_{BiOBr}}$ (%) |
|---|---|---|
| Before | 5.27 | 0 |
| After 3$^{rd}$ test | 3.28 | 0.189 |
| After 5$^{th}$ test | 1.98 | 0.408 |

Note: the characteristic peak (110) of BiOBr was chosen as the reference peak to compare the relative peak intensity.

In total:

$$2AgBr + H_2O \xrightarrow{h\nu} Ag_2O + 2\,H^+ + 2\,Br^- \tag{4.11}$$

### 4.4.8 Deactivation mechanism of AgBr-BiOBr photocatalysts

On the basis of the photo-degradation mechanism and stability study, the deactivation mechanism of our AgBr-BiOBr samples can now be proposed. As schematically illustrated in Figure 4.13 D, a small amount of AgBr was transformed into $Ag_2O$ on the surface of BiOBr once the AgBr-BiOBr sample was irradiated with visible-light for a certain period (Figure 4.13 D, scheme I-III). The $Ag_2O$ concentration gradually increased after long-term irradiation (Figure 4.13 D, scheme II). The XRD intensity of $Ag_2O$ monotonically increased as observed in AgBr-BiOBr, revealing more $Ag_2O$ species were generated, during the multiple recycling photocatalytic tests (Figure 4.13 B). Eventually, the $Ag_2O$ would mask the active AgBr sites in the heterojunction, resulting in the formation of $Ag_2O$-AgBr-BiOBr, a p-n-p type hetero-structure, with reduced photoactivity (Figure 4.13 D, scheme III).

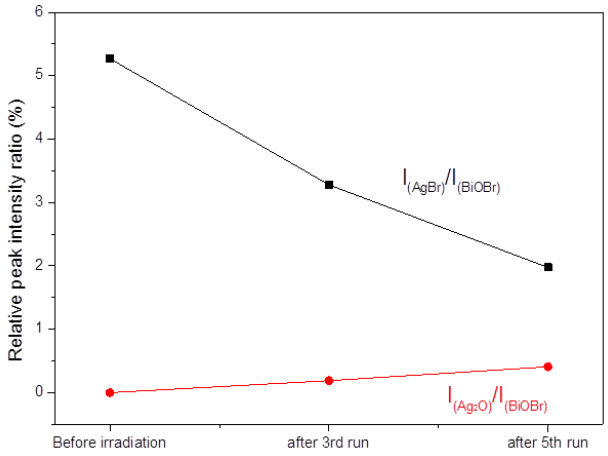


Figure 4.14: Relative XRD peak intensity ratio of AgBr-BiOBr and $Ag_2O$-AgBr-BiOBr of AgBr(5.0%)-BiOBr *versus* repeat time

The decreasing concentration of AgBr and the correspondingly increase of concentration of $Ag_2O$ in the AgBr-BiOBr heterojunction with highest amount of AgBr was further investigated as shown in Figure 4.14. The as-calculated relative peak intensity ratio of AgBr to BiOBr was found to correlate with the stoichiometry of the heterojunction system (Table 4.4). Linear trends in peak intensity for AgBr and $Ag_2O$ could be clearly observed in Figure 4.14, which confirms that deactivation of AgBr is a stepwise accelerated process.

The $Ag_2O$-induced deactivation can be well explained from the photoelectrochemistry point of view as illustrated in Figure 4.15. The estimated top of the $VB_{Ag_2O}$ is located at more negative potentials than $H_2O_2$, ·OH and VBs of BiOBr and AgBr. This suggests $VB_{Ag_2O}$ is a weaker photo-oxidant with limited oxidising ability for Rh.B decomposition. On the other hand, the $CB_{Ag_2O}$ potential is more positive than those of AgBr and $O_2^-$ but more negative than the $CB_{BiOBr}$, suggesting the electrons on the $CB_{AgBr}$ preferentially hop onto CB of $Ag_2O$, which competes with the elec-

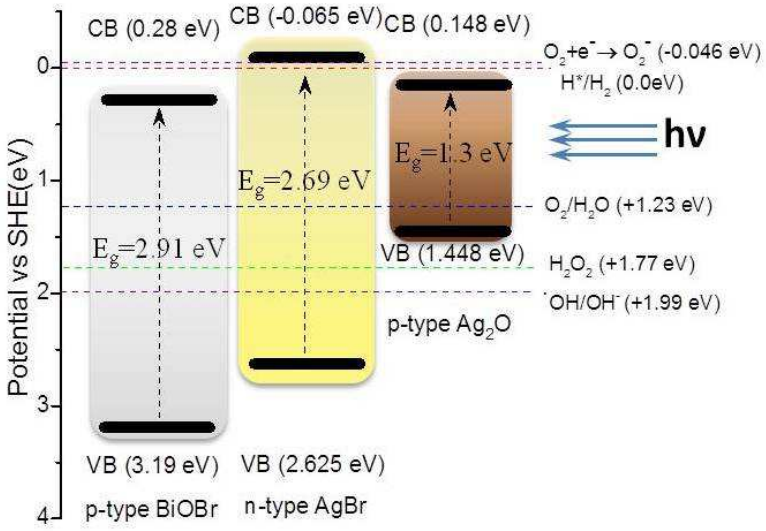


Figure 4.15: Schematic band alignments of the deactivated AgBr-BiOBr

trons flowing onto $CB_{BiOBr}$ and production of reactive $O_2^-$. The $in-situ$ generated $Ag_2O$ also leads to deterioration of the intimate interfaces between AgBr and BiOBr of the p-n heterojunction. $Ag_2O$ absorbs more light due to its smaller band gap energy and thus mask the active AgBr sites. Moreover, the narrow band gap of $Ag_2O$, and thus short electron migration pathway, would inevitably lead to faster recombination of photo-generated charge carriers. Because the BiOBr in the heterojunction remains almost unchanged, the photo-generated $Ag_2O$ species should be the dominant factor responsible for the deactivation of the AgBr-BiOBr heterojunctions. In general, despite the fact that the crystal structure of BiOBr in the AgBr-BiOBr heterojunctions remains stable, the transformation of AgBr to $Ag_2O$ would occur during photocatalytic reaction.[129] The $Ag_2O$ particles formed as stronger recombination centers and would destroy the synergistic interaction between AgBr and BiOBr in photocatalytic reaction, and thus reduced the surface reactivity arisen from AgBr.

It is worth of noting that the results are significantly different from the previous reports for Ag/AgBr/BiOBr,[149] AgBr/$TiO_2$[134] and AgI/BiOI[133] systems, where the authors did not observe transformations of either AgBr or AgI. The authors prepared Ag/AgBr/BiOBr samples by photo-reduction of AgBr/BiOBr using methanol as hole scavenger (reducing reagent) in the preparation process.[149] The redox power of the AgBr/$TiO_2$ system mainly arose from the photo-generated charges from AgBr under visible-light irradiation, where AgBr serves as a sensitiser to $TiO_2$, which may feedback the photo-generated charges to stabilise AgBr.[134] The fate of the AgI was not reported in the AgI/BiOI systems.[133] In this case, the AgBr/BiOBr samples were synthesised and used in the aqueous solution (with of plenty of $OH^-$ anions) without any reductive solvent involved. The photo-generated hole on the $VB_{BiOBr}$ has stronger oxidation potential than that in BiOI and $TiO_2$, and the valence band position of BiOBr is much deeper than AgBr, which might accelerate the corrosion of AgBr during the long-term photocatalytic reaction.

## 4.5 Conclusion

AgBr-BiOBr heterojunctions with different AgBr loading amounts, 0% to 5.0% AgBr, were prepared using an acidic co-precipitation method and used for photodegradation of Rh.B under visible-light irradiation. The properties of the obtained materials were characterised using XRD, SEM, UV-Visible spectroscopy and XPS.

AgBr may be well dispersed in the heterojunctions at low loading levels, while isolated AgBr species may be observed apart from BiOBr phase once the AgBr load-

ing exceeds 1.0%. Loading AgBr did not significantly affect the flake morphology of the BiOBr-based heterojunctions but improve visible-light harvesting in comparison with BiOBr.

Under visible-light irradiation, the initial activity of Rh.B photodegradation on the AgBr-BiOBr heterojunctions is closely related to the AgBr loading. The AgBr(0.2%)-BiOBr photocatalyst showed the best initial activity and stability among these AgBr-BiOBr heterojunctions. The enhanced photocatalytic activity is mainly attributed to the band structure and the additional synergistic effect within the p-n junctions. Loading of AgBr greater than 1.0% leads to the formation of larger AgBr particles and weaker catalytic activity because the majority of AgBr is not in close contact with the BiOBr and may actively screen light irradiation.

All the AgBr-BiOBr heterojunctions are prone to deactivation in the photocatalytic reactions since the AgBr is vulnerable and transformed to $Ag_2O$ under light irradiation. The as-formed $Ag_2O$ reduces the intimate interface of AgBr-BiOBr catalysts, masks the light excitation, and serves as recombination center of photogenerated charge carriers, resulting in the deactivation of the catalysts.

# Chapter 5

# BiOBr-$ZnFe_2O_4$ p-n heterojunction

## 5.1 Overview

In Chapter 4, AgBr-BiOBr p-n heterojunctions were prepared and the properties, performance and working mechanism were also discussed based on key characterisation techniques. However, this heterojuncted semiconductor material tends to deactivate under long-term irradiation. A considerably more durable n-type semiconductor material is in need for designing a more stable BiOBr-based p-n heterojunction. In this chapter, a class of p-n heterostructures comprising of n-type $ZnFe_2O_4$ and p-type BiOBr photocatalysts with visible-light response have been prepared utilising a simple ultrasound-assisted, precipitation-deposition method. The heterojunctions with suitable BiOBr/$ZnFe_2O_4$ ratios have a fascinating micro-spherical morphology and exhibit excellent photocatalytic activity in visible-light-driven degradation of Rhodamine B. The property and photocatalytic performance of the heterojunctions will also be discussed in this chapter.

## 5.2 Introduction

As mentioned previously, p-type semiconductor BiOBr has high photocatalytic activity and stability under UV and visible-light irradiation.[1, 113, 15, 81, 150, 151] The intrinsic lamellar structure and indirect band gap of BiOBr endows it with excellent mobility and a prolonged transfer path for photo-generated electrons and holes, therefore simulated intensive interest in the application of solar energy conversion.[152] However, the band gap energy ($E_g$) of BiOBr is around 2.9 eV, indicating that it cannot absorb the region of the visible-light spectrum above 430 nm.[132]

So far, impurity doping has been the most frequently used method to extend the optical absorption edge of wide band gap semiconductors since the development of nitrogen-doped $TiO_2$ (N-$TiO_2$).[1, 128, 35, 153] Doping is considered as an efficient method only if a good combination of hosts and dopants are chosen. Indeed, the doping of BiOBr with I or Pb may narrow the band gap of BiOBr significantly.[151, 127] Nevertheless, the activity of doped photocatalysts is usually sensitive to both the doping level and homogeneity;[150] in some cases, the dopant works as a recombination centre between photo-generated electrons and holes.

In contrast, combining two semiconductors with different band gaps to form heterojunctions, for example, BiOCl/$Bi_2O_3$ and AgI/BiOI, provides more flexibility than doping, with respects to broadening visible-light absorption and improving tolerance to component heterogeneity.[132, 133] This is because the heterojunction has great potential in tuning the desired electronic properties of the composite photocatalysts, leads to the protracted lifetime of photo-generated charge carriers.[132] Though AgX (X=Cl, Br, I) are frequently used in building heterojunctions with suitable semiconductors, they usually suffer from significant deactivation under op-

erating conditions due to their light-sensitive property. The stability of the junction system still needs to be improved, which leads us to explore a more stable p-n heterostructure.[132, 133, 154]

Zinc ferrite ($ZnFe_2O_4$) is a spinel-type ($AB_2O_4$) semiconductor with typical $E_g$ about 1.9 eV, which enables it to absorb sunlight up to 653 nm or even larger.[155] Despite the fact that $ZnFe_2O_4$ itself has very little activity due to the rapid recombination of light-excited charges, it shows good stability in photo-degradation of organic pollutants.[156] Enhanced visible-light-driven photo-activity has been observed over some composite semiconductors which combine $ZnFe_2O_4$ with secondary semiconductor, such as $TiO_2$ or ZnO, of large $E_g$.[150] These results provided the motivation to fabricate BiOBr-$ZnFe_2O_4$ heterojunctions with the hope of enhanced catalytic performance.

## 5.3 Experimental

### 5.3.1 Synthesis of BiOBr-$ZnFe_2O_4$ heterojunctions

All the chemical reagents and solvents for synthesis and analysis are commercially available and used without further treatment. Zinc ferrite was synthesised by co-precipitation method, and its precursors, zinc acetate (AR, 96.0%) and iron(III) nitrate nonahydrate (97.0%) were purchased from BDH and Sigma-Aldrich, respectively. The precursor of bismuth oxybromide, bismuth nitrate ($Bi(NO_3)_3 \cdot 5\,H_2O$, AR, 99.0%) and KBr (AR, 98.0%) were purchased from Sigma-Aldrich and BDH, respectively.

#### 5.3.1.1 Synthesis of Zinc Ferrite ($ZnFe_2O_4$)

The $ZnFe_2O_4$ precursors were synthesised by the co-precipitation method, in a typical experiment, stoichiometric amounts of $Zn(CH_3COO)_2 \cdot 2\,H_2O$ and $Fe(NO_3)_3 \cdot 9\,H_2O$ were completely dissolved in 200 mL distilled water under magnetic stirred for 20 min. Then 2 mol/L $NaOH/Na_2CO_3$ buffer solution was dropped into the solution to adjust the pH values ranging between 9 and 10. During the reaction the colour of the solution changes from transparent to yellow and then to black. After fiercely stirring for another 30 min, the solution was aged for 6 h and the resulting precipitate was filtered and washed by ethanol and distilled water. Final products were obtained after drying in the oven overnight at the temperature of 65 °C. The as-synthesised product with a dark brown colour was calcined at 800 °C for 6 h to form the spinel structure.

#### 5.3.1.2 Synthesis of the BiOBr-$ZnFe_2O_4$ heterojunctions

A precipitation-deposition method has been utilised to obtain the BiOBr-$ZnFe_2O_4$ heterojunction with different molar ratios. In a typical synthesis, a measured amount of $Bi(NO_3)_3 \cdot 5\,H_2O$ and $ZnFe_2O_4$ were dissolved in 100 mL aqueous solution containing 5 mL acetic acid (HAc). The solution was mixed with various amount of $Bi(NO_3)_3 \cdot 5\,H_2O$ in order to obtain BiOBr-$ZnFe_2O_4$ with molar ratio of 1:9, 3:7, 5:5, 7:3, 9:1, respectively. The mixture was vigorously stirred for 30 min at room temperature, and the resulting solution was added rapidly to 30 mL of distilled water containing stoichiometric amount of KBr. Upon the addition of mixed solution, light purple precipitates were immediately observed. After stirring for another 30 min at room temperature, the suspension was aged for 3 h; the resulting precipitate was

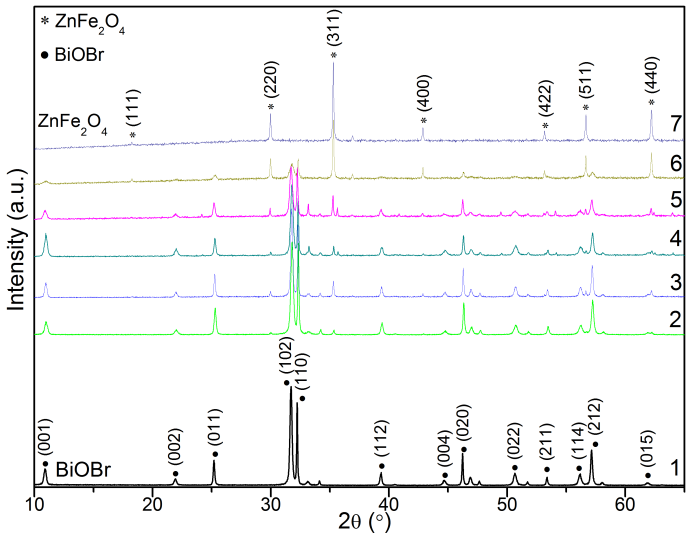


Figure 5.1: XRD patterns of as-synthesised BiOBr-$ZnFe_2O_4$ samples (1. BiOBr; 2. 0.9BiOBr-0.1$ZnFe_2O_4$; 3. 0.7BiOBr-0.3$ZnFe_2O_4$; 4. 0.5BiOBr-0.5$ZnFe_2O_4$; 5. 0.3BiOBr-0.7$ZnFe_2O_4$; 6. 0.1BiOBr-0.9$ZnFe_2O_4$ and 7. $ZnFe_2O_4$ )

filtered, washed thoroughly with distilled water, and then dried at 65 °C overnight.

## 5.4 Results and discussions

### 5.4.1 Crystal structure

The PXRD patterns (Figure 5.1) of the as-synthesised samples can be indexed to $Fd\bar{3}m$ cubic $ZnFe_2O_4$ (JCPDS 21-874)[157] and $P4/nmm$ tetragonal BiOBr (JCPDS 73-2061)[139] crystal phases, respectively. The narrow and sharp Bragg diffraction peaks of each component reveal that BiOBr and $ZnFe_2O_4$ in the samples are highly crystalline.[157] No other phases can be found in the BiOBr-$ZnFe_2O_4$ heterojunctions, suggesting that no impurity species were formed between BiOBr and

Table 5.1: The average crystallite size, band gap energy ($E_g$) and photo-degradation rate constants ($k_{Rh.B}$) of BiOBr-$ZnFe_2O_4$ composites photocatalysts

| Photocatalyst | Crystallite Size (nm) | $E_g$ (eV) | $k_{Rh.B}$ ($min^{-1}$) |
|---|---|---|---|
| BiOBr | 107.3 | 2.88 | 0.066 |
| 0.9BiOBr-0.1$ZnFe_2O_4$ | 75.1 | 2.13 | 0.17 |
| 0.7BiOBr-0.3$ZnFe_2O_4$ | 34.6 | 2.01 | 0.074 |
| 0.5BiOBr-0.5$ZnFe_2O_4$ | 27.9 | 2.25 | 0.14 |
| 0.3BiOBr-0.7$ZnFe_2O_4$ | 32.8 | 1.84 | 0.085 |
| 0.1BiOBr-0.9$ZnFe_2O_4$ | 37.6 | 1.71 | 0.019 |
| Mechanically mixed 0.9BiOBr-0.1$ZnFe_2O_4$ | - | - | 0.092 |
| $ZnFe_2O_4$ | 83.4 | 1.67 | 0.002 |
| $TiO_2$ | - | 3.20 | 0.013 |

$ZnFe_2O_4$.[132] However, the average crystallite sizes of BiOBr in the heterojunctions are much smaller than that of pure BiOBr as shown in Table 5.1, revealing that the crystallite size of BiOBr may be attenuated by the surface deposition process onto $ZnFe_2O_4$. The preferential crystal plane of the ultrasonication-deposited BiOBr is (110) rather than (102) crystal plane for BiOBr synthesised by co-precipitation.[81]

### 5.4.2 Morphology

The morphology and composition of the BiOBr-$ZnFe_2O_4$ were analysed by FE-SEM, HRTEM, and EDS. The low-magnification SEM image reveals that a typical 0.9BiOBr-0.1$ZnFe_2O_4$ sample consists of a large number of particles with micro-spherical structure (Figure 5.2 A). The high-resolution SEM image of an individual

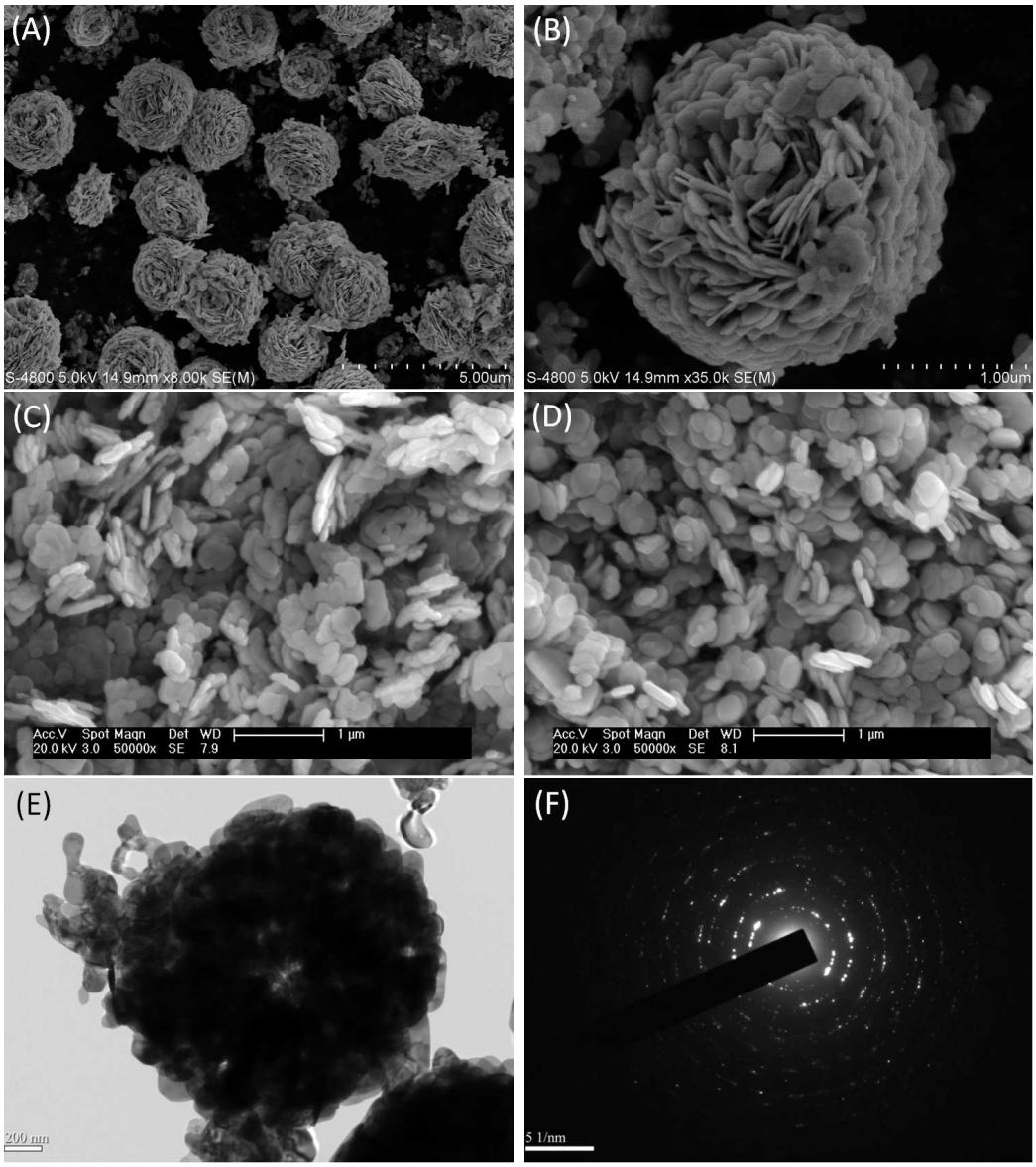


Figure 5.2: (A and B) FESEM images of 0.9BiOBr-0.1$ZnFe_2O_4$ sample at low and high magnification; (C and D) SEM images of 0.5BiOBr-0.5$ZnFe_2O_4$ and pure BiOBr; (E and F) TEM and selected area electron diffraction (SAED) image of 0.9BiOBr-0.1$ZnFe_2O_4$

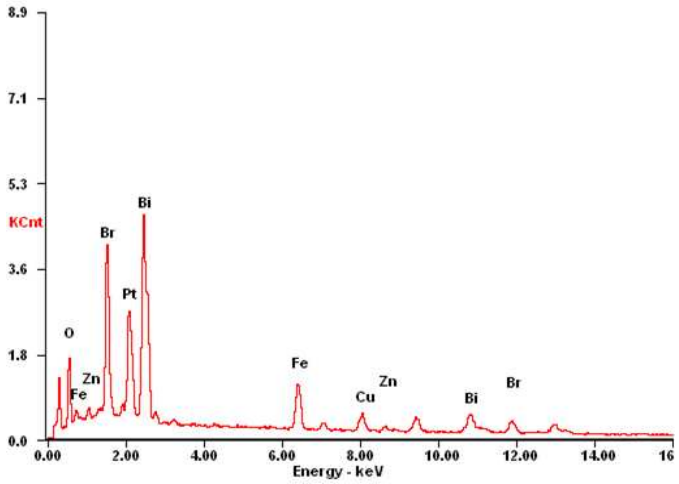


Figure 5.3: EDS spectrum of 0.9BiOBr-0.1$ZnFe_2O_4$

particle (0.9BiOBr-0.1$ZnFe_2O_4$, Figure 5.2 B) shows that the outer part of the microsphere is constructed by numerous thin flakes with a thickness of about 20 nm, which aggregated together to form the hierarchical assembly.[15] The morphology of 0.9BiOBr-0.1$ZnFe_2O_4$ is quite different from pure BiOBr and also the sample with higher amount of $ZnFe_2O_4$ (as shown in Figure 5.2 C, and D). The two different types of surface morphology suggest there might be a critical ratio for BiOBr to $ZnFe_2O_4$, where the spherical shape will disappear once above that point. Energy-dispersive X-ray spectroscopy (EDS) has also been used to carry out the elemental analysis of the BiOBr-$ZnFe_2O_4$ samples, as the spectrum shown in Figure 5.3. EDS analysis of the microsphere reveals that Bi, O, Br, Zn and Fe elements coexist in the BiOBr-$ZnFe_2O_4$ composite materials, where Pt comes from the spray-coated platinum to eliminate the surface charge in the measurement. The TEM image of the 0.9BiOBr-0.1$ZnFe_2O_4$ composite sample further verifies that the microspheres are built with many nanoflakes (Figure 5.2 E). It can be inferred that the individual nanoflakes were formed and aggregated on the surface of $ZnFe_2O_4$ under the ul-

trasound deposition process to form the hierarchical spheres. The TEM image of single microsphere illustrates that it has a hollow centre. The selected area electron diffraction (SAED, Figure 5.2 F) of the assembly suggests that the BiOBr-$ZnFe_2O_4$ composites are polycrystalline including both BiOBr and $ZnFe_2O_4$.[15]

### 5.4.3 Formation scheme

In order to understand the formation conditions of the micro-spherical morphology of BiOBr-$ZnFe_2O_4$, SEM images of the sample with different BiOBr to $ZnFe_2O_4$ ratios were conducted. The spherical morphology disappeared once the BiOBr/$ZnFe_2O_4$ ratio is less than one, because BiOBr cannot fully cover the surface of $ZnFe_2O_4$ assembly. For example, numerous irregularly arranged nano-plates are observed in the SEM image of 0.5BiOBr-0.5$ZnFe_2O_4$ (Figure 5.2 C). On the basis of the SEM observation, the growth and assembly process of the heterojunctions along with the component molar ratio has been proposed here. BiOBr is prone to aggregate into stacked plates without secondary particles existing in the synthetic solution (Figure 5.2 D and 5.4). Given that a suitable amount of $ZnFe_2O_4$ added into the solution, BiOBr flakes will deposit uniformly on the surface of $ZnFe_2O_4$, which serves as 'seeds' in the ultrasound-assisted deposition process, and grows to form a spherical assembly of the BiOBr flaked blocks around the seed. Once the added seeds exceed the desired amount for spherical assembly, the BiOBr flakes cannot fully cover the seeds, leading to irregular morphologies. The gradual change of the colour in the synthetic solutions and UV-Visible spectra also provides some evidence to support this assumption.

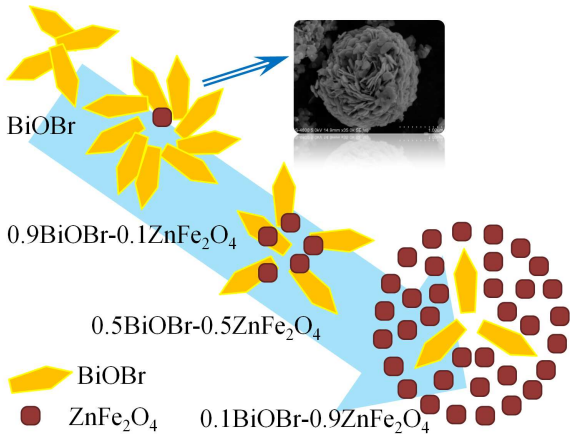


Figure 5.4: Formation scheme of as-generated BiOBr-$ZnFe_2O_4$composites photocatalyst

### 5.4.4 UV-Visible diffuse reflectance (DRS)

The UV-Visible diffuse reflectance absorption spectra (DRS) of the BiOBr-$ZnFe_2O_4$ composites is presented in Figure 5.5. It can be clearly seen from the spectra that the BiOBr-$ZnFe_2O_4$ composite photocatalysts display excellent visible-light absorption, which is consistent with the brown colour of the BiOBr-$ZnFe_2O_4$ composites. The absorption edge has been enlarged remarkably from 420 nm to the range of approximately 500 nm$\sim$600 nm compared to pure BiOBr sample. The band gap of our samples lies in between 2.87 eV and 1.7 eV with a disproportional absorption of light in the visible-light region, suggesting the presence of interactions between $ZnFe_2O_4$ and BiOBr. As is well known, the appropriate band gap of semiconductor material is beneficial for the corresponding photocatalytic activities, which determine the photogenerated electron-hole ($e^- - h^+$) pairs on the surface of the semiconductor.[42] The shift of the absorption edge could facilitate the relatively higher $e^- - h^+$ generation,

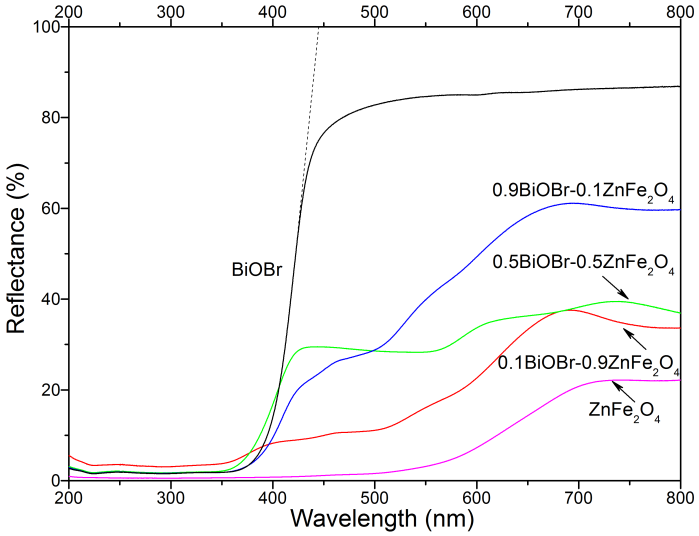


Figure 5.5: UV-Visible DRS spectra of as-synthesised BiOBr-$ZnFe_2O_4$ samples

and thus, more photo-generated holes will be captured and consequently prohibit the recombination of electrons and holes. Therefore, improved photocatalytic activity of semiconductors could be expected eventually. BiOBr-$ZnFe_2O_4$ composite photocatalysts with such energy band gap are very promising for the utilisation of visible-light in comparison to $TiO_2$ with a wide band gap of around 3.2 eV.[116]

### 5.4.5 Electron spin resonance (ESR)

The super-paramagnetic behaviour of the as-prepared BiOBr-$ZnFe_2O_4$ composites is also supported by the subsequent characterisation by electron paramagnetic resonance (EPR/ESR) at room temperature. It is of great significance for the investigation of the magnetic properties of magnetic materials at high frequency because the resonance originates from the interaction between spin and electromagnetic

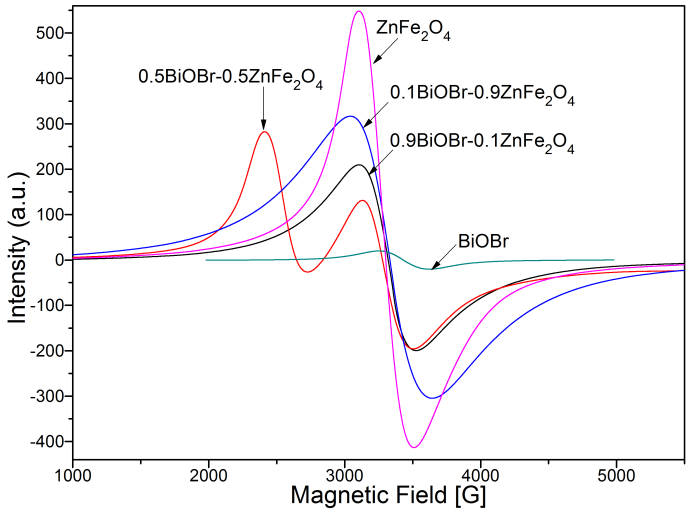


Figure 5.6: ESR spectra of as-synthesised BiOBr-$ZnFe_2O_4$ samples

waves.[91] The resonance line width ($\triangle H_{pp}$), the position corresponds to the zero signal ($H_0$) and the effective $g$-factor are the three parameters that characterise the magnetic properties. The effective $g$-value is determined by the following equation:

$$g = \frac{h\nu}{\beta H}$$

where $h$ is Plank's constant, $\nu$ is the microwave frequency, and $H$ is the magnetic field occurring at the maximum resonance and $\beta$ is the Bohr mageton.[90] As the amount of $ZnFe_2O_4$ increases, the signals gradually get sharper and more symmetrical. Furthermore, an increase in the line width is observed with the decreasing of $ZnFe_2O_4$ composition, the broadening of the resonance line could be attributed to the reduction and/or block of the magnetisation in the composites with lower amount $ZnFe_2O_4$. As shown in Figure 5.6, the $g$-factor for the BiOBr-$ZnFe_2O_4$ samples with an intense, single broad signal is calculated to be around 2.003, which

is ascribed to the paramagnetic centres, i.e., $Fe^{3+}$.[158] In addition to the intense signal, another signal around $g$ =2.583 in the spectra is observed, suggesting that there might be an impurity of $Fe_2O_3$ at an ESR detectable level in the as-prepared 0.5BiOBr-0.5$ZnFe_2O_4$ sample.

### 5.4.6 Photocatalytic performance

#### 5.4.6.1 Reactivity

Figure 5.7 A shows the activity of Rh.B photo-degradation on as-synthesised BiOBr-$ZnFe_2O_4$ composites under visible-light irradiation and Figure 5.7 B shows the absorption spectra variation of Rh.B *versus* irradiation time on the 0.9BiOBr-0.1$ZnFe_2O_4$ sample. The characteristic absorption band of Rh.B at 554 nm diminished quickly, accompanied by slight concomitant blue-shift from 554 nm to 494 nm of the maximum absorption. The rate constant per unit mass, $k$, of each photocatalyst was also listed in Table 5.1. All the photocatalysts showed some photocatalytic activity under visible-light irradiation but importantly Rh.B itself was not decomposed in the absence of catalyst. Pure $ZnFe_2O_4$ showed weak reactivity, on which less than 10% Rh.B was decomposed in 90 min irradiation, which was even worse than P-25 (Degussa $TiO_2$ aerosol). The photo-degradation of Rh.B on P-25 can be attributed to dye-sensitised photocatalysis since P-25 cannot be activated by visible-light.[81] The highest activity was observed over 0.9BiOBr-0.1$ZnFe_2O_4$ sample, on which about 73% Rh.B was degraded in the first 10 min of visible-light irradiation. The photoreaction kinetics constant on the best catalyst is around 3 times and 200

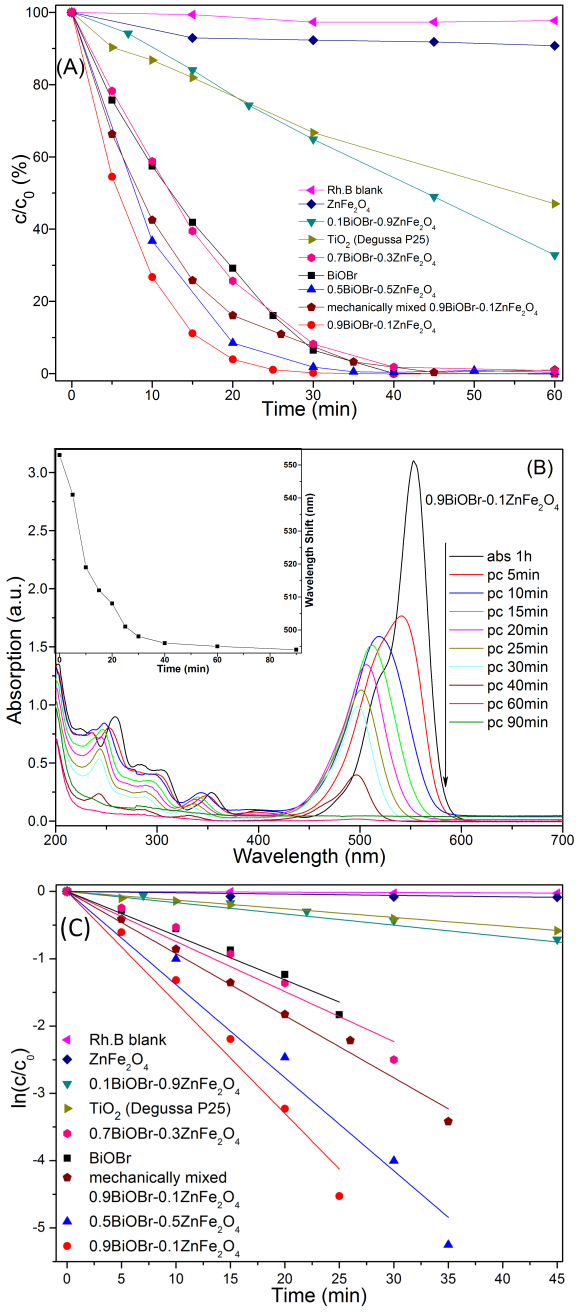


Figure 5.7: (A) Photodegradation of Rh.B over BiOBr-$ZnFe_2O_4$ composites; (B) UV-Visible spectra changes of Rh.B as a function of photoreaction time; Inset: Wavelength shifts as a function of the decrease in absorption maximum; and (C) Photocatalytic removal of Rh.B as a function of irradiation time

times of those of pure BiOBr and $ZnFe_2O_4$ samples, respectively. Although the activity of the composite catalysts decreases as the amount of $ZnFe_2O_4$ increases, 0.1BiOBr-0.9$ZnFe_2O_4$ is still much better than $ZnFe_2O_4$ and is comparable to P-25. The $k_{Rh.B}$ values are not proportional to the molar ratio of BiOBr/$ZnFe_2O_4$, suggesting that the coexistence of $ZnFe_2O_4$ and BiOBr gives rise to some positive synergy for the BiOBr-$ZnFe_2O_4$ heterostructures.

#### 5.4.6.2 Stability

As mentioned in Chapter 4, the semiconductor composites AgBr-BiOBr heterojunctions were not very stable under long-term irradiation and the light-sensitive AgBr may suffer from decomposition and transformation into $Ag_2O$, which can lead to the deactivation of photocatalysts. Here a much more stable semiconductor $ZnFe_2O_4$ has been used, and the stability measurements were carried out under the same condition. It can be seen from Figure 5.8 A that all the BiOBr-$ZnFe_2O_4$ heterojunction composites exhibited good stability after first two cycling tests, though 0.1BiOBr-0.9$ZnFe_2O_4$ cannot decompose Rh.B completely within 1 h, it is relatively stable under long-term irradiation.

Figure 5.8 B displayed the five-time cycling measurements of 0.9BiOBr-0.1$ZnFe_2O_4$, among which showed the best reactivity under visible-light irradiation. Though the photo-reactivity decreased slightly after the fifth run, which could be attributed to the catalyst loss due to the sample collection. Therefore it can be concluded that the BiOBr-$ZnFe_2O_4$ heterojunctions are very efficient and also considerably more stable materials, which make them very promising for the application of the long-term-irradiation stable semiconductor material design in terms of visible-light-responsive

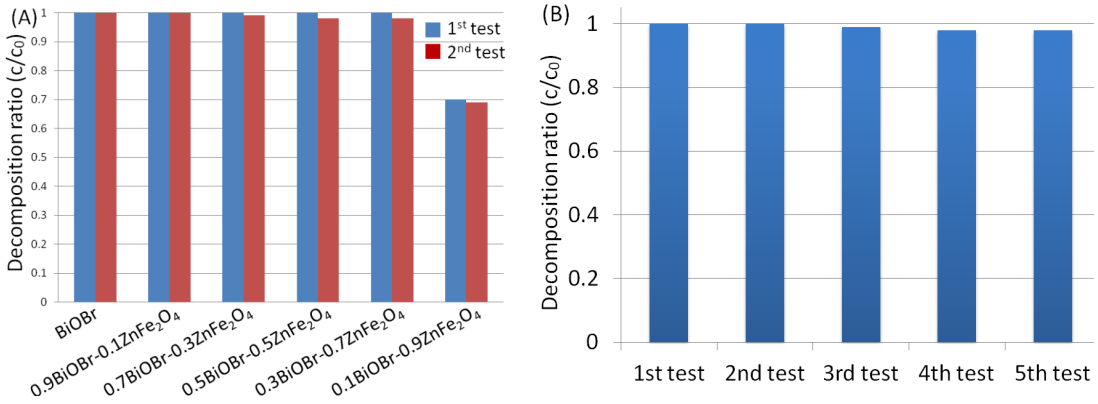


Figure 5.8: (A) Stability tests of BiOBr-$ZnFe_2O_4$ heterojunction materials and (B) five-time cycling tests of 0.9BiOBr-0.1$ZnFe_2O_4$

photocatalytic degradation of organic pollutants.

### 5.4.7 Working mechanism of BiOBr-$ZnFe_2O_4$ heterojunctions

From the electronic structure point of view, as depicted in Figure 5.9, the band potentials of BiOBr and $ZnFe_2O_4$ in the heterostructures fit the requirements to form a heterojunction with a straddling gap, which may facilitate the transfer of charge carriers and resist the $e^- - h^+$ recombination, resulting in improved photocatalytic performance. The potentials of conductance and valence band (CB and VB) edges of BiOBr and $ZnFe_2O_4$ were estimated *via* Mulliken electronegativity theory:[159]

$$E_{VB} = \chi_{Semiconductor} - E^e + \frac{1}{2}E_g$$

where $E_{VB}$ is the VB edge potential, $\chi_{Semiconductor}$ is the electronegativity of the semiconductor, which is the geometric mean of the electronegativity of the constituent atoms, $E^e$ is the standard electrode potential on the hydrogen scale (c.a. 4.5 eV). The VB of $ZnFe_2O_4$ may partially accept the excited electrons from VB of BiOBr and thereby stabilise its photo-generated holes. The photo-generated holes have a strong oxidation potential and serve as active sites responsible for Rh.B photodegradation.[81] Furthermore, $ZnFe_2O_4$ also acts as a sensitiser which considerably broadens the light absorption edges of the heterojunctions in visible-light regions, and may provide photo-generated electrons to sensitise BiOBr.[160] However, $ZnFe_2O_4$ is significantly less active since its photo-generated charges are prone to recombination.[132] On the other hand, the superior reactivity of the BiOBr-$ZnFe_2O_4$ heterojunctions as compared to BiOBr were observed on samples with appropriate molar ratios of $ZnFe_2O_4$ to BiOBr, suggesting that there is a critical ratio for such a positive synergistic effect. Above the critical ratio, excessive $ZnFe_2O_4$ covers the active sites of BiOBr and hinders the visible-light penetrating in the sample to excite BiOBr. This correspondingly deteriorates the photocatalytic activity, as a consequence of less available BiOBr and increased recombination of the photo-generated charges on $ZnFe_2O_4$.

The heterojunction effect can only occur on closely contacted interfaces within the samples.[55] Indeed, enhanced reactivity was observed for the synthesised 0.9BiOBr-0.1$ZnFe_2O_4$ heterojunction than for the mechanically mixed 0.9BiOBr-0.1$ZnFe_2O_4$ sample (Figure 5.7 A) because the latter has more loosely contacted interfaces. The activity of the mechanically mixed 0.9BiOBr-0.1$ZnFe_2O_4$ is higher than BiOBr,

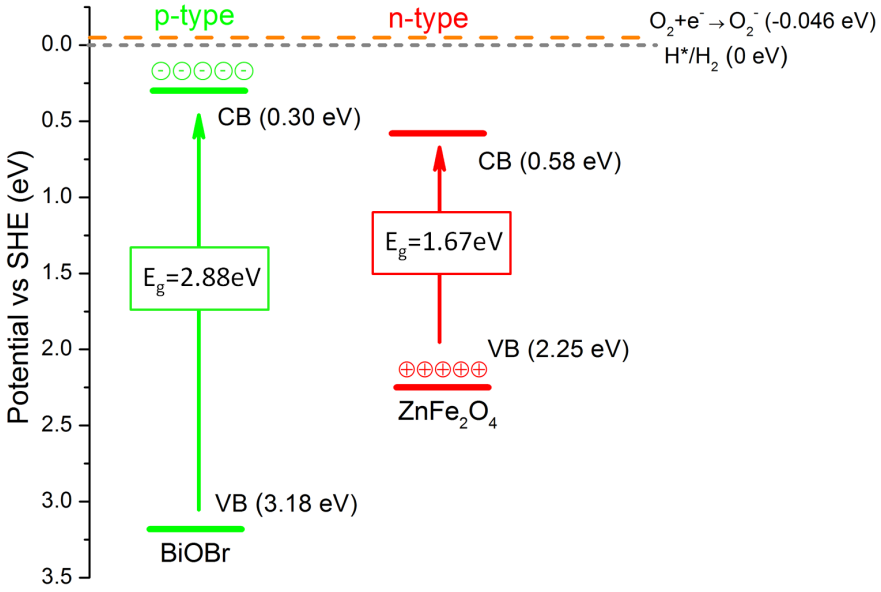


Figure 5.9: Schematic diagram of light excitation and transfer in BiOBr-$ZnFe_2O_4$

which can be depicted in terms of the Z-schemed photocatalysts in an aqueous solution, where the photo-charges may transfer between the two semiconductors with different band gaps.[131] Here, the Z-scheme system can improve the electron separation via the aqueous medium but is less efficient than the corresponding heterojunctions due to the distance limit of the charge transfer.[35] Hence, the enhanced reactivity of the suitable BiOBr-$ZnFe_2O_4$ p-n junctions can be reasonably assigned to the well-aligned straddling band-structures of the BiOBr-$ZnFe_2O_4$ upon their intimately contacted interface.

## 5.5 Conclusions

In this chapter, BiOBr-$ZnFe_2O_4$ heterojunctions have been successfully prepared via an ultrasound-deposition synthesis route for the visible-light-responsive photo-

catalytic decomposition of Rh.B. The BiOBr-$ZnFe_2O_4$ heterojunctions have a particular micro-spherical morphology with appropriate molar ratio of BiOBr to $ZnFe_2O_4$; and this micro-spherical morphology of the BiOBr-$ZnFe_2O_4$ heterojuncted composites significantly improved the absorption ability of visible-light. There is a critical ratio found in the heterostructure, at which point a positive synergism of the heterojunction structure was displayed and controlled both the morphology and thus the absorption ability of visible-light in the junction system. The enhanced reactivity of the suitable BiOBr-$ZnFe_2O_4$ p-n junctions could be tentatively ascribed to the efficient charge separation and transportation through the intimately contacted interface of BiOBr-$ZnFe_2O_4$ and the well-aligned band positions forming a type II straddling gap. The stability of the heterostructure may provide potential application of the design of effective and stable semiconductor composite materials for the photocatalytic degradation.

# Chapter 6

# Ag-modified BiOBr composites

## 6.1 Overview

Surface plasmon resonances on the interface of metallic nano-particles and semiconductors are of great interest for a variety of applications due to the enhanced visible-light absorption ability and the interactions between metals and semiconductors. Generally speaking, excitation of surface plasmons in metal particles placed on a semiconductor might be expected to enhance optical absorption of incident photons within the semiconductor region because of the localised field amplification that occurs.[161] In this chapter, Ag-modified BiOBr composite photocatalysts were prepared through a simple phase-transfer methodology and used for the cleanup of organic dye, Rhodamine B (Rh.B) aqueous solution under visible-light irradiation. X-ray diffraction, ultraviolet-visible diffuse reflectance spectroscopy, and high-resolution X-ray photoelectron spectroscopy confirm that the Ag-modification significantly affected the optical properties, structure and photocatalytic performance of the BiOBr-based semiconductor photocatalysts. In the Ag-modification pro-

cess, a large portion of $Ag^+$ can extract $Br^-$ from BiOBr. The rest of $Ag^+$ may either be photo-reduced by methanol into $Ag^0$, or form $Ag_2O$. In practice, the Ag-modified BiOBr materials exist as the form of a multi-junction photocatalyst $Ag/Ag_2O/AgBr/BiOBr$. The Ag-modification process could significantly enhance the absorption of visible-light but might deteriorate the photocatalytic activity in comparison to the primitive BiOBr in visible-light-driven photodegradation of Rh.B. The activity of Rh.B degradation over such photocatalysts is inversely proportional to its loading amount within the range from 0.2% to 2.0%. Such unusual photocatalytic performance was tentatively attributed to the special band structure of the materials.

## 6.2 Introduction

Great efforts have been made to exploring new catalytic materials for the application of visible-light-driven photocatalysis. Such visible-light-responsive catalysts can be pristine photocatalysts with an intrinsic narrow band gap, for instance, semiconductor compounds of tungsten, molybdenum, bismuth, and metal sulphides.[35, 1, 54, 162, 163, 128, 6] As one of the simplest V-VI-VII bismuth oxyhalides, particularly bismuth oxybromide (BiOBr), has proved with excellent photocatalytic activity and stability in UV-Visible photocatalytic reactions.[98, 81, 151] The band structure of BiOBr favours to prolong the transfer path of photo-excited electrons and thus reduces the recombination of photo-generated electrons and holes, which could be explained by the unique indirect electron-transition in the band gap region.[164] The light absorption of BiOBr is somehow limited by its relatively wide band gap ($E_g \approx 2.9\,eV$).[81]

In previous chapters, forming p-n heterojunction has been confirmed to be an effective yet simple methodology to improve the visible-light absorption and also the photocatalytic performance of the semiconductor materials. However, it requires the band position of both p-type and n-type semiconductors locate in appropriate level, and more importantly, the closely contacted interface of the heterojunction is another crucial factor for the formation of p-n heterojunction. Another methodology, which is doping with nonmetals or transition metals have been extensively adopted to extend the light absorption range of wide band gap photocatalysts.[35, 1, 54] Indeed, iodine-doped BiOBr ($BiOBr_xI_{1-x}$) displayed improved visible-light absorption, though their photocatalytic performance significantly depends on the impurity doping level and the high doping level may deteriorate the photocatalytic activity. [151, 165]

Surface modification through surface deposition of noble metal or semiconductor represents another effective route to extend the absorption region of the primary photocatalyst. For instance, $Ag/TiO_2$ and $AgX/TiO_2$ (X=Cl, Br, I) photocatalysts exhibit performance with respect to $TiO_2$ in photocatalysis applications.[166] Metal Ag nano-particles may trap electrons and thus resist the recombination of photo-generated charge carriers, as well as provide increased visible-light response arisen from the plasmonic effect at the interface of nano-scale silver particle and semiconductor.[166, 52, 167] Plasmon resonance induced by gold and silver could be observed when it is illuminated by light with the wavelength much larger than the size of the metal particle, the charge density is redistributed.

Additionally, AgX may assist photo-generated charge separation as it is supported on the surface of the semiconductors.[166, 140, 133] A classic example is the $AgBr/TiO_2$, in which AgBr is quite stable despite of its photo-sensitivity, show-

ing desirable photocatalytic performance under visible-light irradiation.[166] Within such hybrid or composite photocatalysts, the interfacial energy bias between the well mixed semiconductors offers additional driving force to suppress the recombination of photo-generated charge carriers, while the potentials of their conduction band (CB) and valence band (VB) may be tuned to induce targeted reactions.

In this chapter, Ag-modified BiOBr photocatalysts were prepared and employed to photo-decompose Rh.B under visible-light irradiation. The noble metal-based plasmonic photocatalysts displayed interesting features and properties and various characterisation techniques have been utilised to investigate the structure of the obtained materials and to correlate their photocatalytic reactivity with their structure.

## 6.3 Experimental

### 6.3.1 Synthesis of BiOBr support

The BiOBr semiconductor material was prepared using a simple co-precipitation method. In a typical experiment, $Bi(NO_3)_3 \cdot 5\,H_2O$ was dissolved into acetic acid aqueous solution (5% vol/vol) under vigorous stirring. Light yellowish precipitates formed immediately upon the addition of the aqueous solution containing stoichiometric amount of KBr. After further stirring and ageing for 6 h, the precipitate was thoroughly washed and filtered with distilled water. The obtained hydro-gel was then dried at 65°C overnight in the oven to yield the BiOBr photocatalyst.

### 6.3.2 Surface modification of BiOBr with Ag

The precipitation-deposition method was used to prepare the Ag/BiOBr catalyst. Typically, 0.3 g of BiOBr powder was ultrasonically dispersed into 300 mL of mixed solution of methanol and distilled water (50% vol/vol) prior to adding the appropriate amount of a diluted solution of $AgNO_3$ for producing materials with Ag to BiOBr weight percentage of 0.2, 0.5, 1.0, and 2.0%. The mixture was stirred in the dark for another 60 min before exposure to visible-light irradiation for 40 min under vigorously stirring. The obtained samples were centrifuged and washed with distilled water and 5 mL ethanol before drying. The products were denoted as BiOBr, BiOBr-0.2Ag, BiOBr-0.5Ag, BiOBr-1.0Ag, BiOBr-2.0Ag, which correspond to materials containing 0, 0.2, 0.5, 1.0 and 2.0% Ag, respectively.

## 6.4 Results and discussion

### 6.4.1 XRD characterisation

Figure 6.1 A presents the XRD patterns for the as-prepared photocatalysts. Only the characteristic Bragg diffraction peaks of tetragonal phase BiOBr (JCPDS 73-2061) were observed in the samples with Ag loading amount less than 0.5%, while the materials with Ag loading greater than 1.0% showed extra diffraction peak of AgBr (JCPDS 79-0149), which can be well defined to the prominent (002) crystal phase for AgBr of cubic lattice structure.[168] No obvious shift associated with BiOBr diffraction peaks was observed in the XRD patterns, suggesting AgBr or other species were not incorporated into the crystal matrix of BiOBr. The similar AgBr species were observed as well as reported in Ag/AgBr/BiOBr photocatalysts synthesised

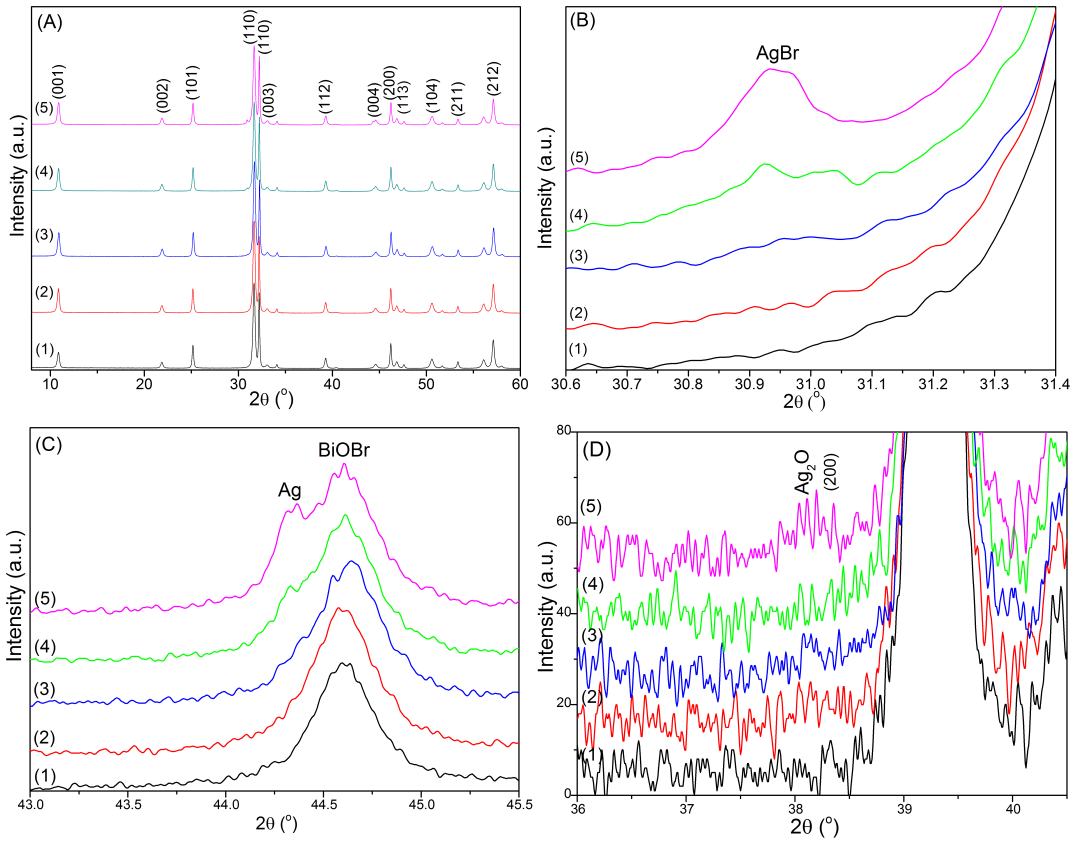


Figure 6.1: (A) XRD patterns of the Ag-modified BiOBr; (B, C, and D) expansion of diffraction data corresponding to AgBr, Ag and $Ag_2O$. (1) BiOBr, (2) BiOBr-0.2Ag, (3) BiOBr-0.5Ag, (4) BiOBr-1.0Ag, and (5) BiOBr-2.0Ag

using ion-exchange method,[149] where pure methanol was adopted as solvent for the photo-reduction of AgBr. Considering the methanol/water mixture involved here, the Ag species could be AgBr, Ag or $Ag_2O$. The mismatch of crystal structure in XRD results concerning BiOBr and AgBr excluded the possibility of forming AgBr-BiOBr solid solutions.

The expansion of the diffraction data in the region of 30° to 31.8° is shown in Figure 6.1 B, which features the (002) Bragg diffraction of AgBr at 30.9° and revealed that AgBr is the dominant species derived from photo-reduction process of $AgNO_3$

as its loading exceeds 1.0%. It is worth noting that no extra $Br^-$ was induced into the system along with the addition of $Ag^+$ in the preparation process, and the formation of AgBr implies that BiOBr must have deviated its stoichiometry in a chemical formula as $BiOBr_{1-x}$, where $x$ corresponds to the molar amount of $Br^-$ in AgBr.

As shown in the extended XRD patterns in Figure 6.1 C, the small shoulder peak appeared at 44.3° as the Ag loading amount exceeds 0.5%. The shoulder peak is associated with the (200) diffraction peak of cubic phased metallic $Ag^0$ (JCPDS: 89-3722).[52] The characteristic XRD signal with respect to (011) diffraction of $Ag_2O$ (JCPDS:72-2108) was clearly observed in Figure 6.1 D for 2.0% Ag-loaded sample at 38°, however too weak to be identified due to the limited resolution of XRD data in this region. From the above discussion, it can be concluded that the Ag-modified BiOBr samples are of multi-junction structure exist as the form of $Ag/Ag_2O/AgBr/BiOBr$. The existence of Ag and $Ag_2O$ may well account for the grey hue of the as-prepared samples. On basis of XRD results for Ag-modified BiOBr samples presented here and for AgX/BiOX compounds in previous chapters, it could be speculated that AgBr is an inevitable species that is generated in the synthesis of Ag-related BiOX materials, through ion exchange between BiOBr and $Ag^+$ out of $AgNO_3$, as shown in the following equation:

$$BiOBr + Ag^+ \rightarrow AgBr + BiO^+$$

Though the dispersion of BiOBr and $AgNO_3$ were immediately reduced to form metallic $Ag^0$ under visible-light irradiation, a small amount of $Ag_2O$ was generated in presence of water in the preparation process. This explains why the $Ag/Ag_2O/AgBr/BiOBr$

Table 6.1: Crystal parameters of the BiOBr and Ag-modified BiOBr photocatalysts

| Samples | Lattice parameter (Å) | | | BiOBr Crystallite size (Å) |
|---|---|---|---|---|
| | $a_{BiOBr}$ | $c_{BiOBr}$ | $a_{AgBr}$ | |
| BiOBr | 3.929 | 8.121 | - | 297 |
| BiOBr-0.2Ag | 3.926 | 8.127 | - | 250 |
| BiOBr-0.5Ag | 3.926 | 8.114 | 5.756 | 353 |
| BiOBr-1.0Ag | 3.928 | 8.125 | 5.765 | 353 |
| BiOBr-2.0Ag | 3.927 | 8.124 | 5.779 | 354 |

multi-junction system exists rather than the Ag/BiOBr composites.

The diffraction intensity of AgBr was found to increase as Ag the loading increases, suggesting that the AgBr crystallite became larger at Ag loading of 1.0% or greater. The crystallite size of BiOBr in the Ag-modified BiOBr materials were calculated from the half maximum full width of the (102) Bragg peak by using the Scherrer equation, and listed in Table 6.1. With a slight expansion of the unit cell, the lattice parameters of BiOBr species in the Ag-modified BiOBr samples are almost similar to those of pure BiOBr ($a = 3.923(5)$ Å and $c = 8.105(2)$ Å).[81] Except for BiOBr-0.2Ag sample, the BiOBr crystallite size of the Ag-modified BiOBr materials are slightly larger than the unadulterated BiOBr. Additionally, the lattice parameters of cubic AgBr in the Ag-modified BiOBr materials were also calculated. It can be seen from Table 6.1 that the AgBr lattice parameter increased as more Ag loaded on the surface of BiOBr.

### 6.4.2 Morphology

Typical SEM images of as-prepared BiOBr and a typical Ag-modified BiOBr samples are shown in Figure 6.2. It can be seen that the obtained samples were flake-like

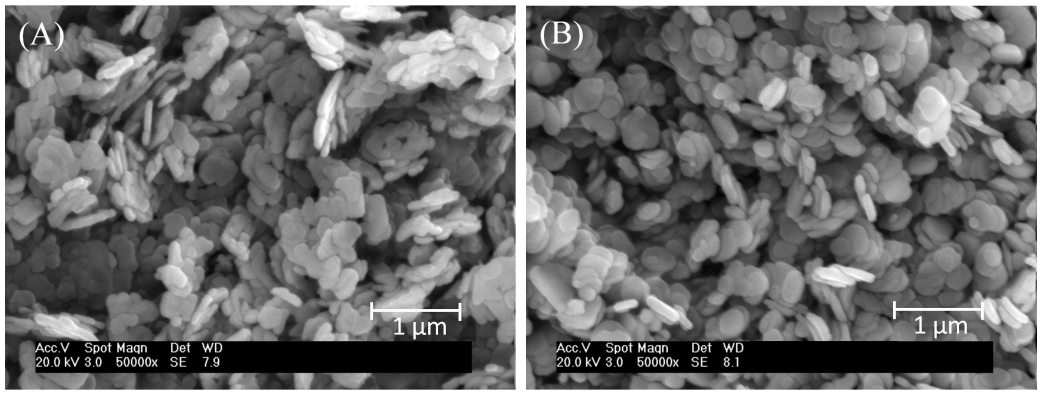


Figure 6.2: FE-SEM images of Ag-modified BiOBr samples: (A) BiOBr and (B) BiOBr-1.0Ag

powders with average diameter of approximately 300 nm and a thickness of 40 nm. The morphology of the Ag-modified BiOBr is quite similar to that of pure BiOBr. It is difficult to distinguish Ag species from the BiOBr surface through SEM image or the energy dispersive X-ray spectroscopy (EDS) of the Ag-modified BiOBr samples due to the low magnification of the electron microscopy utilised and also the low loading amount of Ag on the surface of BiOBr.

### 6.4.3 UV-Visible DRS of Ag-modified BiOBr

Figure 6.3 A shows the UV-Visible absorption spectra derived from the diffuse reflectance spectra (UV-Visible DRS) of the Ag-modified BiOBr samples. All the samples could absorb visible-light with a wavelength over 420 nm in the visible-light region. In comparison with the pure BiOBr sample, the Ag-modification process significantly extended the light absorption to a much broader visible-light region ranging from 425 nm to 800 nm. As shown in Figure 6.3 A, the enhanced light absorption of Ag-modified BiOBr, particularly in the 450 nm to 800 nm region, strongly

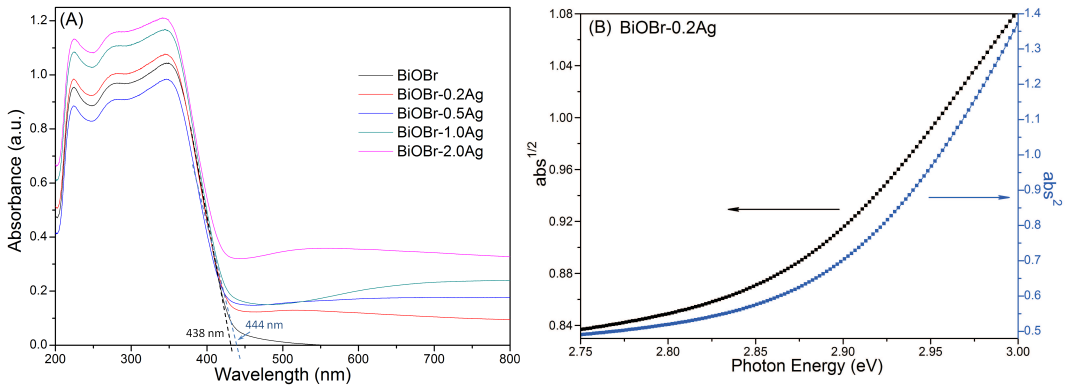


Figure 6.3: (A) UV-Visible spectra of the Ag-modified BiOBr samples and (B) the optical transition property of the BiOBr-0.5Ag sample

depends on the Ag loading amount. The offset observed in Figure 6.3 A could be attributed to the colour change of the Ag-BiOBr samples upon the addition of silver. The colour of the samples become grayer with the increasing amount of Ag, which means they would absorb more visible light in the visible-light region. These results are consistent with the pale white appearance of pure BiOBr and the grey appearance of the Ag-modified BiOBr materials, suggesting new species, Ag and $Ag_2O$, were generated during the Ag-modification process. The corresponding band gap energy ($E_g$) of Ag-modified BiOBr, derived from the formula $E_g = 1239.8/\lambda_g$, are listed in Table 6.2.[81] The $E_g$ of the samples falls in the range from 2.71 eV to 2.84 eV, depending on the Ag loading. The steep drop of the reflectance spectra of the composite photocatalysts were typical of absorption induced by a band gap transition rather than transition from impurity levels which were featured with tailed absorption spectra.

Table 6.2: The optical property and apparent reaction rate constant of the Ag-modified BiOBr

| Sample | $\lambda_{Edge}$ (nm) | $E_g$ (eV) | $k_{Rh.B}$ ($g^{-1}$·min$^{-1}$) |
|---|---|---|---|
| BiOBr | 438 | 2.83 | 0.231 |
| BiOBr-0.2Ag | 442 | 2.81 | 0.2 |
| BiOBr-0.5Ag | 444 | 2.79 | 0.179 |
| BiOBr-1.0Ag | 450 | 2.76 | 0.14 |
| BiOBr-2.0Ag | 457 | 2.71 | 0.093 |
| $TiO_2$ P-25 | 386 | 3.21 | 0.014 |

The surface plasmon band (SPB) is a strong and broad band observed in absorption in the UV-Visible spectrum for metallic nanoparticles bigger than 2 nm.[169] The wavelength and intensity of the surface plasmon depends on the size, shape, orientation and surface roughness of the sample material. It is well known that noble metals, such as Au, Cu and Ag demonstrate strong plasmon resonances. In our series of samples, the improved visible-light absorption in the region from 425 nm to 800 nm can be attributed to Ag-modification process. Similar phenomena were reported for AgBr-Ag-$Bi_2WO_6$ and Ag-AgBr-BiOBr, where the enhanced absorptions were ascribed to the plasmonic effects of the induced nano-scaled Ag particles.[149] In our Ag-modified BiOBr samples, the plasmonic effect arisen from nano-scaled $Ag^0$ could also be observed within 500 nm to 600 nm wavelength region; however, the contribution of $Ag_2O$ and Ag cannot be excluded and must be accounted.

The electron transition characteristics (direct or indirect) of the photocatalysts were analysed by processing the sharp absorption edge according to the equation: $\alpha h\nu = A(\nu - E_g)^{n/2}$; where $\alpha$, $\nu$, $E_g$ and $A$ are absorption coefficient, light frequency, band gap, and a constant, respectively. Among them, n is determined by the type of

optical transition of a semiconductor.[53] For a specific semiconductor, the absorption coefficient is linear with $(h\nu - E_g)^2$, where n=4 for direct transitions in the region around absorption edge; while it is linear with $(h\nu - E_g)^{\frac{1}{2}}$, in which n=1 for indirect transitions. The band gap energy ($E_g$) of the Ag-modified BiOBr semiconductors could thus be estimated from the data plot of $(h\nu - E_g)^{\frac{1}{2}}$ and $(h\nu - E_g)^2$ versus photon energy ($h\nu$), respectively.[51, 74] Figure 6.3 B displayed the transition plots of BiOBr-0.5Ag, where the nonlinear plots of $(\alpha h\nu)^{n/2}$ versus $h\nu$ indicated that the composite samples are not direct or indirect semiconductors. The unusual transition feature of the Ag-modified samples can be reasonably assigned to the band structure changes of the samples induced by the Ag-species in the BiOBr materials.

### 6.4.4 Surface elemental analysis

The surface element composition and oxidation state of the Ag-modified BiOBr samples were identified by high-resolution X-ray photoemission spectroscopy (HR-XPS). Figure 6.4 A shows the Ag $3d$ spectra of three Ag-modified BiOBr samples. The two broad XPS peaks are corresponding to Ag $3d_{3/2}$ and $3d_{5/2}$ , respectively.[170, 171] The peaks at 368.2 eV and 374 eV can be assigned to $3d_{5/2}$ and $3d_{3/2}$ spectra of $Ag^0$, which is the dominant Ag species.[172, 142] The peak intensity of Ag $3d$ spectra increased with the increasing loading amount of Ag in the samples. However, it is not possible to remove the soluble oxygen and hydroxyl group completely under the photo-deposition treatment, which would facilitate $Ag^+$ to form $Ag_2O$.

Figure 6.4 B demonstrates the Bi $4f$ spectra of Ag-modified BiOBr samples with Ag loading of 0.2, 0.5, and 1.0%. The strong peaks at 165 eV and 160 eV were characteristic core line of Bi $4f_{5/2}$ and Bi $4f_{7/2}$ in BiOBr. As the Ag loading amount

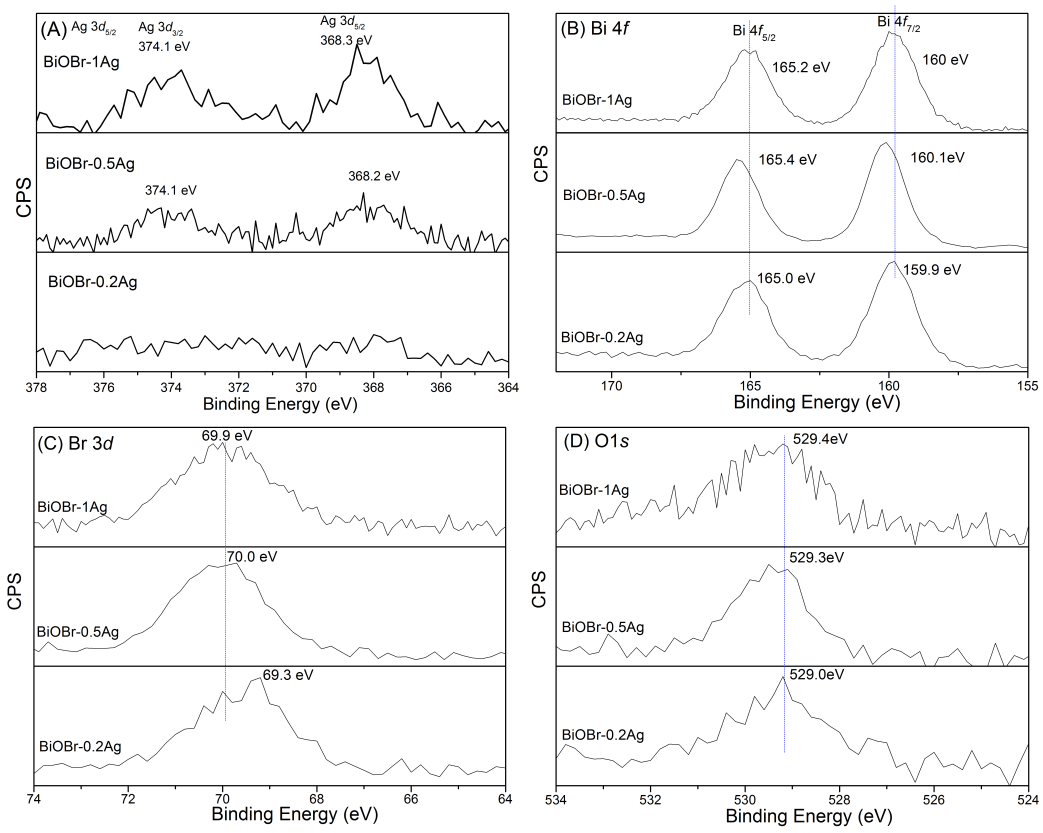


Figure 6.4: The X-ray photoemission spectra of (A) Ag $3d$, (B) Bi $4f$, (C) Br $3d$ and (D) O $1s$

increased from 0.2 to 1.0%, the Bi $4f_{5/2}$ and $4f_{7/2}$ peaks show slight blue shifts which should be induced by Ag-modification process. Figure 6.4 C shows the XPS spectra of Br $3d$, where the binding energy around 68 eV could be assigned to the $Br^-$ in the BiOBr and AgBr. As the Ag loading amount increased, the binding energy of $Br^-$ also displayed blue-shift effect.[92] Figure 6.4 D illustrates the broad symmetric O $1s$ XPS spectra, which are ascribed to $O_2^-$ in BiOBr and the peak in Ag-modified BiOBr samples remains unchanged comparing to that in unadulterated BiOBr.[173] The slight B.E shifts for Ag and Br in the BiOBr-0.2Ag sample were thought to arise from the relatively lower electronegativity of Ag ($\chi_{Ag}$ =1.93) with respect to Bi ($\chi_{Bi}$ =2.02), which produces weaker chemical binding in the Ag-Br bond in comparison to the Bi-Br bond.[174, 88] The changes in B.E for those elements indicate that there are strong interactions between each other, and these interactions are dependent on the Ag loading amount. The XPS results further confirmed the multi-junction nature of the Ag-modified BiOBr photocatalysts.

### 6.4.5 Photocatalytic performance

Surface adsorption of the organic dye is the key step for photocatalytic reaction and plays important roles in determining photocatalytic degradation activity.[81] Figure 6.5 shows the light absorption spectra of Rh.B solution after the establishment of adsorption-desorption equilibrium. It can be seen that all the samples possess almost the same absorption spectra regardless of the Ag-modification, implying that Ag-modification process does not affect the surface adsorption capacity of Rh.B over BiOBr significantly.

The activity of the Rh.B photodegradation over the Ag-modified BiOBr sam-

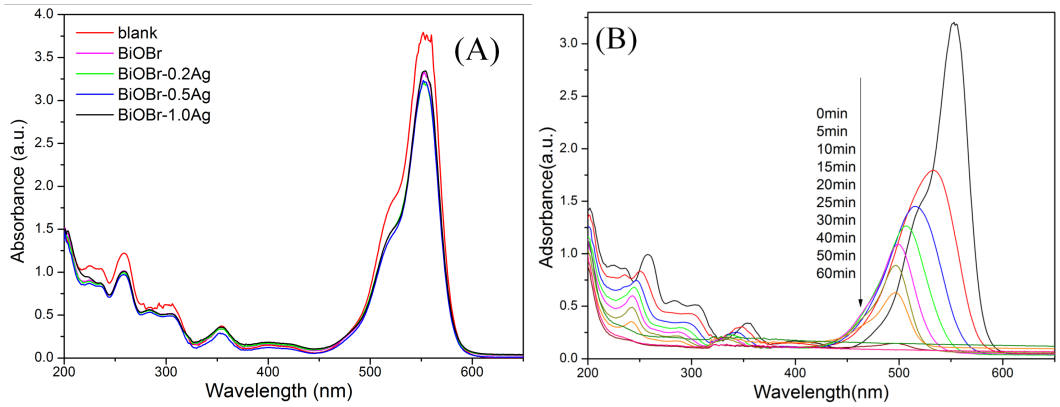


Figure 6.5: (A) UV-Visible absorption spectra of the Rh.B solution upon the establishment of the adsorption-desorption equilibrium and (B) the time-dependent spectra of the Rh.B solution upon its photodegradation over the BiOBr-0.2Ag sample

ples can be compared through the variation of characteristic Rh.B absorption band at 554 nm under visible-light irradiation.[122] As shown in Figure 6.6 A, the concentration of Rh.B remains unchanged under the visible-light irradiation without the catalyst, while it may be completely decomposed in 40 min over BiOBr and Ag-modified BiOBr catalysts. The derived plots of the Rh.B decomposition over the photocatalysts were displayed in Figure 6.6 B and the calculated rate constants of corresponding catalysts, $k$, were listed in Table 6.2. The results indicated that the photocatalytic performance of the Ag-modified BiOBr samples significantly depends on the Ag loading amount and their Rh.B photodegradation reactivity declined with Ag loading amount in the following order: BiOBr>BiOBr-0.2Ag>BiOBr-0.5Ag>BiOBr-1.0Ag>BiOBr-2.0Ag. The activity results suggest that the Ag-modification process of BiOBr through the current methodology may deteriorate the photocatalytic activity. This degraded activity may arise from the formation of $Ag_2O$ via photodegradation of AgBr on the surface of BiOBr.

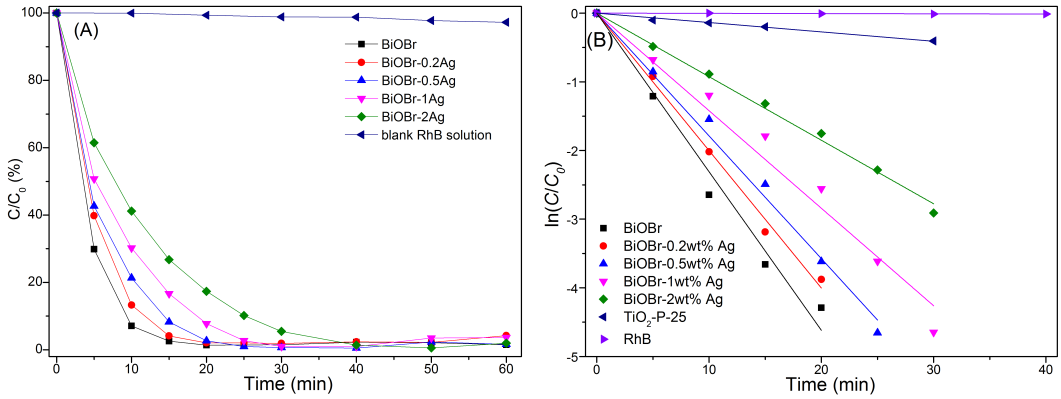


Figure 6.6: (A) Photodegradation of Rh.B over the Ag-modified BiOBr samples and (B) plot of $\ln(C/C_0)$ against irradiation time

Figure 6.7 presents the schematic band structure of the hybrid Ag-modified BiOBr photocatalysts. Although the AgBr and BiOBr may generate heterojunction structure which could facilitate the separation of photo-generated charge carriers as confirmed in previous chapter, the surface $Ag_2O$ would mask the active sites of AgBr and BiOBr, as well as block the incident irradiation onto the reactive species, therefore prevent the generation of charge carriers. From the band structure point of view, $Ag_2O$ has more positive conductance band and more negative valence band than those of AgBr and BiOBr (as shown in Figure 6.7), suggesting it has weaker reduction and oxidation ability in photocatalytic reaction. It has been well demonstrated that nano-sized Ag particles on the surface of catalysts would significantly contribute to the photocatalysis, particularly the plasmonic effect at the interface of metal and support would promote the process.[166, 149] However, the Fermi level of $Ag^0$ is estimated to be close to the standard potential of hydrogen, indicating that $Ag^0$ cannot improve the photo-activity of the Ag-modified BiOBr samples, or

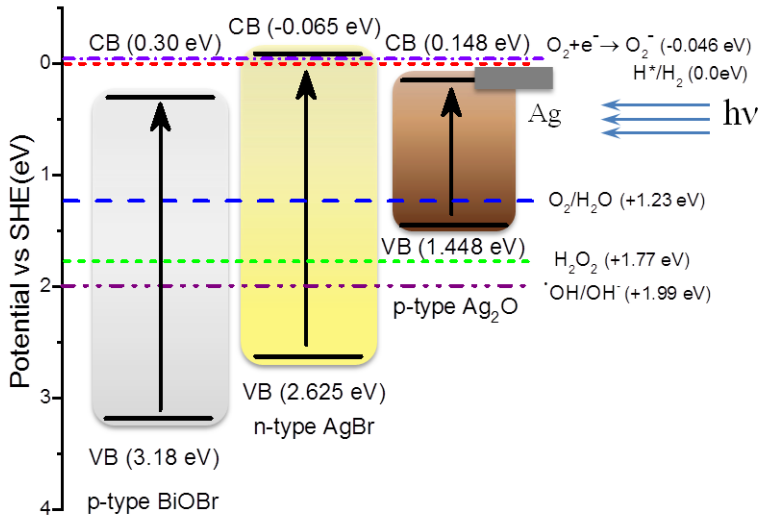


Figure 6.7: Schematic diagram of band structure of the Ag-modified BiOBr

cannot compensate the negative contribution from the trace amount of $Ag_2O$. In addition, the formation of AgBr withdraws $Br^-$ from BiOBr, which deformed BiOBr and generated surface defects, and the defects might serve as the recombination centres of the photo-generated charge carriers and therefore deteriorate reactivity of the Ag-modified BiOBr samples.

It is worth noting that the photodegradation of Rh.B is a gradual decomposition process, which is significantly different from the photocatalytic decomposition of methylene blue (MB) over $TiO_2$-based semiconductors.[163, 128] Figure 6.5 B shows the absorption spectra variation of Rh.B versus irradiation time for BiOBr-0.2Ag sample. The characteristic absorption band of Rh.B at 554 nm diminished quickly, accompanied by a slight concomitant red-shift from 554 nm to 492 nm of the maximum absorption. This phenomenon could be interpreted as the light absorption of

the incomplete mineralised intermediates of Rh.B during the irradiation process.

## 6.5 Conclusions

A series of low loading amount Ag-modified BiOBr samples have been prepared via a two-step precipitation-photodeposition methodology and the Ag species exist in the catalyst as Ag, AgBr and $Ag_2O$. It has been proved that the visible-light absorption ability of the composites can be significantly improved by Ag-modification process, particularly in the region of 430 nm to 800 nm; however, the photocatalytic activity of the Ag-modified BiOBr catalysts might be decreased in the Rh.B photodegradation in comparison to the unadulterated BiOBr. The declined activity could be ascribed to the formation of $Ag_2O$ on the surface of BiOBr, which might mask the reactive sites of either AgBr or BiOBr, and also block the incident irradiation of visible-light. The removal of $Br^-$ from BiOBr to generate AgBr will lead to the surface defects of the BiOBr catalyst, which negatively affect the separation of the photo-generated charge carriers. The total negative effects of AgBr and $Ag_2O$ surpassed the positive effect of Ag particles, therefore the decreased reactivity can be expected.

# Chapter 7

# $BiOBr_xI_{1-x}$ solid solutions

## 7.1 Overview

In this chapter, a continuous series of $BiOBr_xI_{1-x}$ photocatalysts with variable band position have been synthesised by an efficient yet simple ultrasonification method. Various characterisation techniques have been employed to investigate the properties of the solid solution materials and the correlation between the solid solution and their photocatalytic performance. The band gap energy of the $BiOBr_xI_{1-x}$ solid solutions can be tuned artificially and the improved visible-light response was attributed to the well-tuned band structures and the particulate electronic properties.

## 7.2 Introduction

In previous chapters, a range of methodologies have been used and investigated to improve the photocatalytic performance of BiOBr for the application in solar energy utilisation. The methods include ultrasonification and co-precipitation, formation of

p-n heterojunction, and noble metal deposition, etc..[31, 175, 176] The most important problem to be solved is how to find an efficient semiconductor for the photocatalysis which has visible-light-responsive absorbance and reactivity under sunlight irradiation as visible-light accounts for more than 45% in the solar spectrum.[177] For a semiconductor material, the electronic band gap energy ($E_g$) and the position of valence band (VB) and conduction band (CB) are considered to be the most important properties when choosing a material as photocatalyst.

In order to get a highly efficient semiconductor photocatalyst with desirable band structure, the factors that determine the photocatalytic activity must be elucidated.[98, 156, 149] Methodologies such as impurity doping and surface decoration have been extensively utilised and investigated. Among them, fabrication of solid solution semiconductors can artificially control the band position by varying the composition ratio of the component from one end to the other. This strategy has been developed and reported in the system such as $(AgIn)_xZn_{2(1-x)}S_2$, $Sr_2Nb_xTa_{2-x}O_7$ and Cu(II)-$(Sr_{1-y}Na_y)(Ti_{1-x}Mo_x)O_3$ solid solutions,[178, 39, 179] since the oxidising ability of a hole in a semiconductor photocatalyst is influenced by the valence band position where the holes locate. However, it is difficult to attain a precise adjustment to the electronic structure of the ideal semiconductors with such complex components.[180] Theoretically, the formation of solid solutions leads to changes in the electronic band gap energy, the crystal phase, surface area, and also the local electronic structure, all of which can influence the photocatalytic performance.

On basis of the previous work, bismuth oxyhalides, especially BiOBr can be considered as a promising semiconductor photocatalyst with an intrinsic lamellar structure and an indirect band gap which endows BiOBr with excellent mobility and

a prolonged transfer path for photogenerated electrons without changing the band structure.[168] However, the band gap energy of BiOBr is around 2.9 eV, suggesting that it cannot absorb the visible-light with the wavelength larger than 430 nm,[132] which limited its practical application. On the other hand, BiOI, with narrow band gap of 1.7 eV to 1.83 eV, absorbs sunlight up to 653 nm or even larger wavelength ($\lambda < 700$ nm) but shows little photocatalytic activity. With the aim of optimising the electronic properties, the partial substitution of bromine by iodine in the BiOBr system has been proposed. It is expected that the VB and CB positions could be controlled in $BiOBr_xI_{1-x}$ solid solutions. Here in this chapter, solid solutions $BiOBr_xI_{1-x}$ have been prepared via a simple aqueous ultrasonification method, in which the as-synthesised $BiOBr_xI_{1-x}$ samples exhibit composition-dependent optical properties. They also display excellent activity in visible-light-driven photodegradation of Rh.B which could be correlated with the band gap and band edge positions.

## 7.3 Experimental

### 7.3.1 Synthesis of $BiOBr_xI_{1-x}$ solid solutions

To prepare the $BiOBr_xI_{1-x}$ solid solutions, stoichiometric amounts of KBr and KI were dissolved in distilled water (50 mL) to obtain a clear solution. $Bi(NO_3)_3 \cdot 5\,H_2O$ was dissolved in 50 mL aqueous solution containing 5 mL acetic acid (HAc) under magnetic stirring. The aqueous solution of KX was added into the $Bi(NO_3)_3 \cdot 5\,H_2O$ solution under ultrasonification for 30 min. The colours of the precipitates ranged from white to orange between the end member BiOBr to BiOI. The mixture was washed with distilled water and ethanol, and then dried in the oven overnight at the

temperature of 80°C.

### 7.3.2 Band position calculation

The energy of valence band edge, $E_{VB}$, is a measure of the ionization potential, $I$, of the bulk material with respect to vacuum as the zero energy reference. The conduction band edge energy, $E_{CB}$, is a measure of the electron affinity, $A$, of the compound. The Fermi level is the absolute electronegativity, $-\chi$, of a pristine semiconductor, a value which lays in the energy halfway between the conduction band and valence band edges. The energy difference between Fermi energy and vacuum level corresponds to the work function ($\phi$). [48] The relationship between band edge energies and electronegativity can be expressed as:

$$E_{CB} = -A = \mid \chi \mid -\frac{1}{2}E_g = \chi - E^e - \frac{1}{2}E_g$$

$$E_{VB} = -I = \mid \chi \mid +\frac{1}{2}E_g = \chi - E^e + \frac{1}{2}E_g$$

$\chi$ can be expressed *via* the geometric mean of the absolute electronegativity of the constituent atoms, and the electronegativity of each atom is defined as the arithmetic mean of the atomic electron affinity ($A$) and the first ionisation energy ($I$). For instance, the electronegativity $\chi$ of the sample $BiOBr_{0.75}I_{0.25}$ is expressed in the form:

$$\chi_{BiOBr_{0.75}I_{0.25}} = \sqrt[3]{(\chi_{Bi} \cdot \chi_O \cdot \chi_{Br}^{0.75} \cdot \chi_I^{0.25})}$$

where the electronegativity of Br atom can be expressed as $\chi_{Bi} = \frac{1}{2}(I_{Bi} + A_{Bi})$, $E^e$ is the energy of free electrons on the hydrogen scale ($\sim$4.5 eV), and $E_g$ is the band

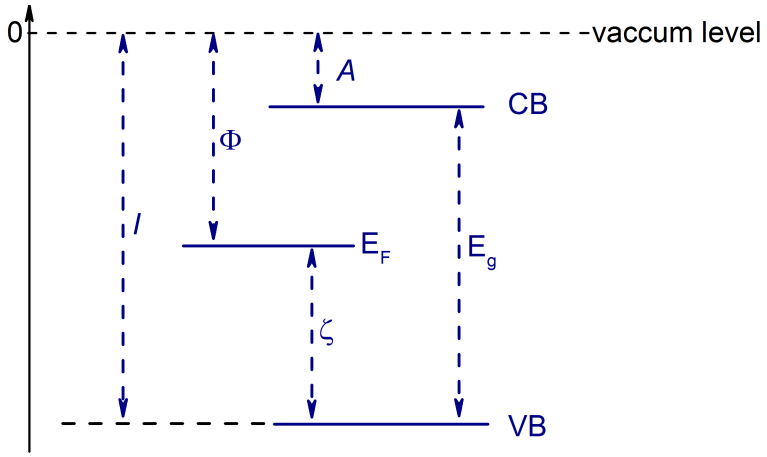


Figure 7.1: Schematic energy diagram of a semiconductor

gap of the semiconductor. The VB edge potential of a semiconductor at the point of zero charge can be expressed empirically *via* Mulliken electronegativity theory.[147] Figure 7.1 shows a schematic energy diagram of a semiconductor.

## 7.4 Results and Discussions

### 7.4.1 Crystal structure

The PXRD patterns for $x = 1.0$ and $x = 0$ of the as-synthesised $BiOBr_xI_{1-x}$ materials (Figure 7.2 A) are identical to those reported for $P4/nmm$ tetragonal BiOBr (JCPDS 73-2061) and BiOI (JCPDS 01-0445) crystal phase, respectively.[98, 181] The characteristic peaks gradually shift to a smaller angle $\theta$ with the increasing amount of iodine, (i.e., a larger spacing between the diffraction planes), which indicates that the larger ionic radius of $I^-$ (2.20 Å vs. 1.96 Å) is expanding the crystal lattice (Figure 7.2 B).[70] The XRD results confirm that the as-prepared samples were not the

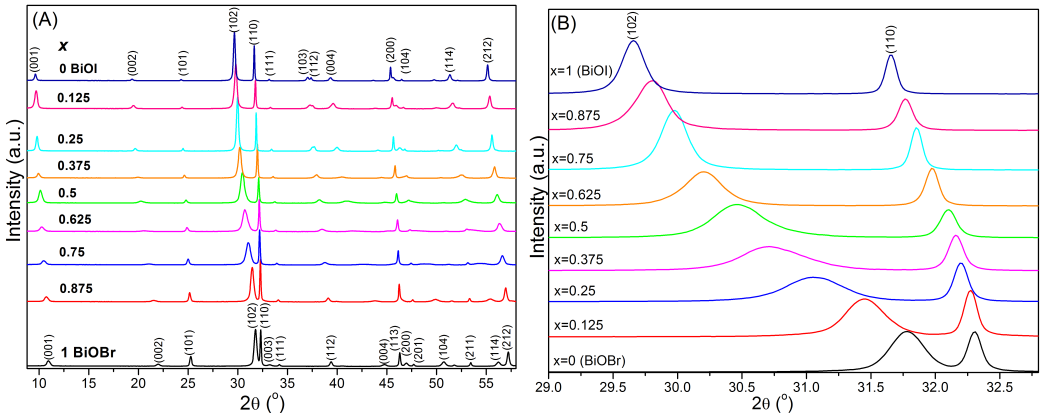


Figure 7.2: (A) XRD patterns of $BiOBr_xI_{1-x}$ materials and (B) Characteristic X-ray diffraction of (102) and (110) peaks ranging from 29 to 33°

Table 7.1: Lattice parameters and cell volume of the $BiOBr_xI_{1-x}$ materials

| $x$ | Lattice parameter (Å) | | $a/c$ | Cell volume ($Å^3$) |
|---|---|---|---|---|
| | $a$ | $c$ | | |
| 1 | 3.9294(2) | 8.1154(5) | 0.484 | 125.303 |
| 0.875 | 3.9356(3) | 8.2854(9) | 0.475 | 128.332 |
| 0.75 | 3.9437(6) | 8.489(2) | 0.465 | 132.028 |
| 0.625 | 3.9533(7) | 8.690(7) | 0.455 | 135.812 |
| 0.5 | 3.9606(5) | 8.8248(2) | 0.449 | 138.429 |
| 0.375 | 3.9662(4) | 8.915(1) | 0.445 | 140.240 |
| 0.25 | 3.9759(3) | 9.0250(9) | 0.441 | 142.665 |
| 0.125 | 3.9895(5) | 9.119(1) | 0.438 | 145.139 |
| 0 | 3.9995(1) | 9.1669(4) | 0.436 | 146.634 |

mixtures of BiOBr and BiOI, but $BiOBr_xI_{1-x}$ solid solutions. The lattice parameters $a$ and $c$ were calculated and are listed in Table 7.1. They increased monotonically with the increasing amount of iodine. From BiOBr to BiOI the lattice parameter $a$ grows by only 0.07 Å (from 3.93 to 4.00 Å) while $c$ increases by 1.05 Å (from 8.12 to 9.17 Å), as shown in Figure 7.3 A. The expansions in lattice parameters suggested that the iodine has successfully been incorporated in BiOBr lattice.[165]

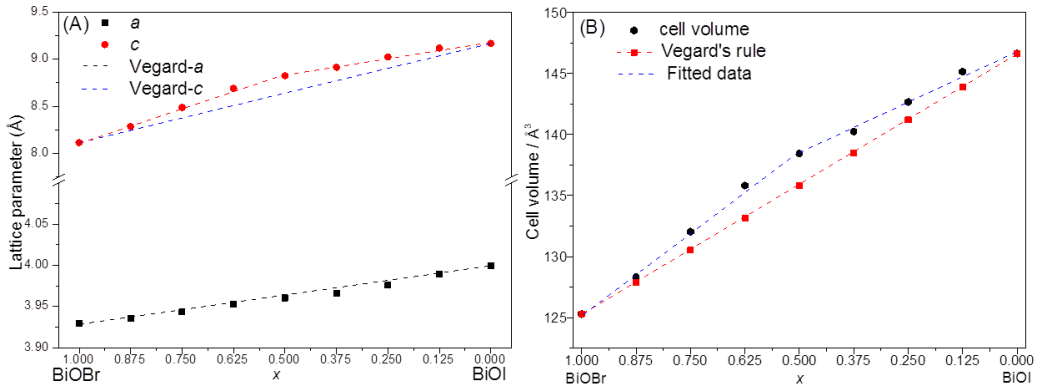


Figure 7.3: plots of lattice parameter (A) $a$ and $c$ fitted by vegard's rule and (B) Cell volume of the $BiOBr_xI_{1-x}$ samples as a function of I doping level $x$.

It can be observed from Figure 7.3 A is that the increase of the a parameter is linear with I concentration, however, $c$ parameter lies above that expected by linear interpolation derived from the Vegard's rule. Deviations from Vegard's law has been reported in previous reports, such as the BiOX-BiOY systems and the $TiO_2$-$SnO_2$ etc..[70, 182] These values indicate that in BiOBr the displacement of Br in the [001] direction is larger than the displacement in the [100] direction. Therefore, the deviation of the $c$ parameter may be a result of the incorporation of the larger I onto Br sites in the [001] directions than in the [100] direction.[183]

The cell volumes ($V = a^2c$) are also shown in Table 7.1, an expansion could be observed among the solid solution samples where the deviation from Vegard's law is greatest for $x$ =0.5. Generally, the values close to those from a linear interpolation between pure BiOBr and BiOI according to the Vegard's rule:

$$t(x) = t_A(1-x) + t_Bx = t_A + (t_B - t_A)x$$

$t_A, t_B$ being the lattice parameters of end members A and B, here referred as BiOBr and BiOI, respectively (Figure 7.3). Both the lattice parameter values of $a$ and $c$ are almost linear with I concentration except for the samples with $x$=0.25-0.75, which is due to the additional effect (i.e. the anion size difference).[70] In binary metal, unlimited solubility could only be observed when the ionic radii difference of the component is smaller than 15%.[174] The similar rule also exists for the general case of solid solutions. For BiOX, the corresponding difference between the halogen ionic radii (Br=1.96 Å, I=2.20 Å) is about 12% for Br/I, which confirms with the results of solid solution system generated.[70] The as-calculated lattice parameters confirm that the incorporation of iodine significantly affected the crystal structure in the solid solution system.

### 7.4.2 Optical properties

The obtained products showed a gradient evolution in colour from offwhite to brick red (as shown in Figure 7.4 C), which is in agreement with the red-shifted spectra displaying sharp absorption edges as a function of $x$ illustrated in Figure 7.4 B. The gradual colour change also confirmed with the offset observed in Figure 7.4 A. Diffuse reflectance spectra (DRS) of all the samples (Figure 7.4 A) demonstrated that the solid solution semiconductors possess absorption edges that extend into the visible-light region. In the pure BiOBr and BiOI sample, the absorption edge situated at the wavelength around 440 nm and 670 nm, respectively; and both of the calculated values are in accordance with the literature.[81, 181] The corresponding band gap energies ($E_g$) of $BiOBr_xI_{1-x}$ solid solution samples, derived from

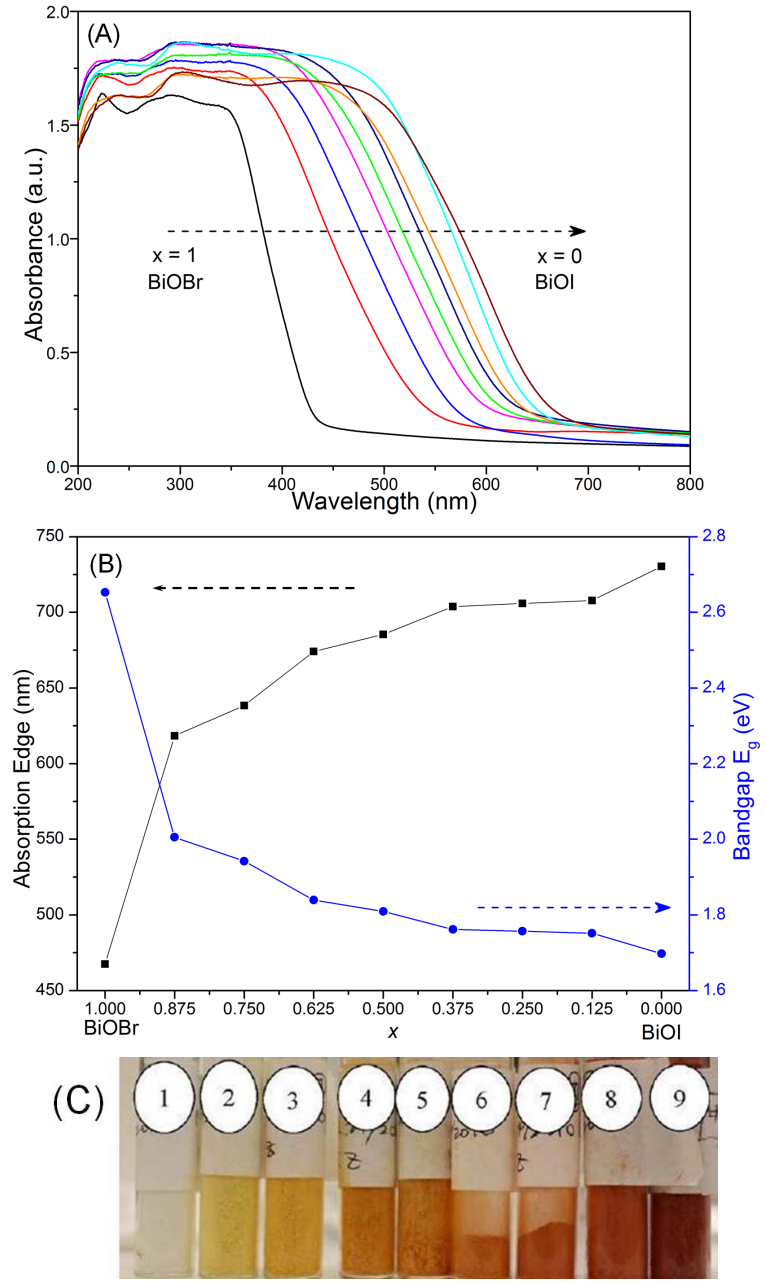


Figure 7.4: (A) UV-Visible diffuse reflectance spectra, (B) absorption edge and band gap energy ($E_g$) *versus* $x$ value plots, and (C) the colour change of $BiOBr_xI_{1-x}$ solid solution samples

Table 7.2: Lattice parameters, electronegativity $\chi$, band gap energy, valence band (VB)/conduction band (CB) position and reaction kinetics of the $BiOBr_xI_{1-x}$ materials

| $x$ | $\chi$ (eV) | $E_g$ (eV) | $E_{VB}$ (eV) | $E_{CB}$ (eV) | $\xi$ (eV)[1] | $k_{Rh.B}$ $(min^{-1} \cdot g^{-1})$ |
|---|---|---|---|---|---|---|
| 1 | 6.1739 | 2.653 | 3.00 | 0.347 | 1.40 | 0.0928 |
| 0.875 | 6.1441 | 2.005 | 2.648 | 0.643 | 1.30 | 0.11 |
| 0.75 | 6.1145 | 1.942 | 2.588 | 0.646 | 0.89 | 0.150 |
| 0.625 | 6.0850 | 1.839 | 2.508 | 0.669 | – | 0.107 |
| 0.5 | 6.0556 | 1.809 | 2.463 | 0.654 | 0.87 | 0.0559 |
| 0.375 | 6.0264 | 1.762 | 2.411 | 0.649 | – | 0.0833 |
| 0.25 | 5.9973 | 1.757 | 2.378 | 0.621 | – | 0.0802 |
| 0.125 | 5.9684 | 1.752 | 2.346 | 0.594 | 0.73 | 0.0201 |
| 0 | 5.9396 | 1.698 | 2.289 | 0.591 | 0.70 | 0.0104 |

[1] $\xi$ is the energy gap between the VBM and the Fermi level

the equation: $E_g = 1239.8/\lambda_g$ are listed in Table 7.1.[53] The band gap energy of all the samples falls in the range from 1.85 eV to 2.81 eV, where an obvious decrease can be observed with the increasing amount of iodine in the $BiOBr_xI_{1-x}$ solid solutions (Figure 7.4 B). The steep shape of the reflectance spectra of the solid solution semiconductors was the typical absorption induced by transition band gap rather than transitions from impurity doping levels which featured with tailed absorption spectra.

### 7.4.3 Morphology

The morphology of materials is an important factor that may influence the catalytic performance of the photocatalysts. The morphologies of the as-synthesised $BiOBr_xI_{1-x}$ solid solutions are shown in Figure 7.5, it can be observed that all the samples consisted of flake-like structure and the particle size of the samples grad-

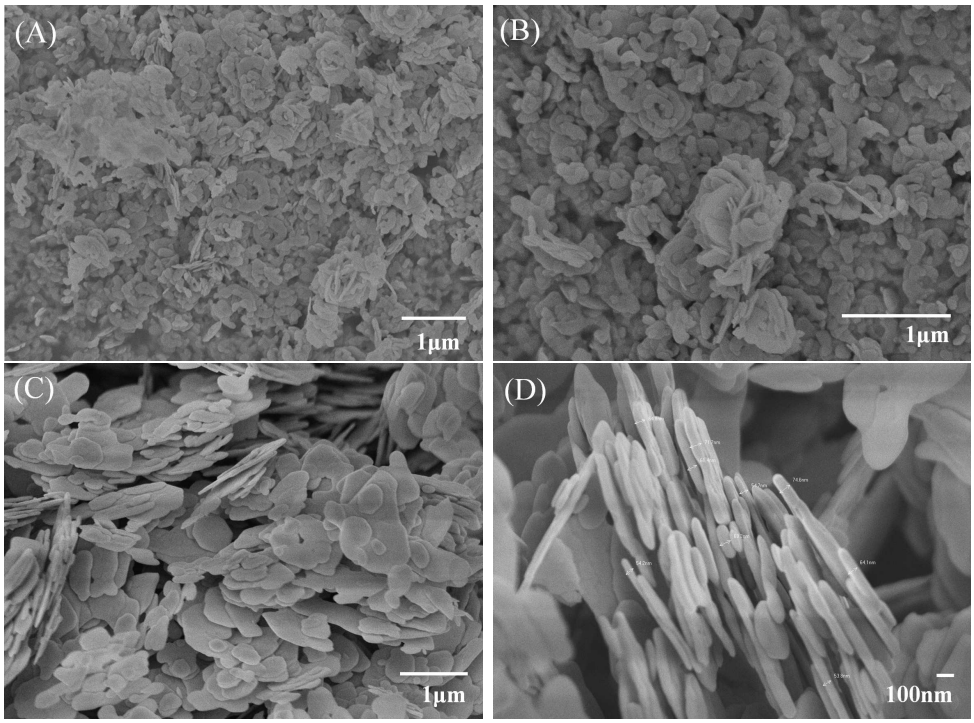


Figure 7.5: SEM images of (A) BiOBr , (B) $BiOBr_{0.5}I_{0.5}$, (C) $BiOBr_{0.875}I_{0.125}$ and (D) BiOI

ually increased from 200 nm to 500 nm with the inducing of I onto BiOBr. There is no obvious difference between the BiOBr and BiOI thin flakes with the thickness about 100 nm (Figure 7.5 D), therefore, it can be inferred that the morphology of the $BiOBr_xI_{1-x}$ samples does not affect the composition-dependent photocatalytic performance of the solid solution samples.

### 7.4.4 Surface elemental analysis

The surface elemental composition and valence states of the $BiOBr_xI_{1-x}$ samples were identified by high-resolution X-ray photoelectron spectroscopy (XPS) (Figure 7.6) and all the peaks' position and attribution were listed in Table 7.3. Two strong peaks

in Figure 7.6 A located around 164.1 eV and 158.7 eV were characteristic Bi $4f_{5/2}$ and $4f_{7/2}$ in the $BiOBr_xI_{1-x}$ solid solutions, suggesting the Bi oxidation state to be $Bi^{3+}$. As the I/Br ratio increased, the Bi $4f_{5/2}$ and $4f_{7/2}$ peaks systematically shift towards lower binding energy. Accordingly, as shown in Figure 7.6 B, the photoelectron lines in O $1s$ spectra also exhibit red shift for the $Bi1OBr_xI_{1-x}$ solid solutions in comparison with the unadulterated BiOBr. The Br $3d$ spectra (Figure 7.6 C) around 68.0 eV with a slight peak red shift has also been detected with the increasing amount of I in the solid solutions. The red shifts observed in binding energy (B.E) for Bi, O and Br in the $BiOBr_xI_{1-x}$ samples were thought to arise from the introducing of iodine with lower electronegativity (2.66) than that of Br (2.96), which leads to weaker interactions in the O-Br (Bi-Br) bond in comparison to the O-I (Bi-I) bond in the solid solution system. The intensity of the Br $3d$ peaks reduced with the decreasing amount of Br in the $BiOBr_xI_{1-x}$ compound, and vice versa for I $3d$ spectra (Figure 7.6 D). The changes of both binding energy position and intensity in all the elements indicated that there are certain interactions along with the inducing of iodine upon the formation of $BiOBr_xI_{1-x}$ solid solutions, depending on the Br/I molar ratio. Those interactions may affect the chemical environment of the materials with respect to pure BiOBr.

### 7.4.5 Photocatalytic activity

To determine the photocatalytic activity of the as-prepared solid solution $BiOBr_xI_{1-x}$ photocatalysts, Rh.B was used as the organic pollutant with an initial concentration

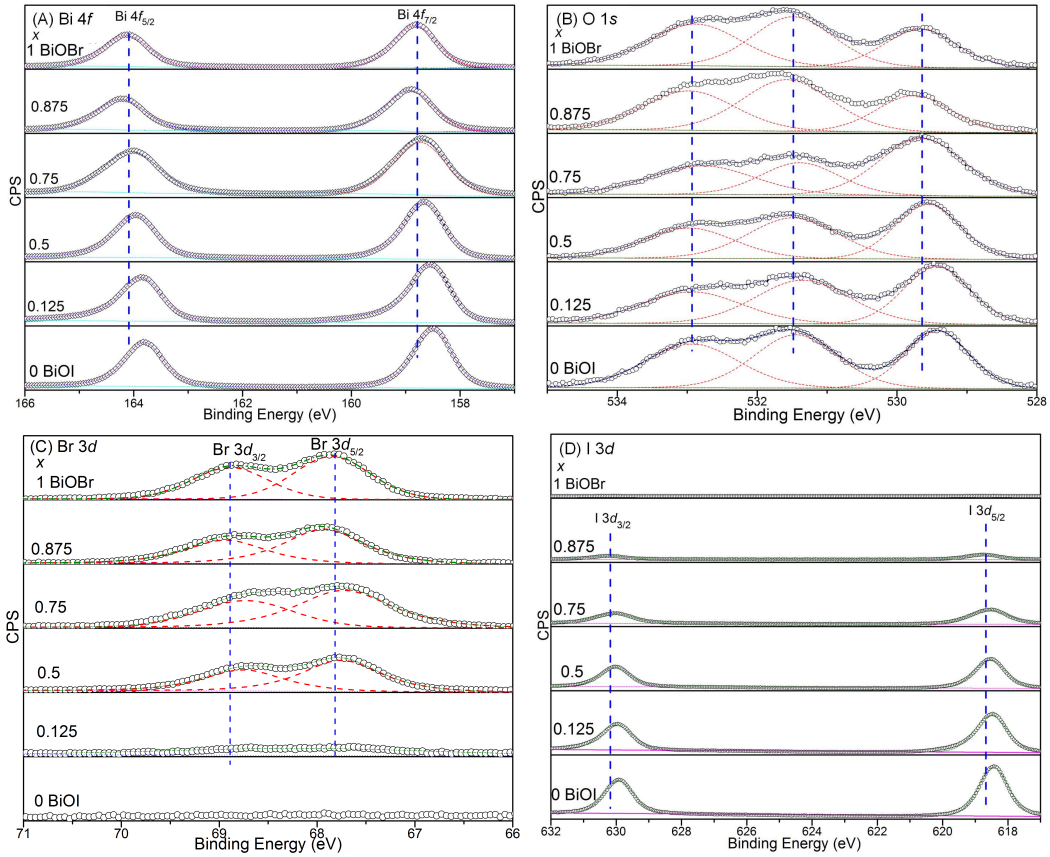


Figure 7.6: XPS spectra of (A) Bi $4f$, (B) O $1s$, (C) Br $3d$, (D) I $3d$ of the $BiOBr_xI_{1-x}$ samples where $x$ =1, 0.875. 0.75, 0.5, 0.125 and 0.

Table 7.3: Peak position and attribution of the elements' XPS spectra

| Sample | Bi $4f_{5/2}$ | Bi $4f_{7/2}$ | O $1s$ | Br $3d_{3/2}$ | Br $3d_{5/2}$ | I $3d_{3/2}$ | I $3d_{5/2}$ |
|---|---|---|---|---|---|---|---|
| BiOBr | 164.13 | 158.78 | 529.63 | 68.83 | 67.83 | - | - |
| $BiOBr_{0.875}I_{0.125}$ | 164.24 | 158.89 | 529.74 | 68.94 | 67.82 | 630.24 | 618.74 |
| $BiOBr_{0.875}I_{0.25}$ | 163.99 | 158.69 | 529.59 | 68.69 | 67.64 | 630.04 | 618.54 |
| $BiOBr_{0.5}I_{0.5}$ | 163.97 | 158.67 | 529.57 | 68.72 | 67.64 | 630.02 | 618.52 |
| $BiOBr_{0.125}I_{0.875}$ | 163.82 | 158.52 | 529.47 | 68.67 | 67.62 | 629.97 | 618.47 |
| BiOI | 163.83 | 158.53 | 529.43 | - | - | 629.88 | 618.43 |

of 20 mg/L. The photocatalytic degradation process is monitored by evaluating the variation in maximal absorption in UV-Visible spectra at 553 nm. $C$ was the absorption of Rh.B at the wavelength of 553 nm and $C_0$ was the absorption of Rh.B after the adsorption-desorption equilibrium on $BiOBr_xI_{1-x}$ photocatalysts before irradiation. Figure 7.7 A displays the concentration changes of Rh.B at 553 nm as a function of irradiation time during the degradation process in aqueous $BiOBr_xI_{1-x}$ photocatalysts. The photocatalytic performance of the as-synthesised solid solutions is significantly dependent on the Br/I molar ratio, and the introduction of iodine in lower amounts improved the photoactivity of the solid solution samples, among which the $BiOBr_{0.75}I_{0.25}$ sample showed the highest photocatalytic activity under visible-light irradiation among all the $BiOBr_xI_{1-x}$ samples. However, the photocatalytic activity of the $BiOBr_xI_{1-x}$ solid solutions decreased when the Br/I molar ratio exceeds one, implying the excessive amount of iodine decreases the reactivity under visible-light irradiation. With the photocatalytic degradation of Rh.B, the absorption peak at 553 nm blue-shifts and turns broadened at the same time, which agrees well with the previous reports.

The reaction kinetics $k_{Rh.B}$, has also been calculated upon the equation: $-kt = ln(C/C_0)$, where $C$ and $C_0$ represent the current and initial concentration of the Rh.B solution, respectively. As shown in Figure 7.7 B, generally the samples with relatively lower amount of iodine displayed better activity compared to those with higher amount. The apparent photocatalytic sequence of the $BiOBr_xI_{1-x}$ solid solutions (as listed in Table 7.1) were correlated to the Br/I molar ratio, in the order as follows: $BiOBr_{0.75}I_{0.25} > BiOBr_{0.875}I_{0.125} \approx BiOBr_{0.625}I_{0.375} > BiOBr > BiOBr_{0.375}I_{0.625} > BiOBr_{0.25}I_{0.75} > BiOBr_{0.5}I_{0.5} > BiOBr_{0.125}I_{0.875} > BiOI$. When bromine dominates the

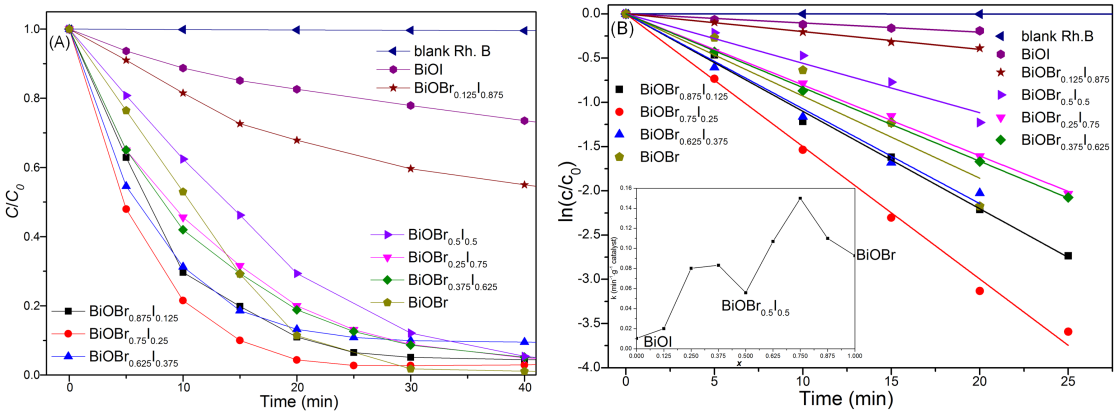


Figure 7.7: (A) Photocatalytic activity and (B) reaction kinetics ($k_{Rh.B}$) of the $BiOBr_xI_{1-x}$ samples (inset: $k_{Rh.B}$ *vs.* $x$)

halide species in the solid solutions, the $BiOBr_xI_{1-x}$ solid solution exhibits higher activity for the degradation of Rh.B than pure BiOBr with increasing I substitution for Br in BiOBr lattice. However, the activity begins to drop when the nominal $x$ is less than 0.5, the slightly decayed activity could be attributed to the predominant iodine part which deteriorates the efficient BiOBr part in the solid solution.

In order to testify the advantage of $BiOBr_xI_{1-x}$ solid solutions, the most effective $BiOBr_{0.75}I_{0.25}$ sample was compared with the physical mixture of BiOBr and BiOI with the molar ratio of 0.75:0.25 under the same photocatalytic degradation conditions, as shown in Figure 7.8 D. It is apparent that the physically mixed sample exhibited much lower reactivity compared to the solid solution sample under visible-light irradiation. This is mainly because the BiOBr and BiOI in the mixture acted as independent photocatalysts rather than a coupled system, which would be unfavourable for the transfer of photogenerated charge carriers from one phase to another. The results indicated that the generation of a solid solution can improve the semiconductor photocatalytic activity significantly.

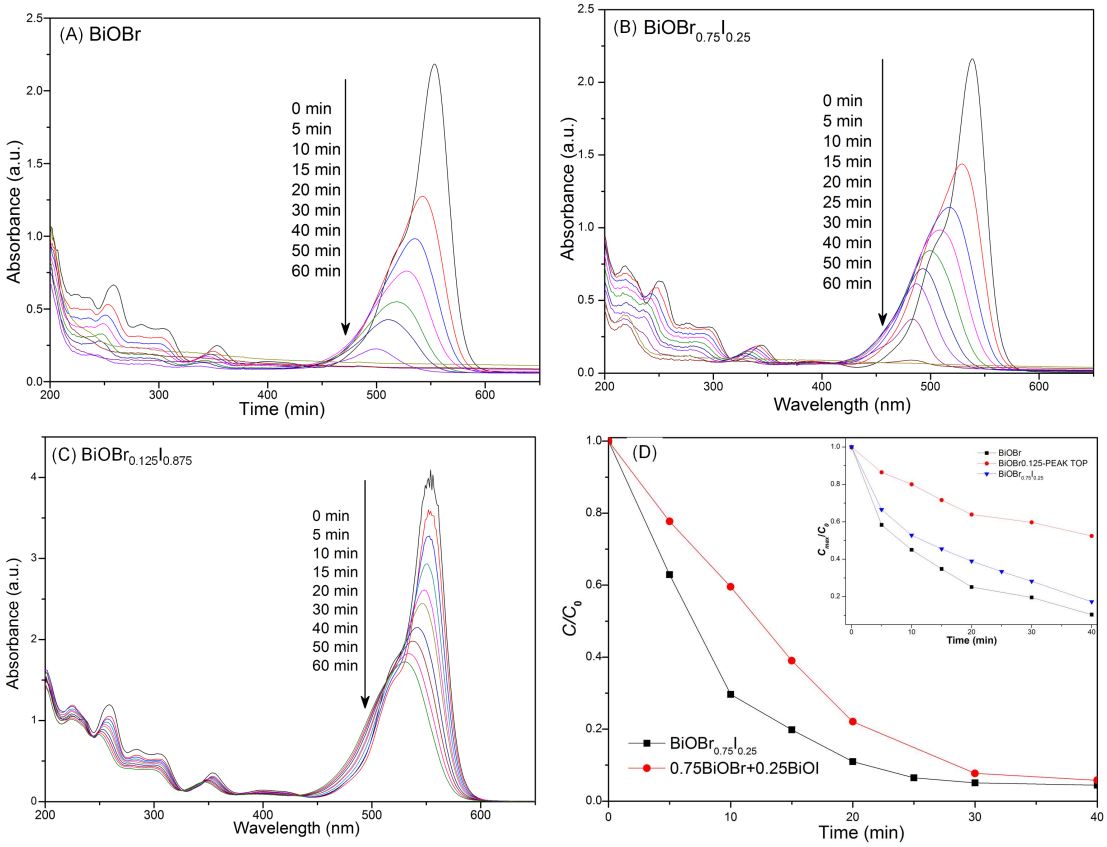


Figure 7.8: (A-C) temporal evolution of the spectra during the photodegradation of Rh.B over $BiOBr_xI_{1-x}$ photocatalysts (x=1, 0.75 and 0) and (D) the comparison of degradation of Rh.B over $BiOBr_{0.75}I_{0.25}$ and physical mixture of BiOBr and BiOI samples in the molar ratio of 0.75:0.25; inset is the plot of peak top of selected photocatalysts

The Rh.B decomposition is a gradual process, and the absorption spectra variation of Rh.B versus irradiation time for selected $BiOBr_xI_{1-x}$ samples is shown in Figure 7.8 A-C. The characteristic absorption band of Rh.B located at 554 nm diminished quickly, accompanied by a slight concomitant blue-shift from 554 nm to 492 nm of the maximum absorption. This phenomenon could be interpreted as the light absorption of the incomplete mineralised intermediates of Rh.B during the irradiation process. This agrees well with previous report of Zhao *et al.* in the $TiO_2$/Rh.B system.[22] The blue-shift of the absorption band is caused by de-ethylation of Rh.B due to the attack by one of the active oxygen species on the N-ethyl group. When the de-ethylation process is complete, the absorption band shifts to the wavelength of 498 nm and Rh.B turns to rhodamine. Gradually rhodamine decomposed because of the further destruction of the conjugated structure. The different decomposition processes of Rh.B were observed in Figure 7.8 A-C. The sample BiOBr possesses a relatively slower change in de-ethylation of Rh.B compared to the $BiOBr_{0.75}I_{0.25}$ sample. Correspondingly, the colour of dye solution changed from red to colourless in a short time period. However, the sample $BiOBr_{0.125}I_{0.875}$ displayed the process of de-ethylation of Rh.B initially and then the slower destruction of the conjugated structure. The colour change of the Rh.B dye solution was observed from red to a light green/yellow, which is in accordance with the peak top shift plot shown in the inset of Figure 7.8 D.

### 7.4.6 Band structure analysis

The decrease in electronic band gap of $BiOBr_xI_{1-x}$ solid solutions along with decreasing electronegativity of halogen may reflect the changes in the electronic structure1

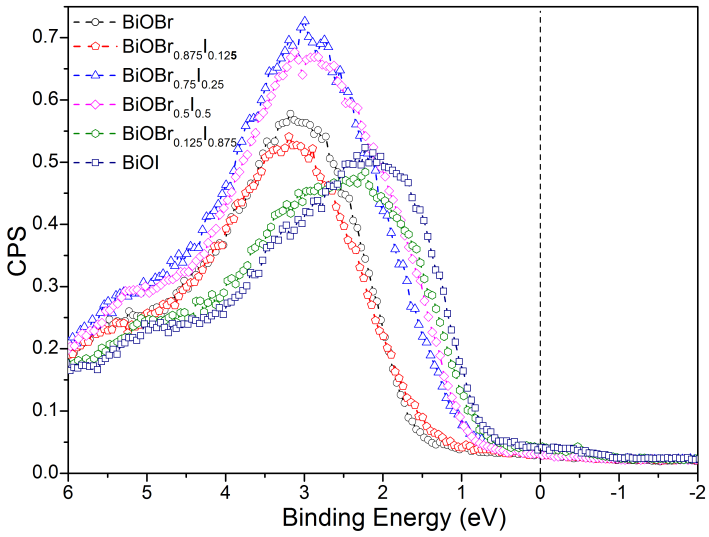


Figure 7.9: Valence band maximum (VBM) XPS spectra of the $BiOBr_xI_{1-x}$ samples

changes of BiOX at both the conduction band minimum (CBM) and the valence band maximum (VBM). XPS is able to probe the changes through measurement of the shift in core spectral lines that would be induced by the changes in energy of the VBM. The position ($\xi$) of the valence band maximum relative to the Fermi level ($E_f$) can be determined from a linear extrapolation of the band edge in XPS, the values of $\xi$ have been calculated and concluded in Table 7.2. The results exhibits an energy shift in $\xi$ with increasing I concentration in agreement with bulk band gap shifting, it is also confirmed by previous literature.[126, 151]

Generally in n-type semiconductors the Fermi level located closer to the CBM, while in p-type semiconductors, the Fermi level located closer to the VBM. As shown in Figure 7.9, the Fermi energy has been pinned in the middle of the band gap, in which the valence band offset energy is about half of the band gap energy. This phenomenon is caused by excitation of electron-hole pairs by the flood gun.[184]

The region of the valence band of bismuth oxyhalides (BiOX) consists the hybridisation of Bi $6s$, O $2p$ and X $np$ orbitals, in which the dominant contribution comes from the X $np$ orbitals (here X corresponds to Br and/or I, and X $np$ orbitals correspond to Br $4p$ and I $5p$). The Bi $6p_z$ orbitals are the major contributor in the region of the conduction band, where the Bi $6p_z$ orbitals in one Bi sheet of each $[Bi_2O_2]^{2+}$ layer are arranged in-phase with those in the other Bi sheet.[72, 126] According to the previous reports, the Bi atom is coordinated with 4 O and 4 Br/I atoms in the $BiOBr_xI_{1-x}$ solid solution samples, generating a $BiO_4X_4$ anti square prism structure.[72] Compared with the band structure of pure BiOBr, the doping of iodine (I $5p$), with different electronegativity can form new bands with hybridised Br $4p$ and O $2p$ orbital between the original valence band and conduction band of BiOBr. Thus, the levels of conduction band minimum are less affected by the induction of iodine, whereas the levels of valence band maximum are controlled by the ratio of Br/I. $BiOBr_xI_{1-x}$ solid solutions with a desired band gap narrowing could be achieved, and visible-light response was obtained as shown in the UV-Visible DRS spectra (Figure 7.4). There is an obvious increase in intensity above the top of the valence band; tailing into the lower part of the band gap to about 1.5 eV binding energy. The tailing is more significant at the higher iodine doping level in the $BiOBr_xI_{1-x}$ solid solutions as can be seen in XPS, which means the introduction of iodine changed the position of the top of the valence band. The results further confirmed that the valence band is dependent of the composition of the solid solution, leading to the band position shift in the solid solution system.

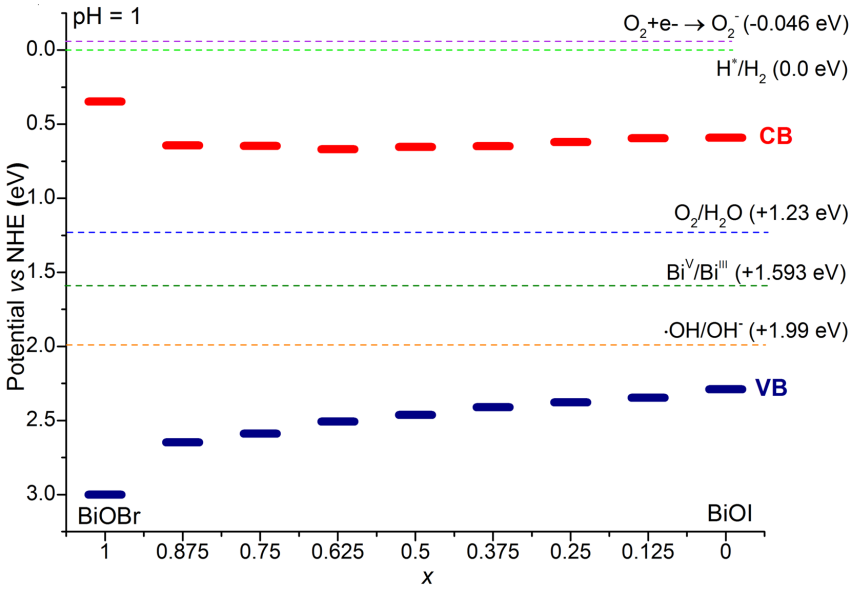


Figure 7.10: As-calculated band position of as-synthesised $BiOBr_xI_{1-x}$ solid solutions

The XPS core level characteristic peak positions have been correlated with the corresponding VB/CB changes as the XPS peak trends may reflect the VBM/CBM situation in the solid solutions. The CB potentials increased with the amount of iodine, which is synchronised with the O 1*s* XPS peak shift. It can be seen from Figure 7.10 B and Table 7.1 that the $E_{VB}$ decreased from 3.0 eV to 2.29 eV with the increasing amount of iodine, implying that the oxidation ability becomes weaker. The as-calculated valence band position of the $BiOBr_xI_{1-x}$ samples are in a similar order comparing to the XPS VBM spectra, which further confirms our assumption that the substitution of iodine with smaller electronegativity successfully changed the composition/position of VB structure. However, the absorption spectra of the $BiOBr_xI_{1-x}$ samples showed a strong absorption in the visible-light region and a red shift with the increasing iodine amount. As listed in the diagram (Figure 7.10 B), the

calculated VB edge potential of all the $BiOBr_xI_{1-x}$ samples locates below the standard redox potentials of $\cdot OH/OH^-$ (1.99 eV), suggesting that the photo-generated hole is far more oxidative than ·OH radical. However, the photo-generated holes could not oxidise $OH^-$ to form the ·OH radicals because of the more negative reduction potential of $Bi^V/Bi^{III}$. Therefore, it is theoretically reasonable that the photo-degradation of Rh.B could be interpreted as the reaction with the photo-generated holes rather than the species such as ·OH radicals generated during the photocatalysis process. The CBM potential of the $BiOBr_xI_{1-x}$ samples is not strong enough to reduce the $O_2$ into the oxygen radical by the photo-excited electrons, because the electrochemical potential for single-electron reduction of oxygen is -0.046 eV.[81] Considering practical applications, further electronic structure improvement should reduce the conduction band of the photocatalysts to the position more negative than the reduction potential of $O_2$ (-0.046 eV) and simultaneously achieve high quantum efficiency in the wide visible region.

It is of great importance to investigate the correlation between the crystal, electronic structure of the $BiOBr_xI_{1-x}$ solid solutions and the photocatalytic performance.

1. **Electronegativity** ($\chi$) It has been confirmed that the inducing of iodine with lower electronegativity ($\chi_I = 2.66$) successfully lowered the electronegativity of the solid solution $BiOBr_xI_{1-x}$, and the effect intensified with the increasing amount of iodine in the system. It is the role essentially played by $\chi_I$ that affected the absorption ability in visible-light region, and effectively tune the band position/structure of VBM and CBM.

2. **The band gap** ($E_g$) The VB of BiOBr and/or BiOI is composed of O $2p$ and

X $np$ hybrid orbital, and the contribution of X $np$ (Br $5p$ and I $6p$ here) is negligible in the CB, but prominent in the VB. There has always been an implicit contradiction between the visible-light absorption and the adequate redox capability.[180] In this case, formation of solid solutions with tuneable valence band and conduction band position, however relatively narrow the band gap, possessing excellent photocatalytic activity is one feasible approach to compromise the contradiction. The substitution of Br in BiOBr lattice by I reduces the band gap energy by around 1.0 eV; thus $BiOBr_xI_{1-x}$ harnesses more visible-light than BiOBr.

3. **The I content** (Hybridisation of orbitals in pure semiconductors) Jia *et al.* demonstrated that the I-containing $BiOBr_xI_{1-x}$ samples exhibited higher photocatalytic activity than pure BiOBr. The halogen materials are influenced by the hybridization of orbital, therefore the bonding orbitals are lowered in energy due to the hybridisation of $p-$ and $s-$ orbitals.[165] Here in this $BiOBr_xI_{1-x}$ solid solution system, the I concentration is also one of the important factors that affect the photocatalytic performance of the solid solutions. However, since BiOI shows little visible-light-responsive activity, there is a critical Br/I molar ratio ($n_{Br}/n_I = 1$) that the effects of VB/CB modification and band gap narrowing surpasses other factors (i.e. the surface area and the morphology), leading to the superior photocatalytic activity of the solid solutions $BiOxBr_xI_{1-x}$ compared to BiOBr.

## 7.5 Conclusions

A series of $BiOBr_xI_{1-x}$ solid solutions with controlled band structure have been successfully synthesised by an effective one-step ultrasonification method. The variation of composition in the $BiOBr_xI_{1-x}$ solid solutions causes changes in the light absorption ability associated with the changes in the band gap energies. XPS displayed a small shift towards lower binding energy in the valance band consistent with the substitution of I onto Br sites, which is correlated with the gradual changes in optical absorption of $BiOBr_xI_{1-x}$ samples. The inducing of iodine may change the composition of the valence band from O $2p$ and Br $4p$ into O $2p$, Br $4p$ and I $5p$, which could influence the photocatalytic activity synergistically. Among all the samples, the as-synthesised $BiOBr_{0.75}I_{0.25}$ possessed the best activity under visible-light irradiation. Based on the estimation of valence band and conduction band position, the inducing of iodine with lower electronegativity into the BiOBr system lays the key role in tuning the band level and also the optical property of the $BiOBr_xI_{1-x}$ solid solutions.

# Chapter 8

# Summary and future work

## 8.1 BiOBr-based photocatalysts: Current perspectives

This section intends to provide an overview of the main system based on bismuth oxyhalides photocatalysts and ideas already analysed throughout the thesis; in addition future perspectives will be mentioned on the basis of systems and/or ideas currently being explored. Differs from the conventional $TiO_2$-based systems, this area has not been significantly presented, however endows it with great potential as it has relatively narrower band gap and meanwhile excellent stability can be achieved.

Generally a semiconductor can be excited by light energy higher than its $E_g$ which results in the formation of electron-hole pairs. The term photocatalysis is commonly referred to any chemical process catalysed by a solid where the external source is an electromagnetic field with wave numbers in the UV-visible-infrared range. The photocatalysts that used are usually solid semiconductors which are able

to absorb visible and/or UV light, with good stability, inexpensive and nontoxic. These semiconductors $TiO_2$, ZnO, $Bi_2S_3$, CdS and ZnS can all act as photoactive materials for redox/charge-transfer processes due to their electronic structures which are characterised by a filled valence band and an empty conduction band.

Bismuth oxyhalides (BiOX, X=Cl, Br, I) have been studied extensively because of their unique properties and potential applications in catalysis, environmental-friendly pigments, cosmetics and nanosensors. All of the BiOX compounds crystallise in the tetragonal matlockite structure, a layer structure which is characterised by $[Bi_2O_2]$ slabs interleaved by double slabs of halogen atoms. These oxyhalide compounds have been utilised as effective photocatalysts in a variety of oxidation reactions such as decomposition of organic dyes, nitric oxide, refractory organic pollutants, and water splitting. It is interesting that all three bismuth oxyhalides have different band gap energy: Bismuth oxychloride (BiOCl) is an off-white semiconductor with a band gap energy between 3.19 eV and 3.44 eV, it is also one of the simplest members of the Sillén family expressed by $[M_2O_2][Cl_m]$ or $[M_3O_{4+n}][Cl_m]$ (m=1-3) where bismuth oxide-based fluorite-like layers, $[M_2O_2]$ or $[M_3O_{4+n}]$, are intergrown with double chlorine layers. Bismuth oxybromide (BiOBr) is a light yellow material with a slightly smaller band gap energy of 2.64 eV due to the hybridisation between the O $2p$ and Bi $6s$ states which can narrow the band gap; the layered structure constructed by the combination of a bromine ion layer and a metal-oxygen (Bi-O) layer endows BiOBr with a high carrier mobility and a small probability of the recombination of photo-generated electrons and holes in the materials. BiOI has the smallest band gap energy between 1.77 eV and 1.92 eV with the colour of brick red. Depending on the band gap energy the three materials exhibit different optical property and catalytic reactivity.

In *Chapter* 3, ultrasound-assisted synthetic methodology is used to obtain the specific flower-like BiOBr materials without the involvement of organic constituents. The nano-sized flower-like materials exhibit both excellent photocatalytic activity and stability under visible-light irradiation. The mechanism for the ultrasound-induced orientational assembly of the special architectures is proposed based on SEM/TEM analysis, which may provide insights into the potential role of sonification in the application of crystals with highly reactive surfaces.

In *Chapter* 4, the combination of n-type semiconductor AgBr and p-type semiconductor BiOBr generates the AgBr-BiOBr p-n heterojunction with various AgBr loading amounts. It is clearly observed that AgBr heterojunctions with lower AgBr loading possess superior photocatalytic activities comparing to pure BiOBr. Isolated AgBr species in the AgBr-BiOBr heterojunctions with higher AgBr loadings may result in reduced photocatalytic activity. Nevertheless, these AgBr-BiOBr materials gradually deactivate under long-term visible-light irradiation since AgBr is unstable and transforms into $Ag_2O$ upon light irradiation. The as-generated $Ag_2O$ might mask the light excitation, and also serve as recombination centers.

In *Chapter* 5, another p-n heterojunction system, BiOBr-$ZnFe_2O_4$ is discussed and this heterostructure exhibits excellent stability under visible-light irradiation; with a simple ultrasound-assisted, precipitation-deposition method, the micro-spherical morphology is found in the BiOBr-$ZnFe_2O_4$ heterojunctions with appropriate molar ratio of the constituents. This heterojunction not only successfully improves the photocatalytic performance of the photocatalyst materials, but also the stability under long-term visible-light irradiation.

In *Chapter*6, the concept of surface plasmon resonance on the interface of metallic

nano-particles and semiconductors is introduced and discussed. Ag-modification on the surface of BiOBr may affect the optical property, structure and photocatalytic performance of the pure semiconductor.

In *Chapter* 7, a continuous series of solid solution $BiOBr_xI_{1-x}$ photocatalysts with tunable band positions are synthesised by ultrasound method. The photocatalysts exhibit different photocatalytic activity depending on the molar ratio of the constituents. The formation of solid solution affects the optical property, crystal structure, and electronic band structure of the materials comparing to the pure semiconductor.

## 8.2 Future work

### 8.2.1 The quest for novel composite materials

As summerised in previous chapters, composite materials are typically aimed at improving photocatalytic activity through adequate controlling of the electronic, particularly the optical and/or chemical properties. The optoelectronic properties of the materials are significantly related to band gap engineering, i.e., controlling light absorption, as well as the recombination rate of charge carriers after light excitation. The chemical properties are usually used to enhance the reaction through adequate absorption and/or desorption and activation of the reactant species. Modifications in electronic and chemical/composition engineering would consider the optimisation of both the major aspects concerning any photocatalytic reactions.

### 8.2.2 Present and forthcoming ideas of developing semiconductor photocatalysts

The concept of photoelectrochemistry has been investigated for decades and the extension of the principles of these photoelectrochemical cells to the design of semiconductor electrodes systems for carrying out visible-light-driven photochemical reactions is still under discussion. Currently the fate of the photo-generated charge carriers ($e^- - h^+$) is still under investigation by various characterisation techniques, and attempts are being made to figure out the working mechanism and explore more stable p-n heterojunctions.

#### 8.2.2.1 Photoelectrochemical (PEC) water cleavage by visible-light

Ever since Fujishima and Honda discovered the photoelectrochemical (PEC) water splitting using a $TiO_2$ electrodes in 1972, significant attention has been paid to the study of semiconductor photoelectrodes in order to split water under both UV and visible-light irradiation. However, the development of oxide semiconductor photocatalysts is stuck in between the sufficiently negative conduction band for $H_2$ production and a relatively narrow band gap (i.e. $< 3.0\,\text{eV}$) for visible-light absorption.

The major advantages of photoelectrochemical devices are the great ease with which the semiconductor-electrolyte junction is formed, and also the thin, polycrystalline, semiconductor films can be used without serious loss of conversion efficiency compared to single crystal semiconductors.[185] Despite the fact that significant advances have been made both in the basic understanding of photoelectrochemical devices and in the development of systems with good conversion efficiency and stability, additional research must be done before photoelectrochemical systems can be

seriously considered for practical solar energy conversion schemes.

#### 8.2.2.2 Z-scheme photocatalysis: What we could learn from the nature?

A system consisting of two photocatalytic reactions which connected with a redox mediator is called a 'Z-scheme' reaction system and this system has been employed mainly for water splitting under visible-light irradiation. The term 'Z-scheme' originates from its shape as shown in Figure 8.1 A, which has been used to interpret the mechanism of photosynthesis by plants in which two chlorophyll molecules, P700 and P680. By mimicking photosynthesis process, it is possible to manipulate 'Z-scheme' which can be utilised in the application of photocatalysis. As shown in Figure 8.1 B, a photocatalyst included in the part 'R' reduces an oxidant (which is known as 'objective reduction', such as hydrogen production from water) and oxidises the redox mediator 'M', while the part 'O' oxidises a reductant (which is 'objective oxidation', i.e., oxygen production from water) and reduces M. A significant advantage of this Z-scheme system is to loosen the requirement of electronic structure of photocatalysts; a photocatalyst in part 'O' is needed to drive an objective oxidation by $h^+$, but not an objective reduction by $e^+$, and a photocatalyst in part 'R' is needed to drive an objective reduction by $e^-$, but not an objective oxidation by $h^+$. The standard electrode potential of redox mediator should lie between a CB bottom of part 'O' and a VB top of part 'R'. Therefore, photocatalysts of relatively narrow band gap, corresponding to photoabsorption of longer wavelength, can be used.[33]

This Z-scheme system still requires inhibitions of unfavourable $e^-$ and $h^+$ transfer processes which induce 'short circuiting' of photo-generated charge. Furthermore, there are still some problems in ordinary single-photocatalyst systems, which might

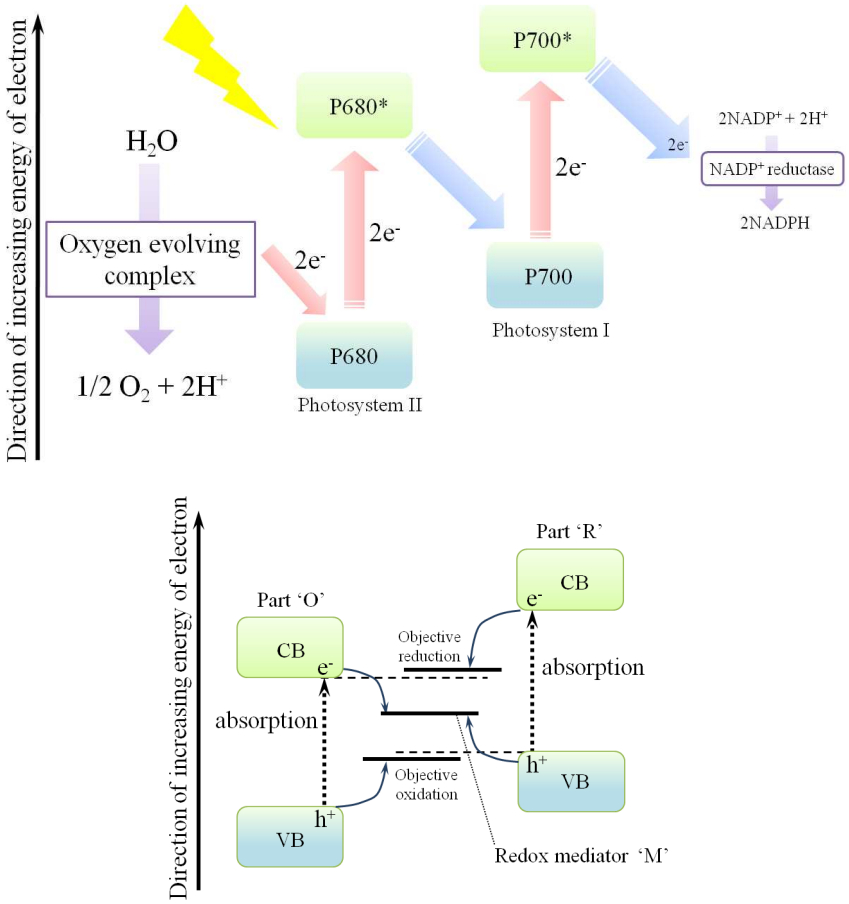


Figure 8.1: (A) A Z-scheme diagram of photosynthesis and (B) a Z-scheme reaction combining two semiconductor photocatalytic reaction parts ('R' and 'O') with a redox mediator 'M'.[23]

be the reason why it is necessary to explore Z-scheme photocatalytic water splitting system with the combination of different photocatalysts.

#### 8.2.2.3 Photo-reduction of $CO_2$

Greenhouse gas such as $CO_2$ is the primary cause of global warming. One of the best routes to remedy $CO_2$ without producing more $CO_2$ is to transform it into higher order hydrocarbons. From the thermodynamic point of view, single electron reduction of $CO_2$ to $CO_2^{\cdot-}$ radical occurs at $E^0 = -1.90\,\text{eV}$ versus NHE at pH=7 in an aqueous solution at temperature of $25^0$C under 1 atmosphere gas pressure. $CO_2$ is extremely stable and the $CO_2$ reduction process is highly endothermic, therefore, sustainable $CO_2$ utilisation is scientifically challenging, which requires appropriate catalysts and more importantly, it is possible only if renewable energy such as solar is used as the energy source.

The reduction of redox species happens at less negative potential on illuminated p-type semiconductor compared to metal electrode due to the band bending at semiconductor/liquid interface. Therefore, it is feasible to photo-reduce $CO_2$ on p-type semiconductors.[28] However, the overall $CO_2$ photo-reduction rate is extremely low, which leads to significant over-potential for $CO_2$ reduction on the surface of these materials. Different approach for photo-reduction of $CO_2$ involves photosensitiser and sacrificial electron donors, in which process sacrificial donors such as noble metals are consumed during the reduction process and photosensitisers degrade under long exposure to illumination. It might be possible to combine Bismuth oxyhalides with another p-type semiconductor, such as GaAs or GaP to realise both the photo-reduction of $CO_2$ with reasonable reaction rate.

# Bibliography

[1] Z Jiang, T Xiao, VL Kuznetsov, and PP Edwards. Turning carbon dioxide into fuel. *Philosophical Transactions of the Royal Society A: Mathematical, Physical and Engineering Sciences*, 368(1923):3343–64, July 2010.

[2] Donghua Pei and Jingfei Luan. Development of visible light-responsive sensitized photocatalysts. *International Journal of Photoenergy*, 2012:1–13, 2012.

[3] I-H Tseng, W-C Chang, and JCS Wu. Photoreduction of $CO_2$ using sol-gel derived titania and titania-supported copper catalysts. *Applied Catalysis B: Environmental*, 37(1):37–48, April 2002.

[4] M Aresta and A Dibenedetto. Utilisation of $CO_2$ as a chemical feedstock: opportunities and challenges. *Dalton Transactions*, (28):2975–2992, 2007.

[5] S Kuwabata, K Nishida, and R Tsuda. Photochemical reduction of carbon dioxide to methanol using ZnS microcrystallite as a photocatalyst in the presence of methanol dehydrogenase. *Journal of the Electrochemical Society*, 141(6):1498–1503, 1994.

[6] N Luo, Z Jiang, H Shi, F Cao, T Xiao, and PP Edwards. Photo-catalytic con-

version of oxygenated hydrocarbons to hydrogen over heteroatom-doped $TiO_2$ catalysts. *International Journal of Hydrogen Energy*, 34(1):125–129, 2009.

[7] H Zhou, X Li, T Fan, FE Osterloh, J Ding, EM Sabio, D Zhang, and Q Guo. Artificial inorganic leafs for efficient photochemical hydrogen production inspired by natural photosynthesis. *Advanced Materials*, 22(9):951–956, 2010.

[8] X Chen, S Shen, L Guo, and SS Mao. Semiconductor-based photocatalytic hydrogen generation. *Chemical Reviews*, 110(11):6503–70, November 2010.

[9] M Bowker. Sustainable hydrogen production by the application of ambient temperature photocatalysis. *Green Chemistry*, 13(9):2235, 2011.

[10] CX Kronawitter, L Vayssieres, S Shen, L Guo, D Wheeler, JZ Zhang, BR Antoun, and SS Mao. A perspective on solar-driven water splitting with all-oxide hetero-nanostructures. *Energy & Environmental Science*, 4(10):3889, 2011.

[11] Y Lin, G Yuan, R Liu, S Zhou, SW Sheehan, and D Wang. Semiconductor nanostructure-based photoelectrochemical water splitting: a brief review. *Chemical Physics Letters*, 507(4-6):209–215, May 2011.

[12] J Su, L Guo, N Bao, and C Grimes. Nanostructured $WO_3/BiVO_4$ heterojunction films for efficient photoelectrochemical water splitting. *Nano Letters*, 11(5):1928–33, May 2011.

[13] SY Yang, J Seidel, SJ Byrnes, P Shafer, C-H Yang, M Rossell, P Yu, Y-H Chu, J Scott, JW Ager, L Martin, and R Ramesh. Above-bandgap voltages from ferroelectric photovoltaic devices. *Nature Nanotechnology*, 5(2):143–147, February 2010.

[14] T Bond, S Doherty, D Fahey, P Forster, T Berntsen, B DeAngelo, M Flanner, S Ghan, B Kärcher, D Koch, S Kinne, Y Kondo, P Quinn, M Sarofim, MG Schultz, M Schulz, C Venkataraman, H Zhang, S Zhang, N Bellouin, SK Guttikunda, PK Hopke, M Jacobson, J Kaiser, Z Klimont, U Lohmann, J Schwarz, D Shindell, T Storelvmo, S Warren, and C Zender. Bounding the role of black carbon in the climate system: A scientific assessment. *Journal of Geophysical Research: Atmospheres*, pages n/a–n/a, 2013.

[15] Z Ai, W Ho, S Lee, and L Zhang. Efficient photocatalytic removal of NO in indoor air with hierarchical bismuth oxybromide nanoplate microspheres under visible light. *Environmental Science & Technology*, 43(11):4143–50, June 2009.

[16] A Di Paola, E García-López, Gi Marcì, and L Palmisano. A survey of photocatalytic materials for environmental remediation. *Journal of Hazardous Materials*, 211-212:3–29, April 2012.

[17] M Graetzel. *Energy resources through photochemistry and catalysis*. 1983.

[18] M Grätzel. Photoelectrochemical cells. *Nature*, 414(November):338–344, 2001.

[19] S Lou, X Guo, T Fan, and D Zhang. Butterflies: inspiration for solar cells and sunlight water-splitting catalysts. *Energy & Environmental Science*, 5(11):9195, 2012.

[20] BA Gregg. Excitonic solar cells. *The Journal of Physical Chemistry B*, 107:4688–4698, 2003.

[21] HI de Lasa and B Serrano Rosales. Preface. In Hugo I de Lasa Engineering and Benito Serrano Rosales B T Advances in Chemical, editors, *Advances in*

*Chemical Engineering Photocatalytic Technologies*, volume Volume 36, pages ix–x. Academic Press, 2009.

[22] J Zhao, C Chen, and W Ma. Photocatalytic degradation of organic pollutants under visible light irradiation. *Topics in Catalysis*, 35(3-4):269–278, July 2005.

[23] R Abe. Recent progress on photocatalytic and photoelectrochemical water splitting under visible light irradiation. *Journal of Photochemistry and Photobiology C: Photochemistry Reviews*, 11(4):179–209, December 2010.

[24] MM Halmann. *Photodegradation of Water Pollutants*. CRC Press, 1996.

[25] JM Herrmann. Heterogeneous photocatalysis: fundamentals and applications to the removal of various types of aqueous pollutants. *Catalysis Today*, 53(1):115–129, October 1999.

[26] M Schiavello. Photocatalysis and environment: trends and applications. 1988.

[27] C Prat, M Vicente, and S Esplugas. Treatment of bleaching waters in the paper industry by hydrogen peroxide and ultraviolet radiation. *Water Research*, 22(6):663–668, 1988.

[28] A Fujishima and TN Rao. Interfacial photochemistry: fundamentals and applications. *Pure and applied chemistry*, 70(11):2177–2187, 1998.

[29] E Heinzle, F Geiger, M Fahmy, and OM Kut. Integrated ozonation-biotreatment of pulp bleaching effluents containing chlorinated phenolic compounds. *Biotechnology Progress*, (1990):67–77, 1992.

[30] M Schiavello. *Heterogeneous photocatalysis*, volume 93. January 1993.

[31] S Sakthivel, B Neppolian, MV Shankar, B Arabindoo, M Palanichamy, and V Murugesan. Solar photocatalytic degradation of azo dye: comparison of photocatalytic efficiency of ZnO and $TiO_2$. *Solar Energy Materials*, 77(3):65–82, 2003.

[32] K Rajeshwar and JG Ibanez. *Environmental electrochemistry: Fundamentals and applications in pollution sensors and abatement*. 1997.

[33] A Kudo, H Kato, and I Tsuji. Strategies for the development of visible-light-driven photocatalysts for water splitting. *Chemistry Letters*, 33(12):1534–1539, 2004.

[34] A Kudo and Y Miseki. Heterogeneous photocatalyst materials for water splitting. *Chemical Society Reviews*, 38(1):253–78, January 2009.

[35] JH Pan, H Dou, Z Xiong, C Xu, J Ma, and XS Zhao. Porous photocatalysts for advanced water purifications. *Journal of Materials Chemistry*, 20(22):4512–4528, 2010.

[36] A Fujishima and K Honda. Electrochemical photolysis of water at a semiconductor electrode. *Nature*, 238:37, 1972.

[37] A Kubacka, M Fernández-García, and G Colón. Advanced nanoarchitectures for solar photocatalytic applications. *Chemical Reviews*, 112(3):1555–614, March 2012.

[38] M Litter. Heterogeneous photocatalysis: transition metal ions in photocatalytic systems. *Applied Catalysis B: Environmental*, 23(2-3):89–114, November 1999.

[39] K Maeda, T Takata, M Hara, N Saito, Y Inoue, H Kobayashi, and K Domen. GaN:ZnO solid solution as a photocatalyst for visible-light-driven overall water splitting. *Journal of the American Chemical Society*, 127(23):8286–7, June 2005.

[40] S Trasatti. Work function, electronegativity, and electrochemical behaviour of metals: III. Electrolytic hydrogen evolution in acid solutions. *Electroanalytical Chemistry and Interfacial Electrochemistry*, 39:163–184, 1972.

[41] VY Gurevich and YY Pleskov. Semiconductor Photoelectrochemistry, May 1988.

[42] MD Hernández-Alonso, F Fresno, S Suárez, and JM Coronado. Development of alternative photocatalysts to $TiO_2$: challenges and opportunities. *Energy & Environmental Science*, 2(12):1231, 2009.

[43] B E A Saleh and M C Teich. *Chapter 15. Photons in semiconductors.* Wiley Series in Pure and Applied Optics. Wiley, 2013.

[44] C Priester and D Bertho. Band-offset determination at strained II-VI heterojunctions within a self-consistent tight-binding model. *Physica B: Condensed Matter*, 191:1–15, 1993.

[45] HP Maruska and AK Ghosh. Photocatalytic decomposition of water at semiconductor electrodes. *Solar Energy*, 20(6):443–458, January 1978.

[46] CG Van de Walle and J Neugebauer. Universal alignment of hydrogen levels in semiconductors, insulators and solutions. *Nature*, 423(6940):626–8, June 2003.

[47] A Bard. Design of semiconductor photoelectrochemical systems for solar energy conversion. *Journal of Physical Chemistry*, 86:172–177, 1982.

[48] Yong X and MAA Schoonen. The absolute energy positions of conduction and valence bands of selected semiconducting minerals. *American Mineralogist*, 85:543–556, 2000.

[49] M Grätzel. Dye-sensitized solar cells. *Journal of Photochemistry and Photobiology C: Photochemistry Reviews*, 4(2):145–153, October 2003.

[50] L-R Hou, C-Z Yuan, and Y Peng. Preparation and photocatalytic property of sunlight-driven photocatalyst $Bi_38ZnO_58$. *Journal of Molecular Catalysis A: Chemical*, 252(1-2):132–135, June 2006.

[51] J Tang and J Ye. Photocatalytic and photophysical properties of visible-light-driven photocatalyst $ZnBi_{12}O_{20}$. *Chemical Physics Letters*, 410(1-3):104–107, 2005.

[52] JM Herrmann, H Tahiri, and Y Ait-Ichou. Characterization and photocatalytic activity in aqueous medium of $TiO_2$ and Ag-$TiO_2$ coatings on quartz. *Applied Catalysis B: Environmental*, 13:219–228, 1997.

[53] MA Butler. Photoelectrolysis and physical properties of the semiconducting electrode $WO_3$. *Journal of Applied Physics*, 48(5):1914–1920, 1977.

[54] F Han, VSR Kambala, M Srinivasan, D Rajarathnam, and R Naidu. Tailored titanium dioxide photocatalysts for the degradation of organic dyes in wastewater treatment: a review. *Applied Catalysis A: General*, 359(1-2):25–40, May 2009.

[55] O Moutanabbir and U Gösele. *Heterogeneous Integration of Compound Semiconductors*, volume 40. June 2010.

[56] Y Gassenbauer and A Klein. Electronic and chemical properties of tin-doped indium oxide (ITO) surfaces and ITO/ZnPc interfaces studied in-situ by photoelectron spectroscopy. *The Journal of Physical Chemistry B*, 110(10):4793–801, March 2006.

[57] SH Cheung, P Nachimuthu, AG Joly, MH Engelhard, MK Bowman, and SA Chambers. N incorporation and electronic structure in N-doped $TiO_2$ rutile. *Surface Science*, 601(7):1754–1762, 2007.

[58] BC O'Regan and F Lenzmann. Charge transport and recombination in a nanoscale interpenetrating network of n-type and p-type semiconductors: transient photocurrent and photovoltage studies of $TiO_2$ /Dye/CuSCN photovoltaic cells. *The Journal of Physical Chemistry B*, 108:4342–4350, 2004.

[59] K Maeda. Photocatalytic water splitting using semiconductor particles: history and recent developments. *Journal of Photochemistry and Photobiology C: Photochemistry Reviews*, 12(4):237–268, December 2011.

[60] DJ Norris, AL Efros, and SC Erwin. Doped nanocrystals. *Science (New York, N.Y.)*, 319(5871):1776–9, March 2008.

[61] N Pradhan and DD Sarma. Advances in light-emitting doped semiconductor nanocrystals. *The Journal of Physical Chemistry Letters*, pages 2818–2826, 2011.

[62] S Rehman, R Ullah, M Butt, and ND Gohar. Strategies of making $TiO_2$ and ZnO visible light active. *Journal of hazardous materials*, 170(2-3):560–9, October 2009.

[63] M Bellardita, M Addamo, A Di Paola, L Palmisano, and A M Venezia. Preparation of N-doped $TiO_2$: characterization and photocatalytic performance under UV and visible light. *Physical Chemistry Chemical Physics*, 11(20):4084–4093, 2009.

[64] Y Bessekhouad, D Robert, and J V Weber. $Bi_2S_3/TiO_2$ and $CdS/TiO_2$ heterojunctions as an available configuration for photocatalytic degradation of organic pollutant. *Journal of Photochemistry and Photobiology A: Chemistry*, 163(3):569–580, May 2004.

[65] L Wu, J C Yu, and X Fu. Characterization and photocatalytic mechanism of nanosized CdS coupled $TiO_2$ nanocrystals under visible light irradiation. *Journal of Molecular Catalysis A: Chemical*, 244(1-2):25–32, February 2006.

[66] W Ho and J C Yu. Sonochemical synthesis and visible light photocatalytic behavior of CdSe and $CdSe/TiO_2$ nanoparticles. *Journal of Molecular Catalysis A: Chemical*, 247(1-2):268–274, March 2006.

[67] L Zhang, W Wang, J Yang, Z Chen, W Zhang, L Zhou, and S Liu. Sonochemical synthesis of nanocrystallite $Bi_2O_3$ as a visible-light-driven photocatalyst. *Applied Catalysis A: General*, 308(0):105–110, July 2006.

[68] J Henle and S Kaskel. Preparation of photochromic transparent BiOX (X = Cl,

I)/PLA nanocomposite materials via microemulsion polymerization. *Journal of Materials Chemistry*, 17(47):4964, 2007.

[69] J Henle, P Simon, A Frenzel, S Scholz, and S Kaskel. Nanosized BiOX (X = Cl, Br, I) particles synthesized in reverse microemulsions. *Chemistry of Materials*, 19(3):366–373, February 2007.

[70] E Keller and V Kramer. A strong deviation from Vegard's rule: x-ray powder investigations of the three quasi-binary phase systems BiOX-BiOY (X, Y= Cl, Br, I). *ZEITSCHRIFT FUR NATURFORSCHUNG B*, 60b:1255–1263, 2005.

[71] Z Deng, D Chen, B Peng, and F Tang. From bulk metal Bi to two-dimensional well-crystallized BiOX (X = Cl, Br) micro- and nanostructures: synthesis and characterization. *Crystal Growth & Design*, 8(8):2995–3003, August 2008.

[72] Y Liu, W-J Son, J Lu, B Huang, Y Dai, and M-H Whangbo. Composition dependence of the photocatalytic activities of $BiOCl_{1-x}Br_x$ solid solutions under visible light. *Chemistry - A European Journal*, 17(34):9342–9, August 2011.

[73] Y Lei, G Wang, S Song, W Fan, and H Zhang. Synthesis, characterization and assembly of BiOCl nanostructure and their photocatalytic properties. *CrystEngComm*, 11(9):1857–1862, 2009.

[74] K-L Zhang, C-M Liu, F-Q Huang, C Zheng, and W-D Wang. Study of the electronic structure and photocatalytic activity of the BiOCl photocatalyst. *Applied Catalysis B: Environmental*, 68(3-4):125–129, 2006.

[75] B Pare, B Sarwan, and SB Jonnalagadda. The characteristics and photocat-

alytic activities of BiOCl as highly efficient photocatalyst. *Journal of Molecular Structure*, 1007:196–202, January 2012.

[76] S Sun, W Wang, L Zhang, L Zhou, W Yin, and M Shang. Visible light-induced efficient contaminant removal by $Bi_5O_7I$. *Environmental Science & Technology*, 43(6):2005–10, March 2009.

[77] Lijun Zhao, Xiaochao Zhang, Caimei Fan, Zhenhai Liang, and Peide Han. First-principles study on the structural, electronic and optical properties of BiOX (X=Cl, Br, I) crystals. *Physica B: Condensed Matter*, 407(17):3364–3370, September 2012.

[78] MA Gondal, X Chang, MA Ali, ZH Yamani, Q Zhou, and G Ji. Adsorption and degradation performance of Rhodamine B over BiOBr under monochromatic 532 nm pulsed laser exposure. *Applied Catalysis A: General*, 397(1-2):192–200, April 2011.

[79] M Shang, W Wang, and L Zhang. Preparation of BiOBr lamellar structure with high photocatalytic activity by CTAB as Br source and template. *Journal of Hazardous Materials*, 167(1-3):803–9, August 2009.

[80] L Zhang, X-F Cao, X-T Chen, and ZL Xue. BiOBr hierarchical microspheres: microwave-assisted solvothermal synthesis, strong adsorption and excellent photocatalytic properties. *Journal of colloid and interface science*, 354(2):630–6, February 2011.

[81] Z Jiang, F Yang, G Yang, L Kong, MO Jones, T Xiao, and PP Edwards. The hydrothermal synthesis of BiOBr flakes for visible-light-responsive photocat-

alytic degradation of methyl orange. *Journal of Photochemistry and Photobiology A: Chemistry*, 212(1):8–13, April 2010.

[82] C Sun, C Chen, W Ma, and J Zhao. Photodegradation of organic pollutants catalyzed by iron species under visible light irradiation. *Physical chemistry chemical physics : PCCP*, 13(6):1957–69, February 2011.

[83] S Choudhary, S Upadhyay, P Kumar, N Singh, VR Satsangi, R Shrivastav, and S Dass. Nanostructured bilayered thin films in photoelectrochemical water splitting-a review. *International Journal of Hydrogen Energy*, 37(24):18713–18730, December 2012.

[84] Y Nosaka, K Norimatsu, and H Miyama. The function of metals in metal-compounded semiconductor photocatalysts. *Chemical Physics Letters*, 106(1):128–131, 1984.

[85] FE Osterloh. Inorganic materials as catalysts for photochemical splitting of water. *Chemistry of Materials*, 20(1):35–54, January 2008.

[86] H Yamashita, Y Fujii, Y Ichihashi, and SG Zhang. Selective formation of $CH_3OH$ in the photocatalytic reduction of $CO_2$ with $H_2O$ on titanium oxides highly dispersed within zeolites and mesoporous molecular sieves. *Catalysis Today*, 45:221–227, 1998.

[87] I-H Tseng, JCS Wu, and H-Y Chou. Effects of sol-gel procedures on the photocatalysis of $Cu/TiO_2$ in $CO_2$ photoreduction. *Journal of Catalysis*, 221(2):432–440, January 2004.

[88] P Atkins, T Overton, J Rourke, M Weller, and F Armstrong. *Shriver Atkins Inorganic Chemistry*. Oxford University Press, New York, 2006.

[89] EN Kaufmann. *X-ray Characterization of Materials*. 2008.

[90] DA Skoog, JF Holler, and SR Crouch. *Principles of Instrumental Analysis*, volume 152. January 1983.

[91] EN Kaufmann. *Characterization of Materials Volume 2*. 2003.

[92] JF Moulder, WF Stickle, PE Sobol, and KD Bomben. *Handbook of X-ray Photoelectron Spectroscopy*, volume Perkin Elm. 1992.

[93] D Briggs. Handbook of X-ray Photoelectron Spectroscopy. *Surface and Interface Analysis*, 3(4):v–v, 1981.

[94] G Beamson and D Briggs. Performance and application of the Scienta ESCA300 spectrometer. *Surface and Interface Analysis*, 15(May):541–549, 1990.

[95] JW Childers, R Roehl, and R Palmer. Direct comparison of the capabilities of photoacoustic and diffuse reflectance spectroscopies in the ultraviolet, visible, and near-infrared regions. *Analytical Chemistry*, 58(13):2629–2636, November 1986.

[96] LS Clesceri, AE Greenberg, and AD Eaton. *Standard methods for the examination of water & wastewater*. 2005.

[97] G Cornelissen, Ö Gustafsson, TD Bucheli, MTO Jonker, AA Koelmans, and PCM van Noort. Extensive sorption of organic compounds to black carbon,

coal, and kerogen in sediments and soils: mechanisms and consequences for distribution, bioaccumulation, and biodegradation. *Environmental Science & Technology*, 39(18):6881–6895, August 2005.

[98] L Kong, Z Jiang, T Xiao, L Lu, MO Jones, and PP Edwards. Exceptional visible-light-driven photocatalytic activity over BiOBr-$ZnFe_2O_4$ heterojunctions. *Chemical Communications*, 47(19):5512–4, May 2011.

[99] YS Nam, AP Magyar, D Lee, JW Kim, DS Yun, H Park, TS Pollom, DA Weitz, and AM Belcher. Biologically templated photocatalytic nanostructures for sustained light-driven water oxidation. *Nature Nanotechnology*, 5(5):340–344, 2010.

[100] W Li, Y Deng, Z Wu, and X Qian. Hydrothermal etching assisted crystallization: A facile route to functional yolk-shell titanate microspheres with ultrathin nanosheets-assembled double shells. *Journal of the American Chemical Society*, pages 15830–15833, 2011.

[101] C George, D Dorfs, G Bertoni, A Falqui, A Genovese, T Pellegrino, A Roig, A Quarta, R Comparelli, ML Curri, R Cingolani, and L Manna. A cast-mold approach to iron oxide and Pt/Iron oxide nanocontainers and nanoparticles with a reactive concave surface. *Journal of the American Chemical Society*, 133(7):2205–2217, 2011.

[102] GM Whitesides and B Grzybowski. Self-assembly at all scales. *Science (New York, N.Y.)*, 295(5564):2418–21, March 2002.

[103] Y Min, M Akbulut, K Kristiansen, Y Golan, and J Israelachvili. The role of

interparticle and external forces in nanoparticle assembly. *Nature Materials*, 7(7):527–538, 2008.

[104] M Niederberger and H Colfen. Oriented attachment and mesocrystals: Non-classical crystallization mechanisms based on nanoparticle assembly. *Physical chemistry chemical physics : PCCP*, 8(28):3271–3287, 2006.

[105] KJ Stebe, E Lewandowski, and M Ghosh. Oriented assembly of metamaterials. *Science (New York, N.Y.)*, 325(5937):159–60, July 2009.

[106] E Pouget, E Dujardin, A Cavalier, A Moreac, C Valery, V Marchi-Artzner, T Weiss, A Renault, M Paternostre, and F Artzner. Hierarchical architectures by synergy between dynamical template self-assembly and biomineralization. *Nature Materials*, 6(6):434–439, 2007.

[107] JH Pan, Z Cai, Y Yu, and XS Zhao. Controllable synthesis of mesoporous F-$TiO_2$ spheres for effective photocatalysis. *Journal of Materials Chemistry*, 21(30):11430, 2011.

[108] A Ahniyaz, Y Sakamoto, and L Bergström. Magnetic field-induced assembly of oriented superlattices from maghemite nanocubes. *P. Natl. Acad. Sci.*, 104(45):17570–17574, 2007.

[109] A Snezhko and IS Aranson. Magnetic manipulation of self-assembled colloidal asters. *Nature Materials*, 10(9):698–703, 2011.

[110] MD Morariu, NE Voicu, E Schäffer, Z Lin, TP Russell, and U Steiner. Hierarchical structure formation and pattern replication induced by an electric field. *Nature materials*, 2(1):48–52, January 2003.

[111] Y Huang, X Duan, Q Wei, and C M Lieber. Directed assembly of one-dimensional nanostructures into functional networks. *Science (New York, N.Y.)*, 291(5504):630–3, January 2001.

[112] S Mann. Self-assembly and transformation of hybrid nano-objects and nanostructures under equilibrium and non-equilibrium conditions. *Nature Materials*, 8(10):781–792, 2009.

[113] J Zhang, F Shi, J Lin, D Chen, J Gao, Z Huang, X Ding, and C Tang. Self-assembled 3-D architectures of BiOBr as a visible light-driven photocatalyst. *Chemistry of Materials*, 20(9):2937–2941, May 2008.

[114] Y Huo, J Zhang, M Miao, and Y Jin. Solvothermal synthesis of flower-like BiOBr microspheres with highly visible-light photocatalytic performances. *Applied Catalysis B: Environmental*, 111-112:334–341, January 2012.

[115] Y Feng, L Li, J Li, J Wang, and L Liu. Synthesis of mesoporous BiOBr 3D microspheres and their photodecomposition for toluene. *Journal of Hazardous Materials*, 192(2):538–44, August 2011.

[116] X Zhang, Z Ai, F Jia, and L Zhang. Generalized one-pot synthesis, characterization, and photocatalytic activity of hierarchical BiOX (X=Cl, Br, I) nanoplate microspheres. *Journal of Physical Chemistry C*, 112(3):747–753, January 2008.

[117] JM Patete, X Peng, C Koenigsmann, Y Xu, B Karn, and SS Wong. Viable methodologies for the synthesis of high-quality nanostructures. *Green Chemistry*, 13(3):482–519, 2011.

[118] NA Dhas and KS Suslick. Sonochemical preparation of hollow nanospheres and hollow nanocrystals. *Journal of the American Chemical Society*, 127(8):2368–2369, 2005.

[119] J. Bang and K. Suslick. Applications of ultrasound to the synthesis of nanostructured materials. *Advanced Materials*, 22(10):1039–1059, 2010.

[120] S H Jung, E Oh, K H Lee, W Park, and S H Jeong. A sonochemical method for fabricating aligned ZnO nanorods. *Advanced Materials*, 19(5):749–753, 2007.

[121] DG Shchukin, E Skorb, V Belova, and H Möhwald. Ultrasonic cavitation at solid surfaces. *Advanced Materials*, 23(17):1922–1934, 2011.

[122] K Yu, H He, C Gu, and Y Ju. Visible light-driven photocatalytic degradation of rhodamine B over $NaBiO_3$: pathways and mechanism. *The Journal of Physical Chemistry A*, 113:10024–10032, 2009.

[123] H Xu, NC Eddingsaas, and KS Suslick. Spatial separation of cavitating bubble populations: the nanodroplet injection model. *Journal of the American Chemical Society*, 131(17):6060–6061, 2009.

[124] M Ashokkumar, M Hodnett, B Zeqiri, F Grieser, and G Price. Acoustic emission spectra from 515 kHz cavitation in aqueous solutions containing surface-active solutes. *Journal of the American Chemical Society*, 129(8):2250–2258, 2007.

[125] KS Suslick and EB Flint. Sonoluminescence from non-aqueous liquids. *Nature*, 330(6148):553–555, 1987.

[126] WL Huang and Q Zhu. Electronic structures of relaxed BiOX (X=F, Cl, Br, I) photocatalysts. *Computational Materials Science*, 43(4):1101–1108, October 2008.

[127] C Yu, JC Yu, C Fan, H Wen, and S Hu. Synthesis and characterization of Pt/BiOI nanoplate catalyst with enhanced activity under visible light irradiation. *Materials Science and Engineering: B*, 166:213–219, 2010.

[128] Z Jiang, F Yang, N Luo, BTT Chu, D Sun, H Shi, T Xiao, and PP Edwards. Solvothermal synthesis of N-doped $TiO_2$ nanotubes for visible-light-responsive photocatalysis. *Chemical Communications*, 1(47):6372–4, December 2008.

[129] X Zhang, L Zhang, T Xie, and D Wang. Low-temperature synthesis and high visible-light-induced photocatalytic activity of BiOI/$TiO_2$ heterostructures. *The Journal of Physical Chemistry C*, 113(17):7371–7378, 2009.

[130] HG Kim, PH Borse, JS Jang, ED Jeong, O-S Jung, YJ Suh, and JS Lee. Fabrication of $CaFe_2O_4$/$MgFe_2O_4$ bulk heterojunction for enhanced visible light photocatalysis. *Chemical Communications*, (39):5889–91, October 2009.

[131] H Tada, T Mitsui, T Kiyonage, T Akita, and K Tanaka. All-solid-state Z-scheme in CdS-Au-$TiO_2$ three-component nanojunction system. *Nature Materials*, 5:782–786, 2006.

[132] SY Chai, YJ Kim, MH Jung, AK Chakraborty, D Jung, and WI Lee. Heterojunctioned BiOCl/$Bi_2O_3$, a new visible light photocatalyst. *Journal of Catalysis*, 262(1):144–149, February 2009.

[133] H Cheng, B Huang, Y Dai, X Qin, and X Zhang. One-step synthesis of the nanostructured AgI/BiOI composites with highly enhanced visible-light photocatalytic performances. *Langmuir*, 26(9):6618–24, May 2010.

[134] Y Lan, C Hu, X Hu, and J Qu. Efficient destruction of pathogenic bacteria with AgBr/$TiO_2$ under visible light irradiation. *Applied Catalysis B: Environmental*, 73(3-4):354–360, 2007.

[135] C Wu, L Shen, YC Zhang, and Q Huang. Synthesis of AgBr/ZnO nanocomposite with visible light-driven photocatalytic activity. *Materials Letters*, 66(1):83–85, 2012.

[136] N Kakuta, N Goto, H Ohkita, and T Mizushima. Silver bromide as a photocatalyst for hydrogen generation from $CH_3OH/H_2O$ solution. *The Journal of Physical Chemistry B*, 103(29):10–12, 1999.

[137] EA Taft, HR Philipp, and L Apker. Photoelectric emission from the valence band in AgBr. *Physical Review*, 110(4):3–5, 1958.

[138] CM Butler, AQ Howard, and RD Nevels. Electromagnetic diffraction of an aperture in a planar conducting screen separating partitioned half-spaces. *Journal of Applied Physics*, 48(12):4886, 1977.

[139] J Ketterer and V Kramer. Structure refinement of bismuth oxide bromide, BiOBr. *Acta Crystallographica Section C: Crystal Structure Communications*, 42(8):1098, 1986.

[140] P Wang, B Huang, X Zhang, X Qin, H Jin, Y Dai, Z Wang, J Wei, J Zhan, S Wang, J Wang, and M-H Whangbo. Highly efficient visible-light plasmonic

Photocatalyst Ag@AgBr. *Chemistry - A European Journal*, 15(8):1821–1824, 2009.

[141] T Sekine, N Ikeo, and Y Nagasawa. Comparison of AES chemical shifts with XPS chemical shifts. *Applied surface science*, 100/101:30–35, 1996.

[142] VK Kaushik. XPS core level spectra and Auger parameters for some silver compounds. *Journal of Electron Spectroscopy and Related ...*, 56(165):273–277, 1991.

[143] A Pron, RR Reghu, R Rybakiewicz, H Cybulski, D Djurado, JV Grazulevicius, M Zagorska, I Kulszewicz-Bajer, and J-M Verilhac. Triarylamine substituted arylene bisimides as solution processable organic semiconductors for field effect transistors. Effect of substituent position on their spectroscopic, electrochemical, structural, and electrical transport properties. *The Journal of Physical Chemistry C*, 115(30):15008–15017, 2011.

[144] V Resta, AM Laera, E Piscopiello, L Capodieci, MC Ferrara, and L Tapfer. Synthesis of CdS/$TiO_2$ nanocomposites by using cadmium thiolate derivatives as unimolecular precursors. *Physica Status Solidi (a)*, 207(7):1631–1635, July 2010.

[145] Y Wang, C Feng, M Zhang, J Yang, and Z Zhang. Enhanced visible light photocatalytic activity of N-doped $TiO_2$ in relation to single-electron-trapped oxygen vacancy and doped-nitrogen. *Applied Catalysis B: Environmental*, 100(1-2):84–90, October 2010.

[146] H Ehrenreich and D Turnbull. *Solid state physics: advances in research and applications*, volume 44. Academic Press, 1991.

[147] X Zong, H Yan, G Wu, G Ma, F Wen, L Wang, and C Li. Enhancement of photocatalytic $H_2$ evolution on CdS by loading $MoS_2$ as cocatalyst under visible light irradiation. *Journal of the American Chemical Society*, 130(23):7176–7177, June 2008.

[148] C Sun, Q Li, S Gao, L Cao, and JK Shang. Enhanced photocatalytic disinfection of escherichia coli bacteria by silver modification of nitrogen-doped titanium oxide nanoparticle photocatalyst under visible-light illumination. *Journal of the American Ceramic Society*, 93(11):3880–3885, November 2010.

[149] H Cheng, B Huang, P Wang, Z Wang, Z Lou, J Wang, X Qin, X Zhang, and Y Dai. In situ ion exchange synthesis of the novel Ag/AgBr/BiOBr hybrid with highly efficient decontamination of pollutants. *Chemical Communications*, 47(25):7054–6, July 2011.

[150] Z Shan, W Wang, X Lin, H Ding, and F Huang. Photocatalytic degradation of organic dyes on visible-light responsive photocatalyst $PbBiO_2Br$. *Journal of Solid State Chemistry*, 181(6):1361–1366, June 2008.

[151] W Wang, F Huang, X Lin, and J Yang. Visible-light-responsive photocatalysts xBiOBr-(1-x)BiOI. *Catalysis Communications*, 9(1):8–12, 2008.

[152] K Zhu, NR Neale, A Miedaner, and AJ Frank. Enhanced charge-collection efficiencies and light scattering in dye-sensitized solar cells using oriented $TiO_2$ nanotubes arrays. *Nano Letters*, 7(1):69–74, January 2007.

[153] R Asahi, T Morikawa, T Ohwaki, K Aoki, and Y Taga. Visible-light photocatalysis in nitrogen-doped titanium oxides. *Science (New York, N.Y.)*, 293(5528):269–71, July 2001.

[154] Y Zang and R Farnood. Photocatalytic activity of $AgBr/TiO_2$ in water under simulated sunlight irradiation. *Applied Catalysis B: Environmental*, 79(4):334–340, March 2008.

[155] Y Hou, X-Y Li, Q-D Zhao, X Quan, and G-H Chen. Electrochemical method for synthesis of a $ZnFe_2O_4/TiO_2$ composite nanotube array modified electrode with enhanced photoelectrochemical activity. *Advanced Functional Materials*, 20(13):2165–2174, May 2010.

[156] X Qiu, M Miyauchi, H Yu, H Irie, and K Hashimoto. Visible-light-driven Cu(II)-$(Sr_{1-y}Na_y)(Ti_{1-x}Mo_x)O_3$ photocatalysts based on conduction band control and surface ion modification. *Journal of the American Chemical Society*, 132(43):15259–15267, 2010.

[157] S Boumaza, A Boudjemaa, A Bouguelia, R Bouarab, and M Trari. Visible light induced hydrogen evolution on new hetero-system $ZnFe_2O_4/SrTiO_3$. *Applied Energy*, 87(7):2230–2236, July 2010.

[158] X Li, G Lu, and S Li. Synthesis and characterization of fine particle $ZnFe_2O_4$ powders by a low temperature method. *Journal of alloys and compounds*, 235:150–155, 1996.

[159] AH Nethercot Jr. Prediction of Fermi energies and photoelectric thresholds

based on electronegativity concepts. *Physical Review Letters*, 33(18):1088–1091, 1974.

[160] Z-H Yuan and L-D Zhang. Synthesis, characterization and photocatalytic activity of $ZnFe_2O_4/TiO_2$ nanocomposite. *Journal of Materials Chemistry*, 11(4):1265–1268, 2001.

[161] X Zhou, G Liu, J Yu, and W Fan. Surface plasmon resonance-mediated photocatalysis by noble metal-based composites under visible light. *Journal of Materials Chemistry*, 22(40):21337–21354, 2012.

[162] JH Kou, J Gao, ZS Li, and ZG Zou. Research on photocatalytic degradation properties of organics with different new photocatalysts. *Current Organic Chemistry*, 14(7):728–744, 2010.

[163] Z Jiang, F Al-Shahrani, T-W Lin, Y Cui, and T Xiao. Visible light activated mesoporous $TiO_{2-x}N_x$ nanocrystalline photocatalyst. In Shilun Qiu Yi Tang Dongyuan Zhao and Yu Chengzhong, editors, *Studies in Surface Science and Catalysis*, volume Volume 165, pages 355–359. Elsevier, 2007.

[164] WL Huang and Q Zhu. Structural and electronic properties of BiOX (X=F, Cl, Br, I) considering Bi $5f$ states. *Computational Materials Science*, 46(4):1076–1084, October 2009.

[165] Z Jia, F Wang, F Xin, and B Zhang. Simple solvothermal routes to synthesize 3D $BiOBr_xI_{1-x}$ microspheres and their visible-light-induced photocatalytic properties. *Industrial & Engineering Chemistry Research*, 50(11):6688–6694, 2011.

[166] C Hu, Y Lan, J Qu, X Hu, and A Wang. Ag/AgBr/$TiO_2$ visible light photocatalyst for destruction of azodyes and bacteria. *The Journal of Physical Chemistry B*, 110(9):4066–4072, 2006.

[167] L Zhang, K-H Wong, Z Chen, JC Yu, J Zhao, C Hu, C-Y Chan, and P-K Wong. AgBr-Ag-$Bi_2WO_6$ nanojunction system: a novel and efficient photocatalyst with double visible-light active components. *Applied Catalysis A: General*, 363(1-2):221–229, 2009.

[168] L Kong, Z Jiang, HH-C Lai, RJ Nicholls, T Xiao, MO Jones, and PP Edwards. Unusual reactivity of visible-light-responsive AgBr-BiOBr heterojunction photocatalysts. *Journal of Catalysis*, 293:116–125, September 2012.

[169] Audrey Moores and Fr?d?ric Goettmann. The plasmon band in noble metal nanoparticles: an introduction to theory and applications. *New Journal of Chemistry*, 30(8):1121, 2006.

[170] G Tian, Y Chen, H-L Bao, X Meng, K Pan, W Zhou, C Tian, J-Q Wang, and H Fu. Controlled synthesis of thorny anatase $TiO_2$ tubes for construction of Ag-AgBr/$TiO_2$ composites as highly efficient simulated solar-light photocatalyst. *Journal of Materials Chemistry*, 22(5):2081, 2012.

[171] CA Strydom, JF Van Staden, and HJ Strydom. An XPS investigation of silver bromide-coated ion-selective electrodes. *Electroanalysis*, 3(8):815–821, 1991.

[172] LH Tjeng, MBJ Meinders, J van Elp, J Ghijsen, and GA Sawatzky. Electronic structure of $Ag_2O$. *Physical Review B*, 41(5):3190–3199, 1990.

[173] VS Dharmadhikari and SR Sainkar. Characterisation of thin films of bismuth oxide by X-ray photoelectron spectroscopy. *Journal of Electron Spectroscopy and Related Phenomena*, 25:181–189, 1982.

[174] AF Wells. Structural inorganic chemistry. In *Structural Inorganic Chemistry*, volume 229, page 1095. February 1971.

[175] Z Tian, J Voigt, J Liu, B McKenzie, M McDermott, M Rodriguez, H Konishi, and H Xu. Complex and oriented ZnO nanostructures. *Nature Materials*, 2(12):821–6, December 2003.

[176] JH Park, S Kim, and AJ Bard. Novel carbon-doped $TiO_2$ nanotube arrays with high aspect ratios for efficient solar water splitting. *Nano Letters*, 6(1):24–28, January 2006.

[177] VBR Boppana and RF Lobo. Photocatalytic degradation of organic molecules on mesoporous visible-light-active Sn(II)-doped titania. *Journal of Catalysis*, 281(1):156–168, July 2011.

[178] I Tsuji, H Kato, H Kobayashi, and A Kudo. Photocatalytic $H_2$ evolution reaction from aqueous solutions over band structure-controlled $(AgIn)_xZn_{2(1-x)}S_2$ solid solution photocatalysts with visible-light response and their surface nanostructures. *Journal of the American Chemical Society*, 126(41):13406–13, October 2004.

[179] M Yoshino, M Kakihana, WS Cho, H Kato, and A Kudo. Polymerizable complex synthesis of pure $Sr_2Nb_xTa_{2-x}O_7$ solid solutions with high photocatalytic

activities for water decomposition into $H_2$ and $O_2$. *Chemistry of Materials*, 14(8):3369–3376, 2002.

[180] S Ouyang and J Ye. $\beta$-$AgAl_{1-x}Ga_xO_2$ solid-solution photocatalysts: continuous modulation of electronic structure toward high-performance visible-light photoactivity. *Journal of the American Chemical Society*, 133(20):7757–7763, 2011.

[181] L Wang, J Zhang, C Li, H Zhu, W Wang, and T Wang. Synthesis, characterization and photocatalytic activity of $TiO_2$ film/$Bi_2O_3$ microgrid heterojunction. *Journal of Materials Science & Technology*, 27(1):59–63, January 2011.

[182] Fabrício R. Sensato, Rogério Custodio, Elson Longo, Armando Beltrán, and Juan Andrés. Electronic and structural properties of $Sn_xTi_{1-x}O_2$ solid solutions: a periodic DFT study. *Catalysis Today*, 85(2-4):145–152, October 2003.

[183] MH Harunsani, FE Oropeza, RG Palgrave, and RG Egdell. Electronic and structural properties of $Sn_xTi_{1-x}O_2$ ($0 \leq x \leq 1$) solid solutions. *Chemistry of Materials*, 22(4):1551–1558, February 2010.

[184] J J Pireaux, J Riga, R Caudano, J J Verbist, J Delhalle, S Delhalle, J M André, and Y Gobillon. Polymer primary structures studied by ESCA and EHCO methods. *Physica Scripta*, 16(5-6):329–338, November 1977.

[185] AJ Nozik. Photoelectrochemistry: Applications to solar energy conversion. *Annual review of physical chemistry*, pages 189–222, 1978.